
Laser Cooling of Intense Relativistic Ion Beams

Laserkühlung von intensiven relativistischen Ionenstrahlen

Zur Erlangung des Grades eines Doktors der Naturwissenschaften (Dr. rer. nat.)

genehmigte Dissertation von Lewin Eidam M.Sc. aus Fritzlár

Tag der Einreichung: 12.09.2017, Tag der Prüfung: 14.12.2017

Darmstadt – D 17

1. Gutachten: Prof. Dr. Oliver Boine-Frankenheim
2. Gutachten: Prof. Dr. Joachim Enders



TECHNISCHE
UNIVERSITÄT
DARMSTADT

Institut für
Theorie Elektromagnetischer Felder
Fachbereich Elektrotechnik
und Informationstechnik

Laser Cooling of Intense Relativistic Ion Beams
Laserkühlung von intensiven relativistischen Ionenstrahlen

Genehmigte Dissertation von Lewin Eidam M.Sc. aus Fritzlar

1. Gutachten: Prof. Dr. Oliver Boine-Frankenheim
2. Gutachten: Prof. Dr. Joachim Enders

Tag der Einreichung: 12.09.2017

Tag der Prüfung: 14.12.2017

Darmstadt – D 17

Bitte zitieren Sie dieses Dokument als:

URN: [urn:nbn:de:tuda-tuprints-71523](https://nbn-resolving.org/urn:nbn:de:tuda-tuprints-71523)

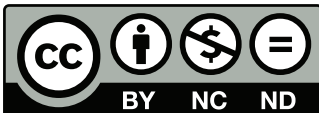
URL: <http://tuprints.ulb.tu-darmstadt.de/7152>

Das Dokument wird bereitgestellt von tuprints,

E-Publishing-Service der TU Darmstadt

<http://tuprints.ulb.tu-darmstadt.de>

tuprints@ulb.tu-darmstadt.de



Die Veröffentlichung steht unter folgender Creative Commons Lizenz:

Namensnennung – Keine kommerzielle Nutzung – Keine Bearbeitung 4.0 International

<http://creativecommons.org/licenses/by-nc-nd/4.0/>



Laser Cooling of Intense Relativistic Ion Beams

Vom Fachbereich Elektrotechnik und Informationstechnik
der Technischen Universität Darmstadt

zur Erlangung des Grades
eines Doktors der Naturwissenschaften
(Dr. rer. nat.)

genehmigte Dissertation
von Lewin Eidam M.Sc. aus Fritzlar

1. Gutachter: Prof. Dr. Oliver Boine-Frankenheim
2. Gutachter: Prof. Dr. Joachim Enders

Tag der Einreichung: 12.09.2017
Tag der mündlichen Prüfung: 14.12.2017

Darmstadt 2018
D17



Zusammenfassung

Die Doppler-Laserkühlung ist eine Methode zur Reduzierung der longitudinalen Impulsverteilung eines Ionenstrahls in einem zirkularen Beschleuniger. In der Vergangenheit wurde das Prinzip an nicht-relativistischen Ionenstrahlen untersucht und verifiziert. Im Rahmen des FAIR-Projekts wird erstmalig die Laserkühlung an hoch intensiven und relativistischen Ionenstrahlen angewendet. Die Laserkühlung erhöht die longitudinale Ionendichte und führt zu exotischen longitudinalen Phasenraumverteilungen des Ionenstrahls. Diese Dissertation befasst sich mit der numerischen Untersuchung der Teilchendynamik und dem Zusammenspiel der Laserkraft und Intensitätseffekten, um den Kühlprozess zu optimieren und einen stabilen Betrieb des Beschleunigers während der Strahlkühlung zu gewährleisten.

Diese Arbeit beschreibt die Ionen-Photonen-Wechselwirkung und leitet die Laserkraft für relativistische Ionenstrahlen her. Die Kraft wird für eine zeitlich konstante und eine gepulste Laseranregung berechnet. Die Anregung mit einem gepulsten Laser führt zu einer breitbandigen Kraft, welche auf alle Ionen gleichzeitig wirkt. Die zeitlich konstante Anregung resultiert in einer drei bis vier Größenordnungen schmalbandigeren Laserkraft. Um eine Kühlung aller Ionen zu gewährleisten, wird die Position der schmalbandigen Laserkraft im Phasenraum sequentiell abgefahren. Die Teilchendynamik beider Kühlprozesse wird analysiert und miteinander verglichen.

Der Einfluss von Heizprozessen auf den Verlauf der Strahlkühlung ist Teil der Untersuchung. Streuprozesse innerhalb des Strahls limitieren die maximale Ionendichte des Kühlprozesses mit zeitlich konstanter und gepulster Laseranregung. Darüber hinaus zeigen numerische Simulationen zwei Instabilitäten, welche während der sequentiellen Abtastung der schmalbandigen Laserkraft durch Raumladung ausgelöst werden. Diese Arbeit beschreibt die Entstehung der Instabilitäten und die Auswirkungen auf den Kühlprozess. Analytische Ausdrücke für den Schwellwert der Strahlintensität werden angegeben.

Die Skalierung des Kühlprozesses und der relevanten Intensitätseffekte für unterschiedliche Strahlenergien wird diskutiert, um einen Ausblick auf künftige Experimente von Laserkühlung an relativistischen Ionenstrahlen zu geben. Die Arbeit schließt mit einem Vergleich der Laserkühlung von nicht-relativistischen Kohlenstoffionen und relativistischen Titanionen ab. Der Vergleich zeigt die Herausforderungen der Laserkühlung im SIS100 Synchrotron an FAIR auf.



Abstract

Doppler laser cooling is a technique to reduce the longitudinal momentum spread of an ion beam in a circular accelerator. In the past, the principle was investigated and verified on non-relativistic ion beams. Within the FAIR project, laser cooling will be applied to high intensity and relativistic ion beams for the first time. Laser cooling results in a further increase of the longitudinal ion density and creates exotic longitudinal phase space distributions. In order to ensure stable operation and optimize the cooling process, this dissertation numerically investigates the particle dynamics and the interplay of the laser force and high intensity effects.

This work describes the ion-photon interaction and derives the laser force on ions at relativistic energies. The force is calculated for continuous wave and pulsed laser excitations. The pulsed laser excitation results in a broadband force, which interacts with all ions simultaneously, whereas the width of the continuous wave laser force is typically three to four orders of magnitude smaller. In order to interact with all ions, the position of the continuous wave laser force is scanned during the cooling process. The particle dynamics during the cooling processes for both laser forces are analyzed and compared.

The impact of heating effects during the laser cooling process is also investigated. Scattering events within the beams limit the maximum ion intensity for the cooling for both a continuous wave or a pulsed laser system. In addition, numerical simulations show two instabilities, that arise during the scan of the continuous wave laser force and are triggered by space charge. This work describes the development of the instabilities and the impact on the laser cooling process. Analytical expressions for the threshold of instabilities and maximum ion intensities are given.

The scaling of the cooling process and intensity limitations with beam energy is discussed in order to evaluate the prospects of laser cooling experiments at relativistic energies. The work concludes with the comparison of the cooling process of non-relativistic carbon ions and relativistic titanium ions. The comparison emphasizes the main challenges for laser cooling experiments in the SIS100 synchrotron at FAIR.



Contents

1	Introduction	1
1.1	Synchrotrons	1
1.2	Beam Cooling	3
1.3	Motivation	5
1.4	Overview	6
2	Beam Dynamics and Intensity Effects	7
2.1	Particle Dynamics in Synchrotrons	7
2.2	Space Charge	12
2.3	Intra Beam Scattering	14
3	Doppler Laser Cooling	17
3.1	Principle of Doppler Laser Cooling	17
3.2	Laser Cooling Force in Accelerators	19
3.2.1	Continuous Wave Excitation	24
3.2.2	Pulsed Laser Excitation	27
4	Simulation Model	31
4.1	Intensity Effects	33
4.2	Laser Ion Interaction	35
4.2.1	Statistical cw Laser Model	35
4.2.2	Mean cw Laser Model	37
4.2.3	Pulsed Laser Model	37
4.2.4	Impact on Cooling Process	38
5	Cooling Process	41
5.1	Continuous Wave Laser	42
5.2	Pulsed Laser	48
5.3	Combined Laser Systems	51
5.4	Alternative Bucket Shapes	53
6	Intensity Effects	59
6.1	Intra Beam Scattering	59
6.1.1	Pulsed Laser	59
6.1.2	Continuous Wave Laser	61
6.2	Space Charge	63



6.2.1	Bunch Length Limit	63
6.2.2	Continuous Wave Laser	67
6.2.2.1	Local rf-Compensation	67
6.2.2.2	Microwave Instability	70
7	Prospects for Relativistic Ion Beams	79
7.1	Scaling Laws of Cooling Process	79
7.1.1	Intensity Limitations	82
7.2	Relativistic Laser Cooling Example	86
7.3	Effects on Transverse Dynamics	88
7.3.1	Transverse Laser Heating	89
7.3.2	Sympathetic Cooling	90
7.3.3	Induced Longitudinal-Transverse Coupling	92
8	Conclusion and Outlook	93
	Bibliography	106

1 Introduction

Accelerated particle beams have become increasingly important within the 20th century. Nowadays particle accelerators are applied in a broad range of scientific research and industrial processes. The field of research is wide spread including for example nuclear, atomic and material science and biology. Even in medicine accelerated particle beams are used for example in cancer therapy [1].

First particle accelerators were realized by electrostatic acceleration. This simple concept has the drawback of limited kinetic energy of the particles due to the finite breakdown voltage [2]. Initiated by the development of oscillating field accelerators and linear accelerators [3], the kinetic energy of the particles could be increased drastically. Beside the linear accelerators, huge circular accelerators have been developed [4]. In circular accelerators the particles pass the accelerating components several times and can be accelerated very efficiently. This concept enables the acceleration of particle beams to the high beam energies which are required for nuclear structure experiments.

Beside the pursuit of reaching higher beam energies, accelerator researchers deal with limiting factors of particle intensity and beam divergence. A low divergence of the particle beam is desired for accurate and precise experiments and to keep the particle beam in the aperture of the accelerator. One concept for the reduction of the particle divergence in longitudinal direction is investigated in this work.

1.1 Synchrotrons

In a synchrotron the trajectory of the particles is bent by dipole magnets to a circle. The transverse confinement is realized by a technique called strong focusing [5]. Transverse oscillations, created by quadrupole magnets with alternating polarity, prevent the particles from diverging and keep them on the axis. The particles are accelerated and confined in longitudinal direction by oscillating longitudinal electric fields excited in radio frequency (rf) cavities. This concept allows to accelerate and store protons and a wide variety of different ions with a relative compact design [6]. The term synchrotron originates in the concept, that the different accelerator components are adapted and synchronized in order to keep the ions on the same trajectory during acceleration.

Usually in a scientific accelerator facility, synchrotrons are one part of a chain, that is required for the creation and acceleration of the particles for experiments. Charged particles are created in particle sources and typically electrostatically preaccelerated. A further acceleration is realized by a linear accelerator before the charged particles are injected into a synchrotron. For experiments the particles either collide with a second accelerated particle beam or are guided on a fixed target experiment. Another option is to inject the particles in another synchrotron for storage or further acceleration.

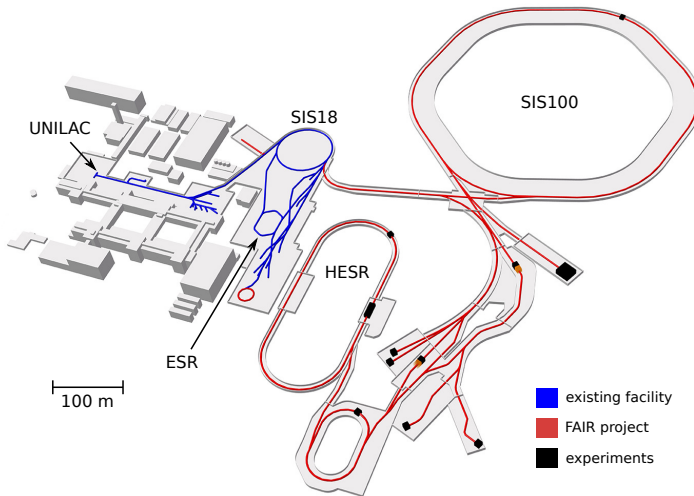


Figure 1.1: Site map of the planned FAIR facility including the already existing accelerator components and buildings of GSI. Laser cooling experiments have been conducted in the ESR and are planned to take place in the SIS100 in the future. Figure from [7].

The GSI Helmholtz Center for Heavy Ion Research is a multipurpose research facility with an accelerator chain for research with a wide range of different ions (marked in blue in fig. 1.1). The different ions are created in sources connected to the linear preaccelerator UNILAC. After acceleration the particles are used for experiments or are injected into the synchrotron SIS18 (Schwerionensynchrotron). After acceleration a further variety of experiments exist or the particles are transferred into the storage ring ESR (Experimentierspeicherring). The ESR, with a length of 108.36m and a magnetic rigidity of 10 Tm, is able to store uranium ions with an energy up to 560 MeV/u. The storage ring includes an electron cooler and precise beam diagnostics for experiments like mass spectroscopy of rare isotopes. In the ESR first laser cooling experiments on relativistic ion beams were performed.

The existing accelerators at GSI are the basis for the international research facility FAIR (Facility for Antiproton and Ion Research), which is presently under construction. The facility will be extended with a wide range of experiments and further stages of the accelerator chain. The existing SIS18 will serve as injector for the SIS100 as shown in fig. 1.1. The synchrotron SIS100, with a length of 1083m, will be able to store ion beams with a magnetic rigidity up to 100 Tm. In the SIS100 laser cooling will be installed and studied at relativistic heavy ions beams for the first time.

1.2 Beam Cooling

In accelerators and storage rings the mean velocity and position deviation of accelerated particles originates from the particle source and is transported through the accelerator chain. Due to imperfections of the accelerator components, plasma instabilities or in general heating mechanisms, the velocity and position deviation increases during the transport to the experiments. The desired accuracy in experiments and the finite size of the vacuum chamber of the accelerator demand small position and velocity deviations.

A measure for the mean velocity deviation of a particle ensemble is given by the temperature T . The temperature of a particle ensemble in free space is defined by (see Ref. [8])

$$\frac{3}{2}k_B T = \frac{1}{2}m \langle |\vec{v} - \langle \vec{v} \rangle|^2 \rangle, \quad (1.1)$$

where k_B is the Boltzmann constant, m the mass of each particle and \vec{v} the three dimensional velocity. The brackets $\langle \cdot \rangle$ denote the mean value for the ensemble. For a stationary ensemble, e.g. in a particle trap, the velocity of the center of mass $\langle \vec{v} \rangle$ is zero. In a particle accelerator the subtraction of the center of mass velocity is very important, because the mean velocity deviation of the particles is very small compared to the mean velocity of the particle ensemble.

The definition Eq. 1.1 follows the equipartition theorem. This theorem assumes the particle ensemble to be in thermal equilibrium and consequently the energy to be shared equally among the three degrees of freedom. For an accelerated ion beam the velocity spread usually differs in the longitudinal and the transverse coordinates. For particles ensembles that are not in thermal equilibrium, the temperature is defined for each degree of freedom by (see Ref. [8])

$$\frac{1}{2}k_B T_i = \frac{1}{2}m (\langle v_i^2 \rangle - \langle v_i \rangle^2), \quad (1.2)$$

where the index $i \in x, y, z$ splits the three spatial coordinates.

Beside the efforts of keeping the initial temperature of the particle ensemble as small as possible and trying to avoid heating of the particle beam during the transport, the accelerated particle ensemble can be actively cooled down. The term cooling describes the temperature reduction of a particle ensemble and consequently the reduction of the mean velocity deviation. Different methods for the cooling of a particle ensemble exist. The preferred method depends on the particle species and the desired final temperature. For ion beams in a circular accelerator three different cooling techniques exist:

Electron Cooling:

The principle of electron cooling was conceived by Budker [9] and experimentally demonstrated in Novosibirsk for the first time [10]. Electron cooling employs the heat transfer of the ion beam to an electron beam. The initial electron beam has a low temperature and is accelerated to the velocity of the ion beam. Both beams are

merged in one section of the accelerator. After typically a few meters the electron beam and the ion beam are separated again and the electron beam is decelerated and dumped. In the co-moving frame of the electrons, the electrons have very low relative velocities while the ions have high relative velocities. During the interaction the ions and electrons perform elastic scattering (Rutherford scattering, see Ref. [11]). These coulomb interactions reduce the relative velocity of the ion beam and increases the relative velocities of the electron beam. The used electrons are constantly replaced by cold electrons from the electron cooler which enables an efficient cooling of the ions.

Electron cooling is widely used in ion accelerators, because it reduces the populated phase space area of an ion beam in all three dimensions. The only requirement is the matched velocity of the electrons and ions. Thus, the principle is not restricted to a certain ion species or charge states and can be used in a broad range of applications. At the GSI facility electron coolers are installed in the SIS18 and in the ESR (see Fig. 1.1). For the electron cooling process in the ESR the ion beam has typically an initial root mean square (rms) momentum spread of $\Delta p/p_0 \approx 10^{-3}$ and is cooled down to $\Delta p/p_0 \approx 10^{-5}$ [12]. For very diluted ion beams with only a few hundred ions, a final rms momentum spread of $\Delta p/p_0 \approx 10^{-6}$ is possible [13].

The cooling rate is proportional to the electron density and is inversely proportional to the relativistic factor of the ion beam squared (see Ref. [14])

$$\tau_{cool}^{-1} \propto \frac{n_e}{\gamma^2}. \quad (1.3)$$

In order to keep a reasonable cooling time the density of the electron beam has to be increased for high energy beams. In addition for ion beams with $\gamma \gg 1$ the required kinetic energy reaches the limit of electrostatic acceleration. The increasing electron density and required electron energy lead to unfeasible electron cooler designs. One of the most powerful electron coolers is planned at the HESR, see fig. 1.1, where electrons are accelerated up to 4.5 MeV with a maximum current of 1 A [15].

Stochastic Cooling:

Stochastic cooling was invented by van der Meer for the accumulation of anti-protons [16] and was demonstrated experimentally at CERN in 1979 [17]. The success was honored with the Nobel price. For stochastic cooling the charge distribution of the circulating ion bunch is measured with a broadband pickup. After signal processing and amplification the signal is applied again to the ion beam by a kicker device. A detailed explanation is found in Ref. [18]. Stochastic cooling can be applied to any circulating charged particles, but it is typically used for precooling. In the ESR stochastic cooling is used for hot ion bunches with a rms momentum spread of $\Delta p/p_0 > 10^{-3}$ [19].

Laser Cooling:

Laser cooling describes the reduction of the momentum spread of a particle ensemble using the excitation and spontaneous deexcitation of an atomic state in the accelerated ions with laser light. The detailed explanation of the underlying process and the cooling force is explained in Sect. 3.1. The technique originates in cooling of ions in a particle trap. The exploration of this cooling technique was honored with the Nobel prize in

physics in 1997 [20]. Laser cooling of stored coasting and bunched beams has been demonstrated at the TSR in Heidelberg (Germany) [21, 22], and at ASTRID in Aarhus (Denmark) [23]. At the ESR in Darmstadt (Germany), first laser cooling experiments with relativistic ion beams were conducted [24]. In the future, laser cooling of intense highly charged ion beams at relativistic energies will be attempted for the first time in the SIS100 at FAIR, which is presently under construction [25]. Compared to other cooling techniques, laser cooling can produce ultra cold ion ensembles, which reach the crystalline state [26]. The major drawback of laser cooling is the restriction to certain ions and charge states. The laser wavelength has to match the atomic transition. This constraint adds a fixed correlation between the atomic transition, wavelength of the laser system and speed of the ions, that is described in more detail in Sect. 3.2 and Ref. [24].

1.3 Motivation

For high energy ion beams no practical cooling technique is available. On the one hand the efficiency of electron cooling decreases tremendously with increasing ion energy as described by Eq. 1.3. For $\gamma \gg 1$ the devices become unfeasible complex, expensive and power consuming. On the other hand stochastic cooling does not cool ion beams to very low temperatures and is only useful for precooling. However a very promising technique for an efficient cooling at high energies is given by laser cooling. As estimated in Ref. [27] the cooling force should increase for higher beam energies. Compared to other cooling techniques laser cooling is more cost efficient and requires only little space in a circular accelerator for merging of the laser and the ion beam. Beside the possibility of beam cooling, the setup of laser cooling enables to perform spectroscopy of atomic states, that can not be investigated in conventional particle traps. Due to the large Doppler shift in the particle frame (see Sect. 3.2) properties of transitions with a high energy gap can be measured very precisely.

For the demonstration and exploration of laser cooling at relativistic ion beams, the cooling setup will be installed in the SIS100 at the FAIR facility. In the past laser cooling was only applied to low energy beams ($\gamma \approx 1$). In order to estimate required laser intensities and cooling times for the high energy regime, the ion photon interaction and the cooling process have to be studied analytically and numerically in advance. This work addresses the detailed calculation of the cooling force produced by the laser beam and an analysis of the particle dynamics during the cooling process. The influence of different configurations of the accelerator on the cooling strength is mostly unknown. Especially for high intensity ion beams, which will be available in the SIS100, the detailed interplay of intensity effects and the laser cooling force are not yet understood. This thesis includes an analysis of the cooling process for different accelerator configurations and intensity limiting factors for an efficient laser cooling process.

1.4 Overview

After introducing the general concept of synchrotrons and different methods of ion beam cooling in Chapter 1, the particle dynamics and heating effects of ion beams is described in Chapter 2. The introduction is focused on the longitudinal phase space and on the two intensity effects, space charge and intra beam scattering, that are the intensity limiting processes for laser cooling. Chapter 3 introduces the concept of laser cooling. The principle of laser cooling in a particle trap and the differences between the cooling of a stationary and an accelerated ion ensemble is discussed. The force of pulsed and continuous wave laser excitation is evaluated. Chapter 4 deals with the implementation of the ion photon interaction in a particle-in-cell tracking code.

Numerical results of the laser cooling process are shown in Chapter 5 and compared to analytical models. Different cooling schemes with the pulsed and continuous wave laser sources are discussed. The impact of intra beam scattering and space charge on the cooling process is described in Chapter 6.

The scaling of the laser force and the counteracting intensity effects with the ion beam energy is investigated in Chapter 7. The scaling gives insights in prospects of laser cooling for relativistic ion beams. Examples of the laser cooling process of a non-relativistic and a relativistic ion beam are compared in Sect. 7.2. The influence of laser cooling on the transverse phase space and the restriction of the study to the longitudinal phase space is discussed in Sect. 7.3.

The Thesis concludes with a summary and outlook in Chapter 8.

2 Beam Dynamics and Intensity Effects

The framework which is commonly used for the description of particle dynamics in circular accelerators is presented in this chapter. It concentrates on aspects that are relevant for the process of laser cooling. A complete description is found e.g. in Ref. [8]. Section 2.1 focuses on the utilized coordinate system and the description of the single particle motion. The interaction with other particles is neglected. Section 2.2 and 2.3 introduce the main inter-particle interactions, which become relevant during the laser cooling process.

2.1 Particle Dynamics in Synchrotrons

Charged particles are accelerated and guided by the Lorentz force. The force \vec{F} on a particle with velocity \vec{v} and charge $q = Z \cdot e$, where Z denotes the charge state of the ion and e the elementary charge, is given by

$$\vec{F}(\vec{r}, \vec{v}, t) = \frac{d\vec{p}(\vec{r}, \vec{v}, t)}{dt} = q \cdot (\vec{E}(\vec{r}, t) + \vec{v}(t) \times \vec{B}(\vec{r}, t)). \quad (2.1)$$

The electric field and the magnetic flux density are described by $\vec{E}(\vec{r}, t)$ and $\vec{B}(\vec{r}, t)$. The force changes the momentum $\vec{p} = \gamma m \vec{v}$ of the particle, where $\gamma = (1 - \beta^2)^{-1/2}$ is the relativistic factor, $\beta = v/c_0$ the relativistic velocity, c_0 the speed of light and m the mass of the particle. Following Eq. 2.1, charged particles are bent to a circle under influence of a homogeneous magnetic field. The equation for the determination of the bending radius ρ is given by

$$B\rho = \frac{p}{q}, \quad (2.2)$$

where $B\rho$ is called magnetic rigidity. For the bending radius of the storage ring and the highest magnetic field, which is reached in the dipole magnets, the magnetic rigidity describes the ability to store particles at high energies. The SIS100 has a maximum magnetic rigidity of 100 Tm while the ESR only attains 10 Tm. As a result, in the SIS100 particles with the same charge state can be stored with a ten times higher momentum compared to the ESR.

The motion and position of the particles are described with respect to the reference particle. The reference particle circulates on the design orbit with the length L_{acc} , which

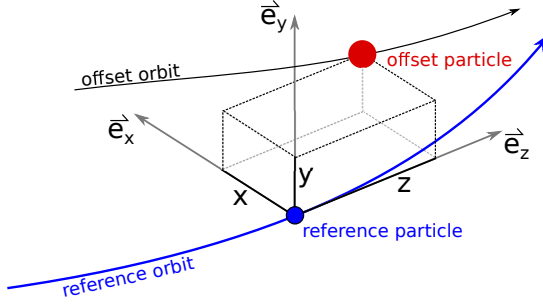


Figure 2.1: Sketch of the co-moving coordinate system. The coordinate system moves with a reference particle along the ideal orbit in the accelerator.

is typically located in the center axis of all magnets and accelerator devices. The reference particle position on the reference orbit is s and moves with the reference velocity βc_0 . The z -coordinate points in the direction along the reference orbit, while the x - and y -coordinate are arranged perpendicular to z . An offset in z -direction can also be considered as a temporal offset with $\Delta t = \Delta z \cdot \beta c_0$. In this coordinate system, see fig. 2.1, the position of a particle in phase space can be described by the 6-dimensional vector

$$\vec{r} = \begin{pmatrix} x \\ x' \\ y \\ y' \\ z \\ \delta \end{pmatrix}, \quad (2.3)$$

where $x' = dx/ds$ and $y' = dy/ds$ are the derivatives of the transverse position with respect to the position on the reference orbit s . The two quantities describe the divergence of the particle in transverse direction. The change in longitudinal direction z is given by the relative momentum deviation $\delta = (p - p_0)/p_0$ where p_0 is the momentum of the reference particle. Note that the transformation of the coordinate system at rest to the co-moving frame is not a Lorentz transformation. In the co-moving frame, the length and time are measured in the laboratory frame at rest.

While in a real accelerator coupling between the degrees of freedom exists, the motion of the particle ensemble can be separated in the transverse and longitudinal direction for simplified models. In the transverse coordinates the particles perform betatron oscillations that are induced by the quadrupole magnets. The motion is described by the Twiss parameters [28], which arise by solving the differential equation of transverse motion, called Hill's equation [29]. Each particle moves on an ellipse in phase space, whose enclosed area is the single particle emittance and the orientation of the ellipse

is described by the Twiss parameters. The rms emittance $\epsilon_{x,y}$ of an ion ensemble is given by the rms value of the single particle emittances that correlates to the rms beam envelope by (exemplary for x)

$$\epsilon_x = \sqrt{\sigma_x^2 \sigma_{x'}^2 - \sigma_{xx'}^2}, \quad (2.4)$$

where $\sigma_x = \sqrt{\langle x^2 \rangle - \langle x \rangle^2}$ is the rms beam size, $\sigma_{x'} = \sqrt{\langle x'^2 \rangle - \langle x' \rangle^2}$ the rms beam divergence and $\sigma_{xx'} = \langle xx' \rangle - \langle x \rangle \langle x' \rangle$ the correlation. The relation of the beta function $\beta(s)$ at the position s in the accelerator and the corresponding rms beam size is

$$\sigma_x(s) = \sqrt{\beta(s) \epsilon_x}. \quad (2.5)$$

The longitudinal structure in phase space is differentiated in coasting and bunched beams. In coasting beams, the particles are not longitudinally confined and circulate in the accelerator with constant momentum. A change in longitudinal position originates in a deviation of the velocity Δv or in a change of the length of the orbit ΔL_{acc} with respect to the reference particle (see Ref. [28])

$$\frac{\Delta v}{v} = \frac{1}{\gamma^2} \delta \quad (2.6)$$

$$\frac{\Delta L_{acc}}{L_{acc}} = \frac{\delta}{L_{acc}} \int \frac{D(s)}{\rho(s)} ds = \frac{1}{\gamma_t^2} \delta. \quad (2.7)$$

where $D(s)$ and $\rho(s)$ are the dispersion function and the bending radius at the position s , respectively. The dispersion is defined by the accelerator lattice and the integral is summarized in the quantity γ_t , called gamma transition. The change in the revolution time is calculated by

$$\frac{\Delta T_{rev}}{T_{rev}} = \frac{\Delta L_{acc}}{L_{acc}} - \frac{\Delta v}{v} = \eta \cdot \delta, \quad (2.8)$$

where $\eta = \frac{1}{\gamma_t^2} - \frac{1}{\gamma^2}$ defines the slip factor. The velocity in the co-moving frame results in

$$v_z = \frac{dz}{dt} = -\eta \beta c_0 \delta. \quad (2.9)$$

At transition energy, which is defined when the relativistic factor and gamma transition are equal, the slip factor becomes zero and all particles have the same revolution frequency independent of the momentum. Above the transition energy particles with a higher momentum circulate slower in the accelerator. This work concentrates on beams below the transition energy ($\gamma < \gamma_t$), however many results are also valid for beams above the transition energy.

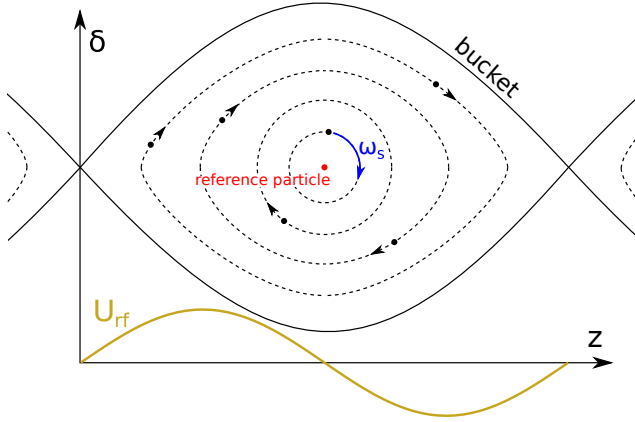


Figure 2.2: Sketch of the longitudinal dynamics in phase space. The reference particle is in the center of the bucket. The frequency of the oscillations is given by the synchrotron frequency (see Eq. 2.15).

For bunched beams the particles are longitudinally confined by radio frequency (rf) electric fields, which are produced in the acceleration cavities. The rf fields create stable areas in phase space, called buckets, where the particles are confined and oscillate around the reference particle. Usually, the rf fields have a sinusoidal shape and the frequency is matched to the revolution frequency of the particles ω_{rev} . The voltage which is seen by the particle, reads

$$U_{rf}(z) = -U_0 \cdot \sin\left(\frac{2\pi h}{L_{acc}} \cdot z + \phi_s\right), \quad (2.10)$$

where U_0 is the amplitude of the accelerating voltage. The harmonic number $h = \omega_{rf}/\omega_{rev}$ describes the number of buckets in the accelerator, where $\omega_{rev} = 2\pi\beta c_0/L_{acc}$. The synchronous phase ϕ_s describes the phase difference between the reference particle and the applied rf field. For $\phi_s \neq 0$ the reference particle experiences a momentum change while for $\phi_s = 0$ the momentum of the reference particle is constant. This configuration is called stationary bucket. This work will only deal with stationary buckets and the synchronous phase is set to $\phi_s = 0$ in the following. Alternative bucket shapes which do not have a simple sinusoidal shape, exist. The advantages and disadvantages of laser laser cooling in alternative bucket shapes are discussed in Sect. 5.4.

The motion of individual particles in the ion distribution can be derived from the Hamiltonian

$$\mathcal{H}(z, \delta) = \frac{(\eta\beta c_0\delta)^2}{2} + \frac{q\eta}{m\gamma L_{acc}} Y(z), \quad (2.11)$$

where $Y(z)$ is the potential of the electric field

$$Y(z) = \int_0^z U(z') dz'. \quad (2.12)$$

For an ion distribution that populates only the area close to the center of the bucket, the externally applied rf field (see Eq. 2.10) can be described by a linear approximation

$$U_{rf}(z) \approx -\frac{U_0 2\pi h}{L_{acc}} \cdot z \quad \text{for } z \ll \frac{L_{acc}}{2h}. \quad (2.13)$$

The Hamiltonian in the linear region reads

$$\mathcal{H}_{lin} = \frac{(\eta\beta c_0)^2}{2} \cdot \delta^2 - \frac{q\eta 2\pi h U_0}{m\gamma L_{acc}^2} \cdot z^2. \quad (2.14)$$

The quadratic dependency of the momentum and position is equivalent to the Hamiltonian of a harmonic oscillator. The ions perform oscillations in the rf potential and move on an ellipse in phase space as illustrated in fig. 2.2. In the linear region the oscillation frequency, called synchrotron frequency, is independent of the amplitude and is determined by

$$\omega_s = \frac{2\pi}{T_{rev}} \cdot \sqrt{-\frac{hq\eta U_0}{2\pi m\beta^2 \gamma c_0^2}}. \quad (2.15)$$

Particles with a high oscillation amplitude penetrate into the non-linear region of the rf fields, which reduces the synchrotron frequency. Equivalently to the synchrotron frequency, the synchrotron tune is commonly used for the description of the speed of the longitudinal oscillation. The synchrotron tune sets the synchrotron frequency in relation to the revolution frequency and is calculated by

$$Q_s = \omega_s \cdot \frac{T_{rev}}{2\pi}. \quad (2.16)$$

Typically, the synchrotron tune is between $Q_s \approx 10^{-3} - 10^{-5}$ for heavy ion synchrotrons. Due to the scaling of Eq. 2.9 with γ the synchrotron tune is usually much higher for ion beams with low γ compared to ion beams with high γ .

For the stable operation of a circular accelerator a stationary ("matched") phase space distribution is beneficial. A distribution is matched when it is a function of the Hamiltonian only and when the Hamiltonian is invariant. One example of a matched distribution is given by the Hofmann-Pedersen distribution (see Ref. [30])

$$g(\mathcal{H}) = C_1 \cdot \sqrt{\mathcal{H}_m - \mathcal{H}}, \quad (2.17)$$

where C_1 is the normalization constant, \mathcal{H} the Hamiltonian at the phase space position (z, δ) and \mathcal{H}_m the maximum value of the Hamiltonian. The maximum momentum $\hat{\delta}$ and the position of the bunch boundary \hat{z} in the bucket are given by

$$\hat{\delta} = \frac{2}{\eta^2 \beta^2 c_0^2} \cdot \mathcal{H}_m \quad (2.18)$$

$$Y(\hat{z}) = \frac{m\gamma L_{acc}}{q\eta} \cdot \mathcal{H}_m. \quad (2.19)$$

As described in more detail in Ref. [31] the longitudinal ion density for the Hofmann-Pedersen distribution results in

$$\lambda(z) = C_2 \cdot (Y(z) - Y(\hat{z})) \quad (2.20)$$

where C_2 is a normalization constant. This equation simplifies for ion bunches in the linear region of the bucket to

$$\lambda_{lin}(z) = \frac{3N_p}{4\hat{z}^3} (\hat{z}^2 - z^2) \quad \text{for } \hat{z} \ll \frac{L_{acc}}{2h}. \quad (2.21)$$

In the linear region the distribution function has a parabolic shape and is enclosed by a sharp edge in phase space. This distribution does not exist in a real accelerator but comes close to the Gaussian phase space distribution typically found for heavy ion beams in synchrotrons. The elliptic matched distribution serves as the initial distribution in this work because the sharp edge of the momentum distribution is very practical for the study of the laser cooling process.

2.2 Space Charge

The previously described particle dynamics characterize the single particle motion and neglect the interactions of particles with each other. This approximation only applies to low phase space densities and diluted beams. Modern accelerators transport particle beams with high phase space densities in order to reach high cross sections in the physical experiments. In this regime the inter-particle interactions are crucial for the analysis of particle dynamics.

The charged particle beam travels in the vacuum chamber of the accelerator and creates an electromagnetic field. The electromagnetic field, which depends on the intensity and shape of the particle bunch, acts back on the ions. This intensity dependent force is called space charge. Usually the force is split into the three different components x , y , z in the co-moving frame. We will concentrate on the longitudinal space charge fields that are important for this work. A detailed explanation of the three dimensional force is described in e.g. Ref. [8]. In the co-moving frame the charge density of the particle bunch is in good approximation stationary. For the calculation of the longitudinal component of the space charge force the particle beam is approximated by a line density $\lambda(z)$ in the co-moving frame, which travels with velocity βc_0 in a perfectly conducting pipe. The traveling charge distribution creates a current in the perfectly conducting pipe with opposite sign. Applying Faraday's law, as described in Ref. [8], the space charge induced electric field E_s is calculated by

$$E_s = -\frac{qg_{sc}}{4\pi\epsilon_0\gamma^2} \frac{\partial\lambda(z)}{\partial z}, \quad (2.22)$$

where ϵ_0 denotes the vacuum permittivity and $g_{sc} = 1 + 2\ln\left(\frac{b}{a}\right)$ the geometrical factor for the electric field in the center of the bunch with the quotient of the pipe radius b and the beam radius a . For a pure longitudinal treatment the electric field is averaged over the transverse position and the geometrical factor evolves into $g = \frac{1}{2} + 2\ln\left(\frac{b}{a}\right)$.

The space charge potential Y_{sc} is calculated equivalently to the rf potential in Eq. 2.12.

$$Y_{sc}(z) = -\frac{qgL_{acc}}{4\pi\epsilon_0\gamma^2} \cdot (\lambda(z) - \lambda(0)) \quad (2.23)$$

For the elliptical distribution (see line density in Eq. 2.20) the space charge potential simplifies to

$$Y_{sc}(z) = -\frac{qgL_{acc}}{4\pi\epsilon_0\gamma^2} \cdot C_2 \cdot Y_{rf}(z). \quad (2.24)$$

For this distribution the space charge potential is proportional to the external applied rf potential. In order to compensate the repulsive space charge force and conserve the matched phase space distribution the rf voltage U_0 has to be increased by the factor $1 + Y_{sc}/Y_{rf}$.

For the study of particle dynamics the electromagnetic interaction of the particle beam is often described in frequency domain. The generated voltage in frequency domain is given by

$$U(\omega) = -Z(\omega)I(\omega), \quad (2.25)$$

where $I(\omega)$ and $Z(\omega)$ denote the current of the ion beam and the longitudinal beam coupling impedance. The impedance is calculated by the integral of the longitudinal

electric field components $E_{\parallel}(s, \omega)$ along the reference trajectory (for more information see Ref. [28])

$$Z_{\parallel}(\omega) = -\frac{1}{I(\omega)} \int E_{\parallel}(s, \omega) ds. \quad (2.26)$$

Due to the periodicity of the circulation in the accelerator, the frequency dependence is often expressed by higher harmonics $n = \omega/\omega_{rev}$ of the revolution frequency in the circular accelerator. The beam current in the n -th harmonic is given by $I_n = \beta c_0 q \lambda_n$ with the wavelength $\lambda_n = L_{acc}/n$. The longitudinal space charge impedance in the long wavelength limit results in (see Ref. [32])

$$\frac{Z_n^{sc}}{n} = -i \frac{Z_0 g}{2\beta\gamma^2}, \quad (2.27)$$

where $Z_0 = (\epsilon_0 c_0)^{-1}$ denotes the vacuum impedance. Equation 2.27 is valid for frequencies below the space charge cut off frequency, which is given by (see Ref. [33, 34])

$$f_c = \frac{\beta c_0 \gamma}{\pi a \sqrt{g}}. \quad (2.28)$$

Above the cut off frequency the longitudinal electric field is damped. The space charge impedance is characterized by (see Ref. [35])

$$\frac{Z_n^{sc}}{n} = -i \frac{Z_0 g}{2\beta\gamma^2} \frac{1}{1 + \left(\frac{n}{n_c}\right)^2}, \quad (2.29)$$

where $n_c = 2\pi f_c/\omega_0$ is the corresponding harmonic number of the space charge cut off.

2.3 Intra Beam Scattering

In a synchrotron the mean velocities in the different degrees of freedom usually deviate. The difference is generated by longitudinal acceleration, intensity effects, imperfections of the accelerator lattice or beam cooling. Similar to a gas or a plasma at rest, the different degrees of freedom couple with each other by elastic coulomb scattering events. The thermal relaxation between the three degrees of freedom by multiple small angle coulomb scattering events is called intra beam scattering (IBS). In synchrotrons that are operating below transition energy ($\gamma < \gamma_T$), temperature is transferred between the

longitudinal and the two transverse components of motion until the mean velocity in all directions is equal. This equilibrium state is reached when (see Ref. [36])

$$\frac{\sigma_\delta}{\gamma} \approx \sigma_{x'} \approx \sigma_{y'}, \quad (2.30)$$

where $\sigma_{\delta, x', y'}$ denotes the rms spread in momentum and transverse divergence of the particle beam. For ultra relativistic beams, especially during a longitudinal cooling process, the transverse velocities are typically much higher compared to the longitudinal velocity $\frac{\sigma_\delta}{\gamma} < \sigma_{x', y'}$. As a result IBS leads to a heating of the longitudinal motion and cooling of the transverse motion.

A general expression for growth rates of Gaussian beam profiles due to IBS is derived by Jie Wei in Ref. [36]. The growth rates can be determined by lattice parameters that are averaged over the ring circumference. The growth rates of the three coordinates are given by

$$\left(\begin{array}{c} \tau_x^{-1} \\ \tau_y^{-1} \\ \tau_\delta^{-1} \end{array} \right)_{IBS} = \frac{q^4 L_c \langle \beta_x \rangle \langle \beta_y \rangle \cdot \lambda}{32 \pi^{5/2} m^2 \epsilon_0^2 \beta^3 \gamma^4 c_0^3 \sigma_\delta^2 \sigma_x^2 \sigma_y^2} \cdot F_{Wei} \cdot \left(\begin{array}{c} -\frac{1}{2} a_{Wei}^2 + d_{Wei}^2 \\ -\frac{1}{2} b_{Wei}^2 \\ 1 - d_{Wei}^2 \end{array} \right), \quad (2.31)$$

where F_{Wei} , b_{Wei} , a_{Wei} and d_{Wei} are functions depending on beam parameters. The functions are described in general form in Ref. [36] and are simplified for the specific example of the longitudinal cooling process of a relativistic ion beam. For longitudinal bunch beams with a rms bunch length of σ_z the ion line density is given by $\lambda = \frac{N_p}{2\sqrt{\pi}\sigma_z}$. The coulomb logarithm $L_c \approx 20$ is set to a fixed value in this model. We restrict the study to beams below transition energy ($\gamma \ll \gamma_T$) and to ion beams with a smaller velocity deviation in longitudinal direction than in transverse direction ($\frac{\sigma_\delta}{\gamma} < \sigma_{x', y'}$). For simplicity we assume both transverse coordinates to have equal beam parameters and the horizontal dispersion to be small ($D_p \delta \ll \sigma_x$). Under these constraints the four functions reduce to

$$d_{Wei} \approx \frac{D_p \sigma_\delta}{\sigma_x}; \quad a_{Wei} \approx b_{Wei} \approx \frac{\sigma_\delta}{\gamma \sigma_{x'}}; \quad F_{Wei} \approx \frac{\pi \gamma \sigma_{x'}}{2 \sigma_\delta}. \quad (2.32)$$

Applying the simplified functions to Eq. 2.31 and neglecting the horizontal dispersion, the longitudinal IBS growth rate of the rms momentum spread σ_δ is calculated by

$$\tau_\delta^{-1} = \tau_{IBS}^{-1} = \frac{q^4 L_c}{128 \pi^2 m^2 \epsilon_0^2 \beta^3 \gamma^3 c_0^3 \sigma_\delta^2 \sigma_z \epsilon_\perp^{3/2} \sqrt{\langle \beta_x \rangle}}, \quad (2.33)$$

where $\langle \beta_x \rangle$ is the average beta function.



3 Doppler Laser Cooling

Doppler laser cooling is a technique to cool an ion ensemble to very low temperatures [20]. It was originally successfully used in ion traps and later applied to stored ions in circular accelerators [21]. In this chapter the principle of Doppler laser cooling is explained. Section 3.1 starts with a description of the photon ion interaction in particle traps and Sect. 3.2 describes the transfer of the cooling process from a trap to a circular accelerator and the main differences.

3.1 Principle of Doppler Laser Cooling

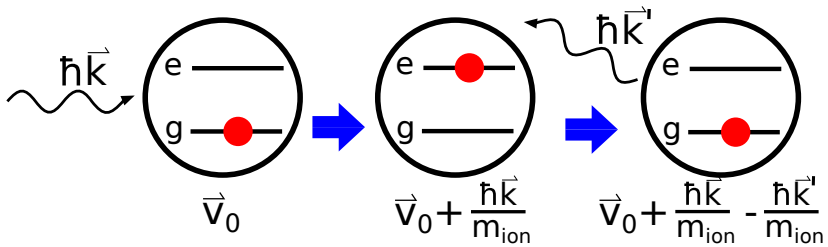


Figure 3.1: Single resonant ion-photon interaction: The ion absorbs an incoming photon and the electron (red) is moved from the ground state (g) into the excited state (e). The excited state is not stable and the ion deexcites by a spontaneous emission in a random direction.

The principle of Doppler laser cooling of a stationary ensemble relies on the resonant interaction of laser light with an atomic transition of the ions. The resonant interaction is illustrated in fig. 3.1. The atomic transition can absorb a photon if the resonance condition is fulfilled. The condition requires the photon energy to be equal to the energy gap of the atomic transition

$$E_e - E_g = \hbar k_t c_0 = \frac{\hbar c_0 2\pi}{\lambda_t}, \tag{3.1}$$

where E_g and E_e are the energies of the ground and excited state, \hbar the Planck constant and λ_t , k_t the wavelength and the absolute value of the wave number of the resonant laser photons.

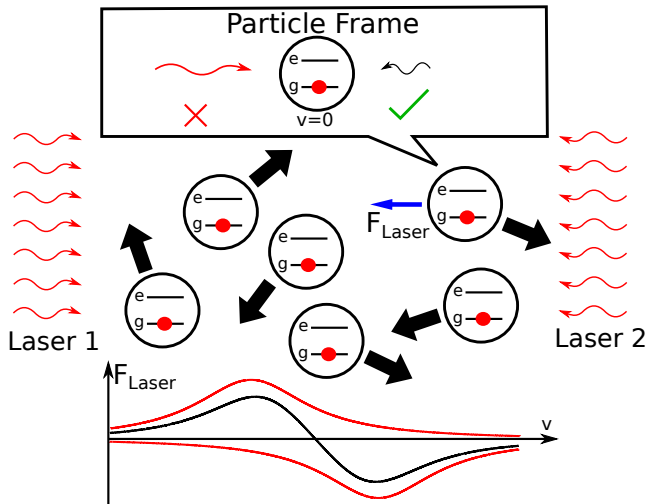


Figure 3.2: Illustration of the Doppler laser cooling process in a particle trap in one dimension. Laser beams point from all directions towards the ion ensemble. The energy of the photons is slightly below the energy gap of the atomic transition. In the particle rest frame the two laser beams are Doppler shifted. The photons, coming from the right hand side, match to the transition, and the ion is decelerated. The two forces from the laser beams are plotted in red and the sum of both produce an approximately linear friction force (black).

The absorption of a photon pushes the ion into the excited state and transfers the momentum of the photon to the ion. After the lifetime of the excited state τ_{se} the ion deexcites by emitting a photon spontaneously. The spontaneous emissions are not restricted to a particular direction but are isotropically distributed. After many absorptions and spontaneous emissions, the mean momentum change of the spontaneous emissions cancels ($\langle \hbar \vec{k}' \rangle = 0$). The remaining momentum change of the absorbed photons points always in the direction of the laser beam and gives a net momentum transfer to the ions.

For the cooling process the ion is described by a two level system with the ground state and one excited state. The scattering rate k_{trap} under influence of a continuous laser intensity I is (see Ref. [37])

$$k_{trap} = \frac{1}{2\tau_{se}} \frac{S}{1 + S + 4 \cdot (k_t - k_L^{PF})^2 \cdot \tau_{se}^2 / c_0^2}, \quad (3.2)$$

where $S = I/I_s$ and $I_s = (k_L^3 \hbar c_0)/(12\pi\tau_{se})$ the saturation intensity. The wave number of the incoming photons is k_L^{PF} . The origin of Eq. 3.2 is described in detail in Sect. 3.2.1. The multiplication of the scattering rate k_{trap} and the mean momentum transfer of each spontaneous emission $\hbar k_L^{PF}$ results in the force, acting on the ions. The scattering rate and the laser force depend on the difference of the resonant wave vector and the wave vector of the incoming laser photons. For moving ions the wave vector of the laser photons k_L has to be transformed into the co-moving frame of the ion. The laser photons are Doppler shifted by

$$k_L^{PF} = k_L \cdot \sqrt{\frac{c_0 + v}{c_0 - v}}, \quad (3.3)$$

where v is the velocity of the ion and k_L^{PF} , k_L the wave vector in the ion reference frame and the frame of the laser system. The velocity dependence of the laser wavelength, which is seen by the ions, creates a velocity dependent force.

For the cooling process laser beams are pointed towards the ion ensemble from all 6 directions as shown in fig. 3.2 for one dimension. The energy of the photons is slightly below the energy of the atomic transition. Due to the Doppler shift the laser beams are in resonance with ions which are moving towards the laser. The momentum transfer in the opposite direction decelerate the ions. The combined force of two counter-propagating red-shifted laser beams results in an approximately linear friction force (see fig. 3.2) and cools the ion ensemble.

3.2 Laser Cooling Force in Accelerators

Doppler laser cooling of an ion ensemble in an accelerator is based on the same principle as laser cooling in an ion trap. The major difference is the high directional velocity of the ions in an accelerator compared to the stationary ion ensemble in an ion trap. Describing the accelerated ion ensemble in the co-moving frame, which is explained in Sect. 2.1, the properties of the ions are similar to those of an ion trap.

For the laser cooling process the laser light has to be transformed into the co-moving coordinate system of the ions. The high velocity of the co-moving frame with respect to the laboratory frame leads to a strong Doppler shift of the laser wavelength. In the co-moving frame the wavelength of the parallel laser beam increases, while the wavelength of the anti-parallel laser beam decreases. In order to match the resonance condition (see Eq. 3.1) of the atomic transition, the laser systems have to satisfy the following equations

$$\lambda_{parallel}^{LF} = \frac{\lambda^{PF}}{\gamma \cdot (1 + \beta)} \quad (3.4)$$

$$\lambda_{anti-parallel}^{LF} = \lambda^{PF} \cdot \gamma \cdot (1 + \beta) = \lambda^{LF}, \quad (3.5)$$

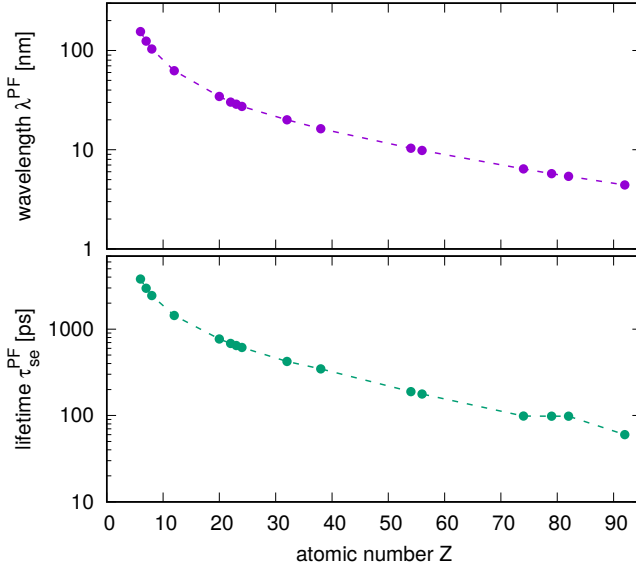


Figure 3.3: Transition wavelength of the $2s_{1/2} \rightarrow 2p_{1/2}$ transition and lifetime of the excited state in lithium-like ions. The data are taken from Ref. [38].

where λ^{PF} is the required wavelength of the atomic transition in the particle rest frame (PF) and λ^{LF} , $\lambda_{parallel}^{LF}$, $\lambda_{anti-parallel}^{LF}$ the wavelengths of the parallel and anti-parallel laser beam in the laboratory frame (LF).

The interaction of the ion beam with a perpendicular orientated laser beam is not possible. Beside the very small cross section of the two beams, the Doppler shift strongly depends on the angle between the ion and the perpendicular laser beam. Typical vibrations of the laser beam would lead to a permanently changing resonance condition. The uncontrollable fluctuations for a perpendicular laser beam prevent an efficient cooling process. Hence laser cooling is only applied to the longitudinal coordinate for accelerated ion ensembles (see Ref. [39]).

This investigation concentrates on the atomic transition $2s_{1/2} \rightarrow 2p_{1/2}$ in lithium-like ions. Lithium-like ions consist of the atomic nucleus and three electrons. The resonance wavelength λ^{PF} and the lifetime of the excited state τ_{se} are shown in fig. 3.3. The resonant wavelengths in PF are in the nm -range and decrease for ions with a higher atomic number. For relativistic beam velocities of the ion beam, the required wavelength for the parallel laser beam in LF (see Eq. 3.4) becomes unaffordably short. No powerful laser systems exist which provide the required wavelength for the parallel laser beam. Consequently, only anti-parallel laser light can be used for the cooling process of rel-

ativistic ion beams. In the following the wavelength of the anti-parallel laser light is $\lambda^{LF} = \lambda_{anti-parallel}^{LF}$.

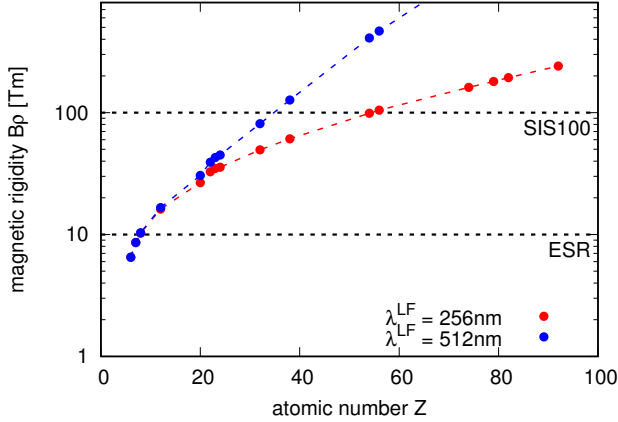


Figure 3.4: Required magnetic rigidity $B\rho$ for the resonant condition of the Doppler shifted laser photons and the atomic transition. The results are shown for lithium-like ions using transition data from fig. 3.3. The correlation was original shown in Ref. [39].

For the laser cooling project in the SIS100 at FAIR laser systems with two different wavelengths (256 nm and 512 nm) will be available (for more information see Ref. [25]). The resonance condition and the Doppler shift generate a fixed correlation between the wavelength of the atomic transition, the wavelength of the laser system and the velocity of the ideal particle in the accelerator. The correlation is given by Eq. 3.5. For the investigated transition (see fig. 3.3) and the two available wavelengths at the SIS100 the required magnetic rigidity is calculated by Eq. 2.2 and shown in fig. 3.4. The cooling process of heavy ion beams require a high magnetic rigidity. For the $2s_{1/2} \rightarrow 2p_{1/2}$ transition in lithium-like ions the SIS100 is able to cool ions up to xenon. The cooling process for ions heavier than xenon requires alternative transitions with a smaller energy gap.

The typical setup of a Doppler laser cooling experiment in a circular accelerator is illustrated in fig. 3.5. The ions are guided by dipole magnets on the reference orbit in the synchrotron and interact with the laser light on one straight section. Due to the presence of superconducting dipole magnets in the SIS100, the ion beam is not merged with the laser beam in the bending magnets. In this case the laser beam is guided by mirrors into the vacuum pipe on the straight section. The ion beam is merged with the laser beam by the dipole field which arises off axis in the quadrupole magnets. A small

angle in the vacuum chamber is sufficient for an overlap with the laser beam without a disturbance of the ion beam by the laser mirrors, as described in Ref. [25].

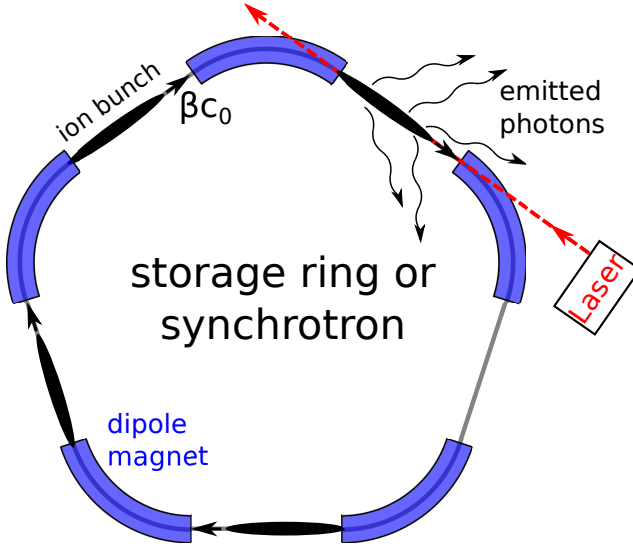


Figure 3.5: Sketch of the interaction section of the laser beam and the circulating ions. The ion bunches travel on the reference orbit in the synchrotron. On one straight section the ions are merged with the anti-parallel laser beam. The interaction section in the SIS100 slightly differs and is explained in more detail in Ref. [25].

The force of the laser ion interaction for relativistic ion beams depends on the spontaneous emission rate and the transferred momentum of each scattered photon. The transferred momentum is a combination of the momenta of the incoming and outgoing photons as illustrated in fig. 3.1. Each resonant interaction changes the momentum of the ion by

$$\Delta\vec{p}^{PF} = \Delta\vec{p}_{absorb}^{PF} - \Delta\vec{p}_{emit}^{PF} \quad (3.6)$$

in the PF. The momenta of the incoming photon $\Delta\vec{p}_{absorb}^{PF}$ and the emitted photon $\Delta\vec{p}_{emit}^{PF}$ are given by

$$\Delta\vec{p}_{absorb}^{PF} = \frac{2\pi\hbar}{\lambda^{PF}} \cdot \begin{pmatrix} 0 \\ 0 \\ -1 \end{pmatrix}; \quad \Delta\vec{p}_{emit}^{PF} = \frac{2\pi\hbar}{\lambda^{PF}} \cdot \begin{pmatrix} \sqrt{1-U^2} \cos(\Theta) \\ \sqrt{1-U^2} \sin(\Theta) \\ U \end{pmatrix} \quad (3.7)$$

in the co-moving coordinate system. The emitted photon is isotropically radiated. The random direction is expressed by two uniformly distributed random numbers $U \in [-1, 1]$ and $\Theta \in [0, 2\pi)$. The momentum change in the LF is calculated by the Lorentz transformation of the incoming and emitted photons. After the forward Lorentz transformation of the emitted photon and a backward Lorentz transformation of the absorbed photon with the velocity of the PF ($u_z = \beta\gamma c_0$) the momenta in the LF result in

$$\Delta \vec{p}_{absorb}^{LF} = \frac{2\pi\hbar}{\lambda^{LF}} \cdot \begin{pmatrix} 0 \\ 0 \\ -1 \end{pmatrix}; \quad \Delta \vec{p}_{emit}^{LF} = \frac{2\pi\hbar}{\lambda^{LF}} \cdot \gamma \cdot (1 + \beta) \cdot \begin{pmatrix} \sqrt{1-U^2} \cos(\Theta) \\ \sqrt{1-U^2} \sin(\Theta) \\ \gamma(\beta + U) \end{pmatrix}, \quad (3.8)$$

where λ^{LF} describes the wavelength of the incoming photon in the LF. The combined momentum transfer in longitudinal direction for a spontaneous emission normalized to the momentum of the ideal particle p_0 yields

$$\Delta \delta^{LF} = \frac{\Delta p_z^{LF}}{p_0} = \frac{2\pi\hbar}{\lambda^{LF} p_0} \cdot \gamma^2 \cdot (1 + \beta) \cdot (1 + U). \quad (3.9)$$

Due to the statistical nature of the spontaneous emission, the transferred momentum change depends on the random direction of the emission. The mean momentum transfer is given by

$$\langle \Delta \delta^{LF} \rangle = \frac{2\pi\hbar}{\lambda^{LF} p_0} \cdot \gamma^2 \cdot (1 + \beta). \quad (3.10)$$

The ratio of the mean momentum transfer for the emitted photon and the absorbed photon is

$$\frac{\langle \Delta p_z^{LF} \rangle_{emit}}{\Delta p_z^{LF} \text{ absorb}} = \gamma^2 (1 + \beta) - 1. \quad (3.11)$$

For stationary ensembles and low energy beams ($\beta \ll 1$) the emitted photons are isotropically distributed and the mean momentum transfer of the emissions vanishes. The mean momentum transfer is given by the absorbed photons. In contrast for high energy beams ($\beta \approx 1$) the emitted photons are concentrated in the forward direction and Doppler shifted twice. Hence the main momentum transfer originates in the emitted photons.

The frequency of occurrence of a resonant interaction is given by the spontaneous emission rate k_{se}^{PF} , that is calculated by (see Ref. [37])

$$k_{se}^{PF}(\delta, t) = \rho_{ee}(\delta, t) \cdot \frac{1}{\tau_{se}^{PF}}, \quad (3.12)$$

where $\rho_{ee}(\delta, t)$ is the excitation probability and τ_{se}^{PF} the lifetime of the excited state. The integration of the emission rate over a time interval $[t_1, t_2]$ results in the average number of scattered photons per ion

$$n_{scat}(\delta) = \int_{t_1}^{t_2} k_{se}^{PF}(\delta, t) dt. \quad (3.13)$$

Neglecting the statistical component, the strength of the ion laser interaction can be expressed by an averaged force of

$$\langle F_L^{LF}(\delta) \rangle = \langle \Delta p^{LF} \rangle \cdot \langle k_{se}^{LF}(t, \delta) \rangle \quad (3.14)$$

For the two level system the probability of an ion being in the excited state ρ_{ee} is calculated by the optical Bloch equations (see Ref. [37])

$$\frac{d\rho}{dt} = \frac{i}{\hbar} [\rho, \mathcal{H}] - \frac{1}{\tau_{se}} \rho. \quad (3.15)$$

The brackets represent the commutator $[A, B] = A \cdot B - B \cdot A$. The density matrix ρ and the Hamiltonian \mathcal{H} of the two level system are given by

$$\rho = \begin{pmatrix} \rho_{ee} & \rho_{eg} \\ \rho_{ge} & \rho_{gg} \end{pmatrix}; \quad \mathcal{H} = \begin{pmatrix} \hbar\omega_e & (\frac{\hbar}{2}\Omega_{rabi})e^{-i\omega t} \\ (\frac{\hbar}{2}\Omega_{rabi})e^{i\omega t} & \hbar\omega_g \end{pmatrix}. \quad (3.16)$$

All values are evaluated in the PF and $\Omega_{rabi} = \sqrt{I(t)/2I_S} \cdot 1/\tau_{se}$ describes the Rabi frequency. The equations can be solved for arbitrary laser intensities $I(t)$. In the following the excitation probability for two different laser scenarios is discussed. For simplicity we assume that the transverse laser beam spot covers the whole particle beam equally.

3.2.1 Continuous Wave Excitation

The ordinary solution for laser cooling is to use a continuous wave (cw) laser system. The particles circulate in the accelerator and interact with the laser along one straight section with the length $L_{interact}$ as shown in fig. 3.5. Each turn the particles see a rectangular laser pulse with a duration of

$$\Delta t_{cw}^{PF} = \frac{L_{interact}}{\gamma\beta c_0}. \quad (3.17)$$

The numerical solution of the optical Bloch equations for the cw laser excitation is shown in fig. 3.6. Usually the interaction time is long compared to the life time of the excited state ($\Delta t_{cw}^{PF} \gg \tau_{se}^{PF}$) and the excitation probability levels on a constant value. For long interaction times, the excitation probability can be approximated with a rect-

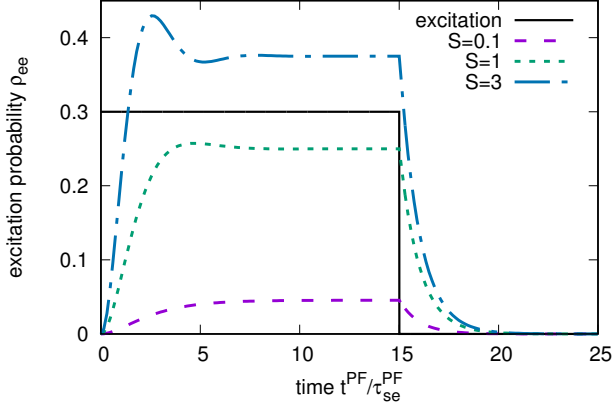


Figure 3.6: Excitation probability for the excitation with a cw laser for three different laser intensities. After approximately $3 \cdot \tau_{se}^{PF}$ the probability reaches a steady state.

angular shape. For a constant excitation probability ($d\rho_{ee}/dt = 0$) the optical Bloch equations can be solved analytically (see Ref. [37]) and result in

$$\rho_{ee}(\delta) = \frac{1}{2} \frac{S}{1 + S + (2\zeta(\delta - \delta_{LPos}) \cdot \tau_{se}^{PF})^2} \quad (3.18)$$

$$\xi = \frac{d\omega}{d\delta} = \frac{2\pi c_0}{\lambda_{PF}} \beta \gamma (1 + \beta), \quad (3.19)$$

where $S = \frac{I_s^{PF}}{I_s^{LF}} = \frac{I_s^{LF}}{I_s^{PF}}$ describes the saturation parameter, δ the relative momentum deviation of a test particle and δ_{LPos} the position of the laser in units of relative momentum. The mean number of scattering events per turn is given by

$$n_{scat}^{turn}(\delta) = \frac{L_{interact}}{\gamma \beta c_0} \cdot \frac{1}{2\tau_{se}^{PF}} \frac{S}{1 + S + (2\zeta(\delta - \delta_{LPos}) \cdot \tau_{se}^{PF})^2}. \quad (3.20)$$

The required laser intensity in the LF for saturation is (see Ref. [27])

$$I_s^{LF} = I_s^{PF} \cdot \frac{1}{\gamma^2(1 + \beta)^2} = \frac{2\pi^2 \hbar c_0}{3\lambda_{LF}^3 \tau_{se}^{PF}} \cdot \gamma(1 + \beta). \quad (3.21)$$

For the $2s_{1/2} \rightarrow 2p_{1/2}$ transition in lithium-like ions the saturation intensity is shown in fig. 3.7. The saturation intensity increases strongly for higher beam energies. If the laser intensity is far below the saturation intensity of the transition, the number of scattering events decreases as described by Eq. 3.18 and laser cooling becomes inefficient. At higher magnetic rigidities the required laser power for a typical beam cross-section of several mm^2 substantially exceeds the output power of existing ultra-violet laser systems (256 nm). As an alternative, cooling with a wavelength of 512 nm looks promising, because the saturation intensity is lower and laser systems with higher laser power are available.

The width of the function $\rho_{ee}(\delta)$ and consequently the width of the laser force in units of relative momentum is given by

$$\Delta_{fwhm} = \frac{\sqrt{1+S} \cdot \lambda^{LF}}{2\pi\tau_{se}^{PF}(1+\beta)\beta\gamma c_0}. \quad (3.22)$$

Assuming a saturated transition ($S = 1$), the width of the laser force for the investigated transition in lithium-like ions is in the range of $\Delta_{fwhm} \approx 5 \cdot 10^{-8}$ (discussed in more detail in Sect. 7.1). The width is much smaller than the initial momentum spread of a typical relativistic ion beam. The cooling technique of an ion ensemble with a significant higher momentum spread than the width of the cooling force is described in Sect. 5.1.

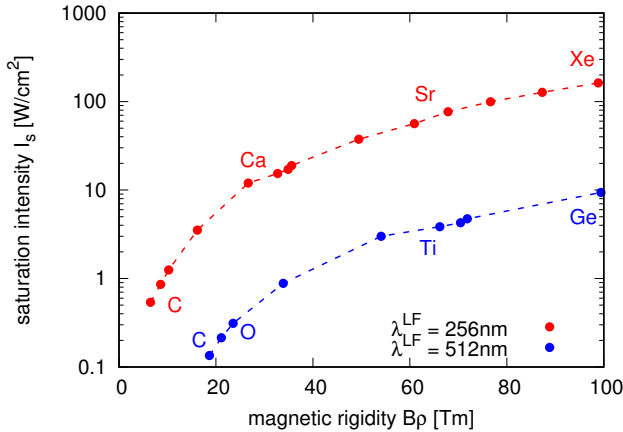


Figure 3.7: Saturation intensity for cw laser excitation. For higher relativistic factors the required intensity increases significantly. The results are shown for lithium-like ions using transition data from fig. 3.3. Different dots represent different ions that are partly marked by name.

3.2.2 Pulsed Laser Excitation

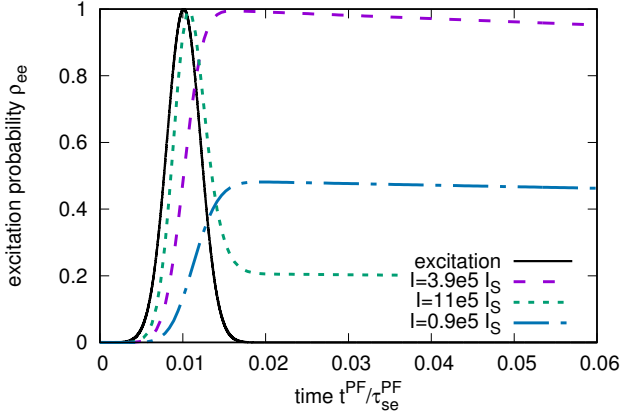


Figure 3.8: Excitation probability over time for different intensities of the pulsed laser system. During the laser pulse the ions perform Rabi oscillations. After the pulse the excitation slowly decays by spontaneous emissions.

The second option is to use a pulsed laser system [40, 41]. A short pulse length in time domain increases the spectral width of the laser light (see Ref. [42]). For a Gaussian laser pulse with a standard deviation of σ_t^{LF} in time the width of the laser force in units of relative momentum can be calculated by (see Ref. [40]):

$$\sigma_{\delta_{Laser}} = \frac{1}{p} \frac{dp}{d\lambda^{LF}} \sigma_{\lambda}^{LF} = \frac{\lambda^{LF}}{2\pi c_0 \beta \sigma_t^{LF}} \quad (3.23)$$

$$\sigma_t^{PF} = \sqrt{\frac{1-\beta}{1+\beta}} \cdot \sigma_t^{LF} \quad (3.24)$$

The excitation of an ion ensemble with short laser pulses ($\sigma_t^{PF} \ll \tau_{se}$) is no longer described by the well known steady state solution (Eq. 3.18). For the calculation of the required laser intensity and strength of the laser force, we assume the pulses to be short compared to the lifetime of the excited state ($\sigma_t^{PF} \ll \tau_{se}^{PF}$). As a consequence at most only one spontaneous emission per laser pulse can take place. The goal of the excitation with a short laser pulse is to have all ions in the excited state after the pulse. After the pulse is gone all ions spontaneously emit one photon. The optical Bloch equations (see

Eq. 3.15) are simplified for an infinite long lifetime of the excited state $1/\tau_{se} = 0$ to (all values are given in the PF)

$$\frac{d^2(\rho_{ee} - \rho_{gg})}{dt^2} = -\Omega_{rabi} \cdot (\rho_{ee} - \rho_{gg}). \quad (3.25)$$

With the constrains $\rho_{gg} + \rho_{ee} = 1$ and $\rho_{ee} = 0$ at $t = 0$ the excitation probability of the Rabi oscillator is

$$\rho_{ee}(t) = -\frac{1}{2} \cos(\Omega_{rabi} t) + \frac{1}{2}. \quad (3.26)$$

The intended state after the pulse is $\rho_{ee} = 1$. If the pulse energy is too low, some particles are still in the ground state whereas if the pulse energy is too high, the stimulated emission decreases the amount of ions in the excited state as shown in fig. 3.8. For analytic calculations the Gaussian pulse is approximated by a rectangular pulse with the same peak intensity. The length of the corresponding rectangular pulse is determined by the integral of the Rabi frequency over time that has to be equal for both pulse shapes.

$$\rho_{excit} = \rho_{ee}(\tau_{rec\ pulse}) = -\frac{1}{2} \cos(\Omega_{rabi} \cdot \tau_{rec\ pulse}) + \frac{1}{2} \stackrel{!}{=} 1 \quad (3.27)$$

$$\tau_{rec\ pulse} = \sqrt{4\pi} \cdot \sigma_t \quad (3.28)$$

The ideal laser peak intensity is

$$\frac{\hat{I}_S^{PF}}{I_S^{PF}} = \frac{\hat{I}_S^{LF}}{I_S^{LF}} = \frac{\pi}{2} \cdot \left(\frac{\tau_{se}^{PF}}{\sigma_t^{PF}} \right)^2. \quad (3.29)$$

The analytically calculated peak intensity agrees with the results of the numerically solved Bloch equations in fig. 3.8. The optimum average laser intensity is found to be

$$I_{avg} = f_{rep} \cdot \sqrt{2\pi} \cdot \frac{\pi}{2} I_S^{LF} \cdot \frac{\tau_{se;PF}^2}{\sigma_t^{LF}} \cdot \frac{1+\beta}{1-\beta}, \quad (3.30)$$

where all parameters are determined in the LF except the lifetime of the excited state τ_{se}^{PF} . The required average intensity for the pulsed laser is depicted in fig. 3.9. The intensity scales linearly with the spectral width, respectively inversely proportional with the pulse length.

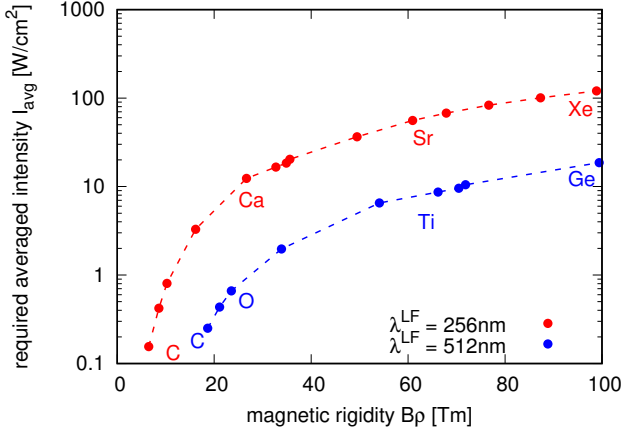


Figure 3.9: Required average intensity of pulsed laser system for $\sigma_{\delta Laser} = 10^{-5}$. The intensity scales linearly with $\sigma_{\delta Laser}$. The values are calculated for $f_{rep} = f_{rev} \approx 278$ kHz in the SIS100. The results are shown for lithium-like ions using transition data from fig. 3.3. Different dots represent different ions that are partly marked by name.

The probability of a scattering event in the interaction section for a pulsed laser excitation is given by

$$\rho_{scat}(\delta) = \rho_{excit}(I) \cdot \rho_{syn} \cdot e^{-\frac{1}{2} \left(\frac{\delta_L Pos - \delta}{\sigma_{\delta Laser}} \right)^2} \quad (3.31)$$

$$\rho_{syn} = \begin{cases} \frac{f_{rep}}{f_{rev}} \cdot \frac{(1+\beta) \cdot L_{interact}}{L_{acc}}, & \text{(not synchronized)} \\ \frac{f_{rep}}{f_{rev}}, & (f_{rep} < f_{rev} \text{ synchronized}) \\ 1, & (f_{rep} \geq f_{rev} \text{ synchronized}) \end{cases} \quad (3.32)$$

where $\rho_{excit}(I)$ is the excitation probability ρ_{ee} directly after the laser pulse (see Eq. 3.27). In case the repetition rate f_{rep} is not synchronized to the revolution frequency of the bunches f_{rev} the position of the laser pulses is randomly distributed and all bunches in the ring will interact with the laser. For a synchronized condition one bunch interacts with the laser pulses and is cooled more efficiently. Note that for long bunches the laser acts only on ions in an area of $(1+\beta)L_{interact}$. On a small accelerator like the ESR the synchronization only results in a gain of 2.9 whereas for the SIS100 the factor is 20.8. The averaged relative momentum kick per turn of a pulsed laser results in

$$\Delta \delta_{turn}^{pulsed}(\delta) = \langle \Delta \delta^{LF} \rangle \cdot \rho_{excit}(I) \cdot \rho_{syn} \cdot e^{-\frac{1}{2} \left(\frac{\delta_L Pos - \delta}{\sigma_{\delta Laser}} \right)^2} \quad (3.33)$$

The impact of the pulsed laser excitation on the dynamics of the ions is discussed in Sect. 5.2.

4 Simulation Model

The availability of physical experiments is usually strictly limited in time. Especially experiments with relativistic ion beams in modern accelerator facilities are expensive and require a lot of preparation. In order to study physical effects more efficiently and support experimental investigations, numerical simulations of the underlying process are very useful. Besides, numerical simulations easily give visualization of the complete phase space information of the ion beam, while experiments typically measure only single projections of the phase space distribution. Furthermore, numerical simulations enable to investigate experiments for future facilities. During the planning of the experimental setup, the impact of different configurations on the success and accuracy of the final experiment can be studied.

For the numerical simulation of a particle ensemble, the interaction and forces have to be reduced to a model that covers all important processes for the investigation. Simulation models usually restrict the variables to a certain range in which the physical processes of the ensemble are properly described. For the simulation study of the Doppler laser cooling process the temperature of the ion ensemble varies over a broad range. A quantity which is often used to express the regime of particle interaction of an ion ensemble is given by the plasma parameter

$$\Lambda = 4\pi n \lambda_D^3 = \frac{4\pi (\epsilon_0 k_B T)^{3/2}}{n^{1/2} q^3} \quad (4.1)$$

where λ_D is the Debye length and n the ion density.

For low temperatures of the ion ensemble the plasma parameter is small ($\Lambda \lesssim 1$) and the kinetic energy of the ions is in the same range as the potential energy between the ions. The motion of the ions depends strongly on the single interaction between two ions. This regime is called strongly coupled plasma. On the other hand for high values of the plasma parameter ($\Lambda \gg 1$) the ions have a high temperature and consequently a high relative velocity. The single interaction between two particles becomes less important and the particle interaction is described by mean fields. This regime is called weakly coupled plasma.

The motion of the particles in the strongly coupled regime is typically simulated by molecular dynamic codes (see Ref. [43]). In the weakly coupled regime the model assumes that the particles produce a smooth distribution in phase space $f(\vec{r}, \vec{p})$. The

evolution of the smooth distribution function is described by a Boltzmann equation (see Ref. [44]). Concentrating on the longitudinal motion, the Boltzmann equation is

$$\frac{\partial f}{\partial t} + v_z \frac{\partial f}{\partial z} + \frac{F_z}{p_0} \frac{\partial f}{\partial \delta} = \left(\frac{\partial f}{\partial t} \right)_{collision}, \quad (4.2)$$

where v_z is the longitudinal velocity, F_z the longitudinal force and $\left(\frac{\partial f}{\partial t} \right)_{collision}$ the elastic collision term.

The initially hot ion bunch in a circular accelerator is typically in the weakly coupled regime while the ion ensemble can reach the strongly coupled regime after the laser cooling process. However this work concentrates on the particle dynamics during the cooling process, which are located in the weakly coupled regime. Hence the description with mean fields leads to accurate results for the particle dynamics during the cooling process. The final state after the cooling process might be inaccurate and would need a more detailed description of the single particle interactions.

The particle dynamics of the laser cooling process are investigated by solving numerically the Boltzmann equation given by Eq. 4.2. The distribution function is described in the co-moving coordinate system, which is introduced in Sect. 2.1. In this work, the focus is on the longitudinal behavior of the ion beam and the transverse phase space is assumed to be constant. The validity of this assumption is discussed in detail in Sect. 7.3. Thus, the simulation of the particle dynamics is restricted to the longitudinal position z and the longitudinal relative momentum deviation δ .

The Boltzmann equation is solved by the PIC (particle-in-cell) method (see Ref. [45]). The distribution function $f(z, \delta)$ is represented by macro particles ($M_p \approx 10^5 - 10^7$). Each macro particle has a position z_i and δ_i in phase space and carries the charge and mass of N_p/M_p particles, where N_p and M_p describe the total number of real particles and macro particles of the simulated ensemble. In order to calculate the distribution function the macro particles are scattered on a grid with N_{Grid} cells. The differential equation is solved using the leapfrog method (see Ref. [46]). After each time step Δt the position and momentum of each macro particle is updated by

$$z \left(t + \frac{\Delta t}{2} \right) = z \left(t - \frac{\Delta t}{2} \right) + v_z(\delta(t)) \cdot \Delta t \quad (4.3)$$

$$\delta(t + \Delta t) = \delta(t) + F \left(z \left(t + \frac{\Delta t}{2} \right), t + \frac{\Delta t}{2} \right) \cdot \Delta t, \quad (4.4)$$

where v_z is the velocity in the co-moving coordinate system, which is calculated by Eq. 2.9. The force $F(z, t)$ consists of the externally applied rf voltage for the creation of buckets $F_{rf} = q \cdot U_{rf}(z, t)$ and inter particle forces, that are described in the following section. The change of the particle position during one time step must not exceed the width of a cell which is described by the Courant-Friedrichs-Lewy condition (see Ref. [47]).

The simulation code is implemented in Python (see Ref. [48]). In order to enable the simulation of the ion bunch over several seconds, time consuming routines are written in Cython (see Ref. [49]). The initial ion bunch is approximated by a matched elliptic phase space distribution.

4.1 Intensity Effects

Beside the externally applied forces the motion of the ions in phase space is affected by intensity dependent inter particle interactions. The physical background of the two main intensity effects in the weakly coupled regime is explained in Sect. 2.2 and 2.3. For the implementation of the space charge forces into the tracking code the electric field of the particle distribution is calculated. As described by Eq. 2.22 the particle induced longitudinal electric field depends only on the longitudinal line density $\lambda(z)$. For a PIC-code the line density on the grid point m is calculated by

$$\lambda_m = \frac{1}{\Delta z_{Grid}} \sum_{j=0}^{M_p-1} S\left(\frac{z_j - z_m}{\Delta z_{Grid}}\right) \quad (4.5)$$

where Δz_{Grid} is the distance between two grid points, z_j/z_m the longitudinal position of the j -th ion/ m -th grid point and the function $S(l)$ describes the shape of the macro particles. For this investigation the particles are distributed onto their neighboring grid points and the function is given by a triangular shape

$$S(l) = (1 - |l|) \cdot \Theta(1 - |l|), \quad (4.6)$$

where $\Theta()$ denotes the Heaviside step function.

The electric field at the grid points is determined in frequency domain. As described by Eq. 2.29 space charge is described by an impedance in frequency domain. Applying two FFTs (fast Fourier transformations) the space charge induced voltage U_m at the grid points is calculated by

$$I_n = FFT[q \cdot \beta c_0 \cdot \lambda_m] \quad (4.7)$$

$$U_m = FFT^{-1}[-Z_n \cdot I_n] \quad (4.8)$$

where I_n is the spectral ion current and Z_n the space charge impedance calculated by Eq. 2.29. The longitudinal electric space charge field $E_z(z)$ is calculated equivalently to Eq. 4.5 by

$$E_z(z) = \frac{1}{L_{acc}} \sum_{m=0}^{N_{Grid}-1} U_m \cdot S\left(\frac{z - z_m}{\Delta z_{Grid}}\right). \quad (4.9)$$

The force in Eq. 4.4 consists of the Lorentz force (see Eq. 2.1) of the externally applied rf field and the space charge field.

The second intensity effect which is covered by the simulation tool, is intra beam scattering. The effect of multiple coulomb scattering events within the beam does not lead to a directional force, but to a diffusion. A diffusive component is not covered by Eq. 4.4, but is described by the Langevin equation (see Ref. [50]), which reads in the general form

$$p_i(t + \Delta t) = p_i(t) - K_i p_i(t) \Delta t + \sqrt{\Delta t} \sum_{j=1}^3 C_{i,j} Q_j, \quad (4.10)$$

where p_i are the momentum components in the three dimensions ($i = x, y, z$), K_i denote the friction coefficients, $C_{i,j}$ the coupling coefficients between the degrees of freedom and Q_j are Gaussian random numbers with unity standard deviation. During the laser cooling process the change of p_x and p_y is assumed to be negligibly small and the velocity spread to be much higher in transverse than in longitudinal direction ($\sigma_\delta/\gamma \ll \sigma_{x,y}$) as discussed in detail in Sect. 2.3. Equation 4.10 simplifies to (see Ref. [51])

$$\delta(t + \Delta t) = \delta(t) + Q \cdot \sqrt{2D_{IBS}\Delta t}, \quad (4.11)$$

where D_{IBS} denotes the relevant IBS diffusion coefficient. The statistical momentum change of IBS extends the coordinate update of Eq. 4.4 in each time step.

The correlation of the growth rate of the rms momentum spread and the diffusion coefficient is given by

$$\tau_\delta^{-1} = \frac{1}{\sigma_\delta^2} \frac{d\sigma_\delta^2}{dt} = \frac{D_{IBS}}{\sigma_\delta^2}. \quad (4.12)$$

The IBS growth rate assumes a Gaussian shaped bunch and is calculated by Eq. 2.33 for the Wei model. In the PIC tracking code the longitudinal bunch distribution does not have a Gaussian shape. The local diffusion model handles IBS heating for arbitrary line densities. The model is implemented in the simulation tool BETACOOOL [52] and is described in Ref. [51, 53]. The local diffusion coefficient for the Wei IBS model is given by

$$D_{IBS}(\lambda) = \frac{q^4 L_c}{64\pi^{3/2} m^2 \epsilon_0^2 \beta^3 \gamma^3 c_0^3 \epsilon_\perp^3 \sqrt{\langle \beta_x \rangle}} \cdot \lambda. \quad (4.13)$$

The local density λ at the position of each macro particle is determined by interpolation on a grid equivalent to the space charge field in Eq. 4.5 and 4.9.

Due to the finite number of macro particles the scattering on the grid produces noise on the ion density $\lambda(z)$. The created noise in the space charge field leads to a parasitic

increase of the longitudinal emittance. The heating by numerical noise is similar to the heating of IBS, but without physical meaning. For accurate results the emittance growth rate created by the grid noise should be kept well below the IBS growth rate.

4.2 Laser Ion Interaction

The absorption and re-emission of laser photons change the momentum of the ions, as discussed in Sect. 3.2. For the implementation in the PIC tracking code two different models for the cw laser and one for the pulsed laser excitation are presented. The models assume an equally distributed laser intensity in the transverse plain within the laser interaction section.

4.2.1 Statistical cw Laser Model

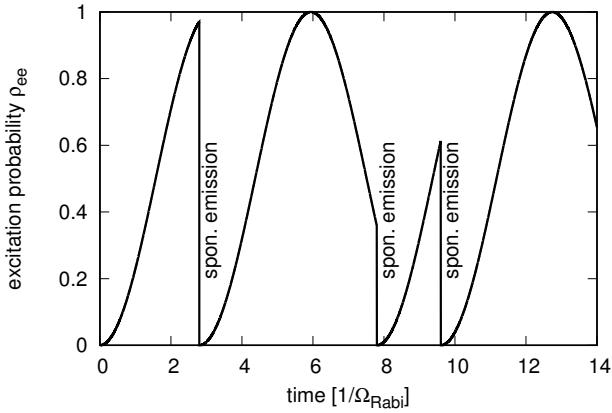


Figure 4.1: Example of excitation probability of a single ion. The excitation probability oscillates and is interrupted by spontaneous emissions, whose probability of occurrence is equal to the excitation probability.

The laser ion interaction consists of three effects given by the stimulated emission, the spontaneous emission and the absorption of a photon. Neglecting the spontaneous emissions, the excitation probability oscillates for each ion with the Rabi frequency

$$\rho_{ee}(t, \delta) = \frac{\Omega_{Rabi}^2}{\Omega_{Rabi}^2(\delta)} \cdot \sin^2\left(\frac{\Omega'_{Rabi}(\delta) \cdot t}{2}\right), \quad (4.14)$$

where the momentum dependent Rabi frequency is given by

$$\Omega'_{Rabi}(\delta) = \sqrt{\Omega_{Rabi}^2 + \xi^2 \cdot (\delta - \delta_{LPoS})^2} \quad (4.15)$$

$$\Omega_{Rabi} = \sqrt{I(t)/2I_S} \cdot 1/\tau_{se}. \quad (4.16)$$

The process is discussed in more detail in Ref. [37] and the symbols are explained in Sect. 3.2. The probability of a spontaneous emission is proportional to the excitation probability. If a spontaneous emission takes place, the ion receives the recoil of the emitted photon, the excitation probability drops immediately down to $\rho_{ee} = 0$ and continues with oscillations (see example in fig. 4.1). The mathematical description of the Rabi oscillation including the spontaneous emission would need to include the basis functions of all possible spontaneous emissions but the problem can be solved by using the Monte Carlo method (see Ref. [54]). However the simulation of laser cooling does not require the exact description of the whole laser ion interaction, because only the momentum transfer of a spontaneous emission is relevant for the cooling process. Therefore the model has to reproduce the number of spontaneous emissions in a certain time interval and the momentum change for each spontaneous emission. In order to reduce the computational effort and still use a realistic description of the interaction, the interaction region is divided into slices ($n_{slices} \geq n_{scat}^{turn}(\delta_{LPoS})$). The probability of a spontaneous emission in one slice is given by

$$\rho_{slice}(\delta) = \int_t^{t+\Delta t} \rho_{ee}(t', \delta) dt'. \quad (4.17)$$

For a saturated transition during the cw laser excitation Eq. 4.17 simplifies to

$$\rho_{slice}(\delta) = \frac{n_{scat}^{turn}(\delta)}{n_{slices}}. \quad (4.18)$$

The probability is equal for each slice in the interaction region. During numerical simulations, a random number is compared to the excitation probability for each slice. If the random number is smaller, the momentum change of a spontaneous emission is applied to the ion (see Eq. 3.9). The number of spontaneous emissions for different n_{slices} is shown in a histogram in fig. 4.2 for $n_{scat}^{turn}(\delta_{LPoS}) = 4.7$. The results indicate that choosing only 5 slices the statistical occurrence of spontaneous emissions is not well described, whereas for $n_{slices} = 10 \approx 2 \cdot n_{scat}^{turn}$ the distribution has already converged sufficiently. The impact of different number of slices on particle dynamics during the cooling process is discussed in Sect. 4.2.4.

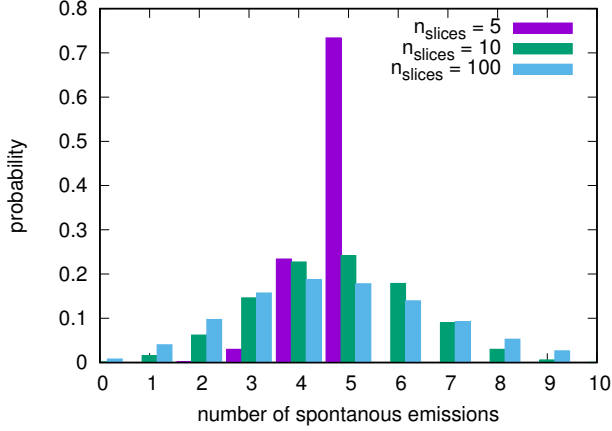


Figure 4.2: Histogram of the probability of different numbers of spontaneous emissions during the interaction section for $n_{scat}^{turn}(\delta_{LPos}) = 4.7$. For $n_{slices} = 5 \approx n_{scat}^{turn}$ the statistical distribution is not well described whereas for $n_{slices} = 10$ the distribution has already converged sufficiently.

4.2.2 Mean cw Laser Model

A simplified implementation of the photon ion interaction is given by the mean force of the interaction. For this model the ions experience a momentum change calculated by

$$\Delta p_{turn}^{LF} = \langle \Delta p^{LF} \rangle \cdot n_{scat}^{turn}(\delta) \quad (4.19)$$

$$= \langle \Delta p^{LF} \rangle \cdot \frac{L^{interact}}{\gamma \beta c_0} \cdot \frac{1}{2\tau_{se}^{PF}} \frac{S}{1 + S + (2\xi(\delta - \delta_{LPos}) \cdot \tau_{se}^{PF})^2}, \quad (4.20)$$

which is applied once per revolution in the accelerator. The model neglects the statistical component and the quantization of the laser ion interaction. The impact of this simplification on the simulation results for the laser cooling process is discussed in Sect. 4.2.4.

4.2.3 Pulsed Laser Model

The probability of a scattering event in the interaction region for a pulsed laser excitation, which is calculated by Eq. 3.31, is always below or equal to 1. The transferred momentum of the pulsed laser excitation is calculated as described in Sect. 4.2.1 for the cw laser excitation. But the number of slices for one revolution in the accelerator

is set to one. The probability of a spontaneous emission in the single slice is calculated by Eq. 3.31. The separation of the interaction region into several slices is not necessary, because spontaneous emissions can be neglected during the excitation.

4.2.4 Impact on Cooling Process

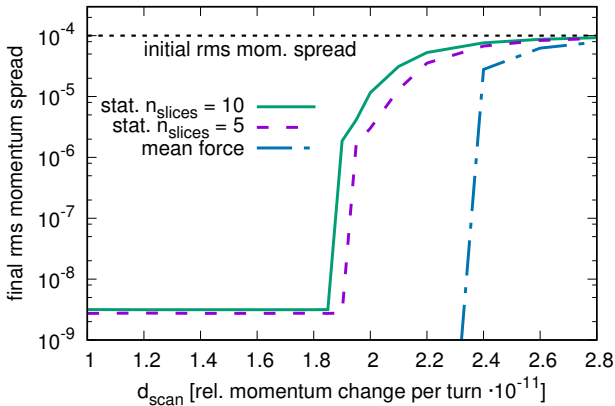


Figure 4.3: Final rms momentum spread for different scan speeds of the laser force. The implementation of the mean laser force is compared to the statistical implementation with two different amounts of slices. The results of the two different simulations with the statistical implementation are very similar, whereas the implementation of the mean laser force shows some deviations.

This section discusses the impact on the laser cooling process of the different cw laser force models. The process is discussed in detail in Sect. 5.1. The scanned cw laser cooling scheme of titanium ions in the SIS100 is exemplary investigated. Figure 4.3 shows the final rms momentum spread for different models of the laser force. The results for the statistical implementation (see Sect. 4.2.1) for $n_{slices} = 5$ and $n_{slices} = 10$ are compared. Despite the distribution of the statistical occurrence of spontaneous emissions not being equal for both cases (see fig. 4.2), the results of the cooling process are very similar. The maximum scan speed of the laser resonance differs only by $\approx 4\%$. During the presented cooling process each ion spontaneously emits approximately $\sigma_{\delta 0} / \Delta \delta^{LF} \approx 10^5$ photons. Due to the large number of spontaneous emission, the details of a single spontaneous emission are not important for the particle dynamics during the

cooling process as long as the mean momentum change and the strength of diffusive heating are correctly reproduced.

Beside the statistical model, figure 4.3 shows the final rms momentum spread for the implementation of the mean laser force (see Sect. 4.2.2). The mean laser force model does not include the laser induced diffusion. The lack of diffusive heating enables to cool below the Doppler limit, which disagrees with the theory of Doppler laser cooling. Secondly the maximum scan speed is $\approx 20\%$ higher due to the lack of the statistical process. However the evolution of the phase space distribution of a successful cooling process is very similar for both simulation models, especially for simulations including other heating effects, the differences of the laser force models become negligible. Therefore the simplified mean laser force model is suitable for analytic descriptions and preliminary simulations.



5 Cooling Process

The procedure of laser cooling in a circular accelerator differs from the conventional cooling process in a particle trap. As described in Sect. 3.2 the strong Doppler shift of the laser light in the frame of a relativistic ion beam prevents the setup with two counter-propagating laser beams. Only the laser beam which is counter-propagating to the ion beam, satisfies the resonant condition (see Eq. 3.5). Furthermore the initial momentum spread of the ion ensemble in an accelerator is typically significantly higher compared to the momentum spread in a particle trap. The width of the cooling force of a cw laser system is approximately $\Delta_{fwhm} \approx 5 \cdot 10^{-8}$ in units of relative momentum (discussed in more detail in Sect. 7.1), while the ions have typically an initial rms momentum spread in the range of $\sigma_{\delta_0} \approx 10^{-5} - 10^{-3}$. As a consequence only a small fraction of the ion ensemble interacts with the laser light.

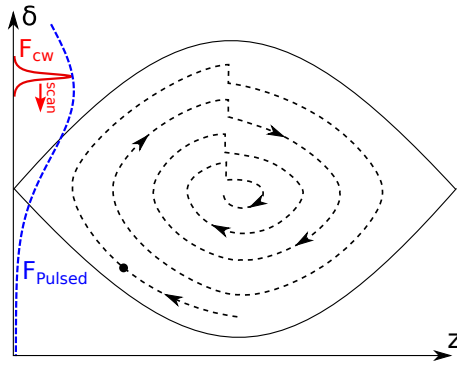


Figure 5.1: Sketch of the ion trajectory in longitudinal phase space during the cooling process in a rf bucket. The laser force of a cw laser and the pulsed laser are indicated by the red and the dashed blue curve. The cw laser force is scanned to damp continuously the synchrotron oscillations of all ions whereas the pulsed laser force interacts with all ions simultaneously.

The cooling processes that overcome both challenges, are discussed in the following. The inter-particle interactions are neglected in this chapter. The expected cooling times are given for the cooling process with a cw laser system and a pulsed laser system. The simulation results are given exemplary for the cooling process of lithium-like titanium ions Ti^{19+} in the SIS100 with an initial rms momentum spread of $\sigma_{\delta_0} = 10^{-4}$. The

relevant accelerator properties are given by the length of the accelerator $L_{acc} = 1080 m$, the length of the laser ion interaction $L_{interact} = 26 m$, the harmonic number $h = 8$ of the rf system and the gamma transition of $\gamma_t = 15$. The atomic transition is assumed to be saturated ($S = 1$) for the cw laser excitation and the excitation probability to be $\rho_{scat}(\delta_{LPos}) = 1$ for the pulsed laser excitation.

5.1 Continuous Wave Laser

The cooling process of a particle ensemble requires a stable point where the sum of all forces cancels. Due to the lack of two counter-propagating laser beams the decelerating laser force is counteracted by the force, induced by the rf bucket (see Ref. [55]). The synchrotron motion in the sinusoidal rf bucket leads to a repetitive exchange of ions with a higher momentum and ions with a lower momentum with respect to the reference particle as illustrated in fig. 2.2. Due to the exchange, the laser acts on ions with a positive as well as a negative momentum deviation. The significant difference of this technique compared to two counter-propagating laser beams is that the ions do not continuously interact with the cooling force. The ions only experience a cooling force on a small fraction of the synchrotron motion and oscillate in the bucket without a cooling force for many revolutions in the circular accelerator.

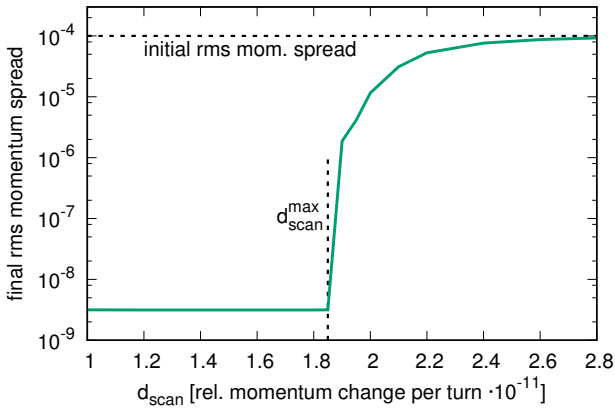


Figure 5.2: Final rms momentum spread for different scan speeds of the laser force in units of relative momentum per turn for titanium ions in the SIS100.

In order to extend the interaction range of the narrow cw laser force, the laser wavelength is scanned in time. As a result, the position of the laser resonance in phase space δ_{LPos} changes as illustrated in fig. 5.1. Starting at the momentum deviation of the particle with the highest oscillation amplitude $\hat{\delta}$ the laser force is scanned continuously to

the center of the bucket. After each ion photon interaction the oscillation amplitude of the ion is damped. The ions follow the scan of the laser resonance to the center of the bucket and the rms momentum spread of the ensemble shrinks. The required time for the laser cooling process is calculated by

$$T_{cool} = T_{rev} \cdot \frac{\hat{\delta}}{d_{scan}} \quad (5.1)$$

and is proportional to the momentum deviation of the particle with the highest oscillation amplitude $\hat{\delta}$ and inversely proportional to the scan speed of the resonance d_{scan} . The unit of the scan speed is given by the change in relative momentum of the laser resonance per turn. Consequently, the cooling time reduces for increasing scan speeds of the laser resonance in phase space.

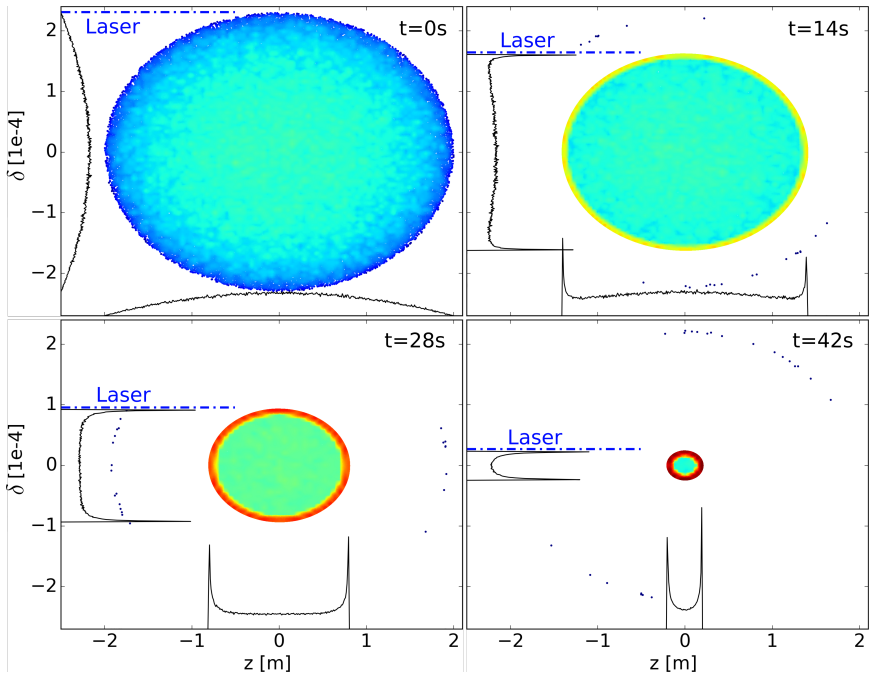


Figure 5.3: Evolution of the phase space distribution for a successful cooling process ($d_{scan} < d_{scan}^{max}$). All ions are continuously pushed to the center of the bucket. The ions form a dense ring in phase space that creates peaks in the longitudinal line density.

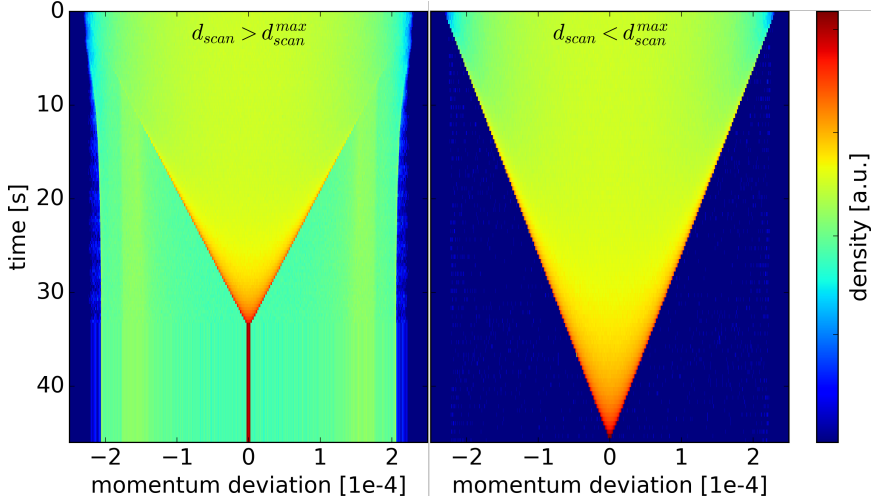


Figure 5.4: Evolution of the momentum distribution over time (left) for an unsuccessful cooling process ($d_{scan} > d_{scan}^{max}$) and (right) for a successful cooling process ($d_{scan} < d_{scan}^{max}$). For the unsuccessful cooling process some ions are lost behind the laser force and do no longer take part in the cooling process.

Beside the required cooling time, the speed of the laser resonance scan strongly influences the success and efficiency of the cooling process. The final rms momentum spread after the laser scan for different scan speeds is shown in fig. 5.2. The results are calculated for an initial bunch length of $4m$ in order to produce a rapid synchrotron motion and stay in the linear region of the bucket. The results in fig. 5.2 indicate that below a certain speed of the laser scan (marked as d_{scan}^{max}) the cooling process is successful, whereas above this scan speed the rms momentum spread of the ion distribution stays close to the initial value.

The phase space distribution during a successful cooling process ($d_{scan} < d_{scan}^{max}$) is shown in fig. 5.3. The narrow cw laser force creates a dense ring of ions in phase space and continuously pushes the ions to the bucket center. Due to the synchrotron motion, the bunch length shrinks by the same factor as the rms momentum spread. Figure 5.4 compares the evolution of the momentum distribution for a successful ($d_{scan} < d_{scan}^{max}$) and an unsuccessful ($d_{scan} > d_{scan}^{max}$) cooling process. The cooling process is successful if all ions stay always in front of the laser force and move with repetitive steps to the center of the bucket. For the unsuccessful cooling process the laser force moves faster to the center of the bucket than the ions. Consequently, some ions are left behind and do not interact with the laser light for the rest of the cooling process. A snapshot of the

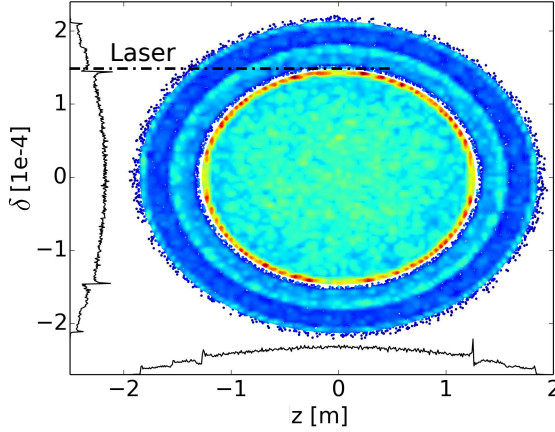


Figure 5.5: Snapshot of the phase space distribution for an unsuccessful cooling process ($d_{scan} > d_{scan}^{max}$). Ions are left behind the laser force and are no longer affected by the laser force. Only a small fraction of the ions is cooled.

phase space distribution for an unsuccessful cooling process is shown in fig. 5.5. Most of the ions preserve the initial distribution and only a small fraction of the ions are laser cooled.

The maximum laser scan speed d_{scan}^{max} is equal to the mean momentum change of the ions per turn. This quantity is calculated by averaging the laser force over the synchrotron motion.

$$d_{scan}^{max} \approx \langle \Delta \delta_{turn}^{LF} \rangle_{syn} \quad (5.2)$$

The mean momentum change is calculated for the ions with the oscillation amplitude equal to the resonant momentum of the laser force ($\hat{\delta} = \delta_{LPos}$). In the linear region of the rf bucket the average momentum change by the laser interaction $\Delta \delta_{turn}^{LF}(\delta)$ is calculated by

$$\langle \Delta \delta_{turn}^{LF} \rangle_{syn} = \frac{1}{2\pi} \int_0^{2\pi} \Delta \delta_{turn}^{LF}(\delta_{LPos} \cdot \cos(\phi)) \cdot \cos(\phi) d\phi. \quad (5.3)$$

The calculation assumes a circular motion in the rf bucket and is only valid for a small perturbation by the laser force. The strength of the perturbation is expressed by the momentum change of the laser force (see Eq. 3.14) divided by the momentum change

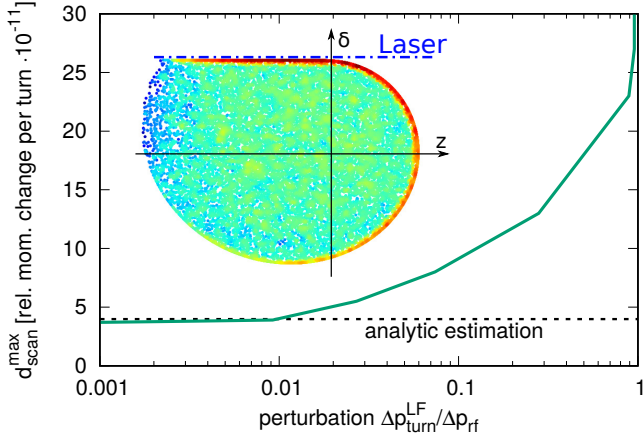


Figure 5.6: Maximum scan speed of the laser resonance in units of relative momentum per turn for different strength of the perturbation of the synchrotron motion by the laser. The perturbation is defined by the ratio of the momentum change per turn by the laser force and by the rf force. The snapshot of the phase space density for a strong perturbation $\Delta p_{turn}^{LF}/\Delta p_{rf} \approx 1$ indicates, that the ions stay in resonance with the laser light for a longer time. The prolonged laser ion interaction increases the maximum scan speed respectively reduces the required cooling time.

of the rf bucket $\Delta p_{turn}^{LF}/\Delta p_{rf}$. Figure 5.6 shows the maximum scan speed for different strengths of the perturbation. The ratio of the laser and rf force is changed by varying the strength of the rf potential respectively the bunch length. For the simulation the laser force is multiplied by two in order to cover the whole range. If $\Delta p_{turn}^{LF}/\Delta p_{rf} \ll 1$ (small perturbation) the simulation results converge towards the analytic estimation (see Eq. 5.3) while for $\Delta p_{turn}^{LF}/\Delta p_{rf} \approx 1$ (strong perturbation) the maximum laser scan speed increases. The strong perturbation of the circular motion in the bucket, like illustrated in the phase space plot in fig. 5.6, keeps the ions in resonance with the laser light for a longer time and increases the maximum scan of the laser resonance per turn. A faster scan of the laser resonance reduces the required cooling time (see Eq. 5.1). Consequently, a slow motion of the ions in the bucket and therefore a strong perturbation of the laser force is beneficial for a rapid cooling process.

An alternative cooling scheme exists for a laser force stronger than the maximum rf force $\Delta p_{turn}^{LF}/\Delta p_{rf} > 1$. If this condition is fulfilled the laser resonance can directly be set close to the center of the bucket. The particles are not able to pass the laser force because the laser is stronger than the rf force. As a result, the synchrotron motion of the ions is interrupted and the particles stay close to the laser force as illustrated in

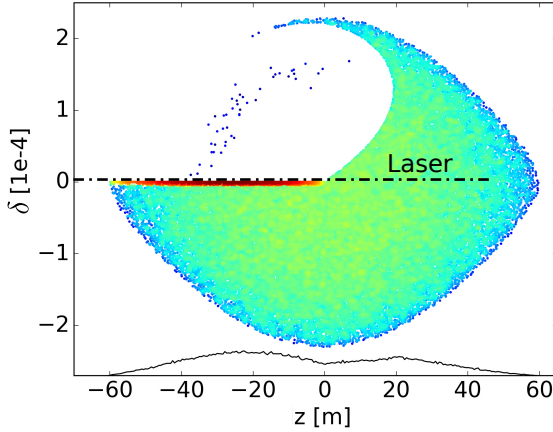


Figure 5.7: Snapshot of the phase space density during an alternative cooling scheme for a strong laser force $\Delta p_{turn}^{LF}/\Delta p_{rf} > 1$. The laser resonance is set close to the center of the bucket and the ions rotate into the laser force. At the position of the laser force the synchrotron motion of the ions is stopped.

fig. 5.7. The ions which are not in resonance with the laser, perform the synchrotron motion until they are captured by the laser force. The cooling time is reduced to one synchrotron period

$$T_{cool}^{fixedCW} = T_{rev} \cdot \frac{1}{Q_s}, \quad (5.4)$$

where Q_s is the synchrotron tune. The fixed laser scheme is much faster compared to the scan of the laser resonance, but it is only available for a strong laser force and a slow motion of the ions in the bucket. If the condition for this cooling scheme is fulfilled ($\Delta p_{turn}^{LF}/\Delta p_{rf} > 1$), a further reduction of the synchrotron tune increases the cooling time.

In contrast to the scanned cw laser scheme, the fixed cw laser scheme does not simultaneously reduce the spatial and momentum spread. At the final state the ions accumulate at the accelerating half of the bucket, as shown by the high ion density in fig. 5.7. Consequently, the bunch length is only reduced by a factor of two during the cooling process and the distribution is not matched to the rf bucket without the laser force.

5.2 Pulsed Laser

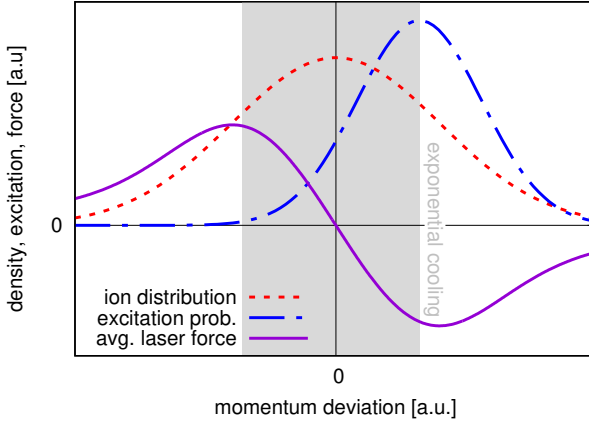


Figure 5.8: Illustration of the pulsed laser force. The pulsed laser affects all ions with a positive momentum deviation. By averaging over the synchrotron motion (purple line) the deceleration force results in a symmetric friction force with the stable point in the center of the bucket. In the linear region of the cooling force, the rms momentum spread of a particle distribution decreases exponentially.

The procedure and particle dynamics during the cooling process with a pulsed laser system differ from the cooling process with a cw laser system. In contrast to the narrow band cw laser force the width of the pulsed laser force can be adjusted the way that the laser affects all ions in phase space as shown in fig. 5.1. Therefore no scan of the laser frequency is needed during the cooling process. As illustrated in fig. 5.8 the laser force averaged over the synchrotron motion results in a symmetric friction force with a stable point in the center of the bucket. In the central region the mean laser force is linear and the rms momentum spread of the particles decreases exponentially. If all ions are within the linear region the cooling rate is calculated by

$$\tau_{pulse\ cool}^{-1} = \frac{1}{T_{rev}} \frac{\partial \langle \Delta \delta_{turn}^{pulsed} \rangle_{syn}}{\partial \delta} \quad (5.5)$$

$$\approx -\frac{1}{T_{rev}} \cdot \langle \Delta \delta^{LF} \rangle \cdot \rho_{scat}(0) \frac{\delta_{LPos}}{2\sigma_{\delta Laser}^2} \quad (5.6)$$

where $\langle \Delta \delta_{turn}^{pulsed} \rangle_{syn}$ is the momentum kick of the pulsed laser averaged over the synchrotron motion. The quantity is sketched in fig. 5.8 and is calculated equivalent to the cw laser force in Eq. 5.3. The evolution of the rms momentum spread over time during the cooling process is shown in fig. 5.9. The results are given for the cooling process of titanium ions in the SIS100. The excitation probability is set to $\rho_{excit}(\delta_{LPos}) = 1$. At the beginning some ions are located outside of the linear region of the averaged laser force where the cooling rate is lower. After all ions are within the linear region the exponential decrease, calculated by Eq. 5.5, represents the simulation properly. Due to the linear cooling force the distribution stays close to a Gaussian shape during the whole cooling process. The required cooling time is calculated by

$$T_{cool} = \tau_{pulse\ cool} \cdot \ln\left(\frac{\sigma_{\delta_0}}{\sigma_{\delta_f}}\right), \quad (5.7)$$

where σ_{δ_0} and σ_{δ_f} are the initial and final rms momentum spread of the bunch.

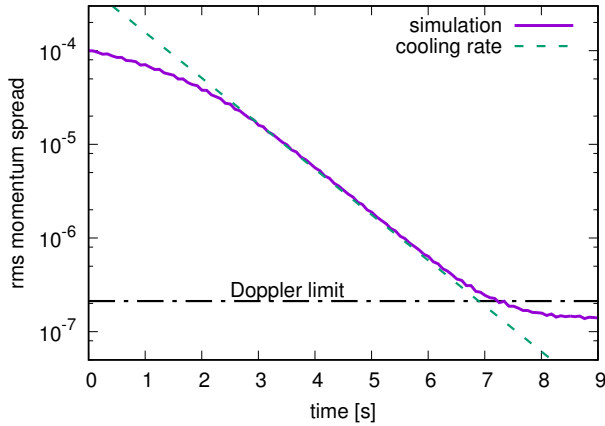


Figure 5.9: Cooling process of titanium ions in the SIS100 with a single pulsed laser system. The dashed lines show the analytically calculated cooling rate (see Eq. 5.5) and the Doppler limit (see Eq. 5.11).

The cooling is counteracted by the diffusive heating of the ion-photon interaction. The laser heating originates in the finite steps of the cooling force and the random direction of the spontaneous emissions. The average momentum change of a scattering

event is $\langle \Delta \delta^{LF} \rangle$ and the average time between two scattering events is $T_{rev}/\rho_{scat}(0)$. The diffusion coefficient results in

$$D_L = \frac{\langle \Delta \delta^{LF} \rangle^2 \cdot \rho_{scat}(0)}{T_{rev}}, \quad (5.8)$$

and leads to a heating rate of (see Eq. 4.12)

$$\tau_{Lheat}^{-1} = \frac{D_L}{\sigma_{\delta}^2}. \quad (5.9)$$

The lowest attainable rms momentum spread is given by the equilibrium state of the diffusive heating and the laser cooling rate

$$\tau_{pulse\ cool}^{-1} + \tau_{Lheat}^{-1} = 0. \quad (5.10)$$

Rearranging the equation the equilibrium rms momentum spread is determined by

$$\sigma_{\delta\ equ}^{pulsed} = \sqrt{\frac{\langle \Delta \delta^{LF} \rangle \cdot \sigma_{\delta Laser}^2}{\delta_{LPoS}}}, \quad (5.11)$$

and is referred to the Doppler limit (see Ref. [37]). Compared to a cw laser system, the Doppler limit of a pulsed laser system can be adjusted by the width and the position of the laser force. However, the Doppler limit of a pulsed laser system is always above and typically much higher than the limit of the cw laser system.

The width and position of the pulsed laser force in phase space influence the performance of the laser cooling process. Figure 5.10 shows the required cooling time of titanium ions in the SIS100 for different configurations of the pulsed laser. The cooling time for an initial rms momentum spread of $\sigma_{\delta 0} = 10^{-4}$ to the final rms momentum spread of $\sigma_{\delta f} = 10^{-6}$ is simulated. The most efficient cooling process, with a cooling time of $T_{cool} \approx 5$ s is achieved by choosing $\delta_{LPoS} \approx 8.3 \cdot 10^{-5}$ and $\sigma_{\delta Laser} \approx 6.3 \cdot 10^{-5}$ in units of relative momentum. However, the configurations within $\approx \pm 20\%$ of the ideal values do not show a significant increase of the cooling time which implies that an adjustment of position and width of the pulsed laser force within this range of precision is sufficient. Beside the required cooling time, the configuration of the pulsed laser force influences the Doppler limit, as described by Eq. 5.11. The lowest attainable rms momentum spread for different configurations are shown in fig. 5.11. Within the region of short cooling times the Doppler limit varies marginally. However, if lowest possible rms momentum spreads is the goal of a cooling process the width of pulsed laser force $\sigma_{\delta Laser}$ can be reduced with the drawback of an increase of the required cooling time.

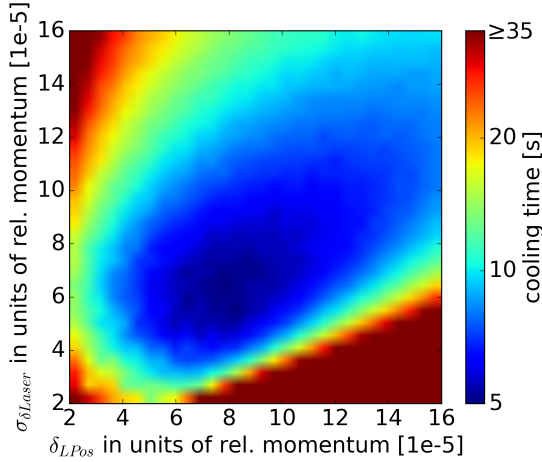


Figure 5.10: Required cooling time for the cooling process with a pulsed laser system for titanium ions in the SIS100. The width and position of the pulsed laser force is varied. The cooling time for the reduction of the rms momentum spread from $\sigma_{\delta 0} = 10^{-4}$ to $\sigma_{\delta f} = 10^{-6}$ is determined by numerical tracking simulations.

The optimized configuration for a rms momentum spread reduction of two orders of magnitude is generalized for arbitrary initial rms momentum spreads to

$$\delta_{LPos} \approx 0.83 \cdot \sigma_{\delta} \quad (5.12)$$

$$\sigma_{\delta Laser} \approx 0.63 \cdot \sigma_{\delta}. \quad (5.13)$$

This configuration is also used in the cooling process depicted in fig. 5.9 and the illustration in fig. 5.8.

5.3 Combined Laser Systems

The presented cooling scheme with a pulsed laser force does not satisfy optimal conditions for a cooling process. As shown in fig. 5.10 and fig. 5.11 the choice of the width and position of the pulsed laser force is a compromise between a short cooling time and a strong final cooling rate in order to reach low rms momentum spreads.

A high derivative of the averaged cooling force at the center of the bucket leads to a high final cooling rate. While a broad laser spectrum is required in order to cool the entire ion distribution. Therefore the ideal broadband laser force provides a sharp edge

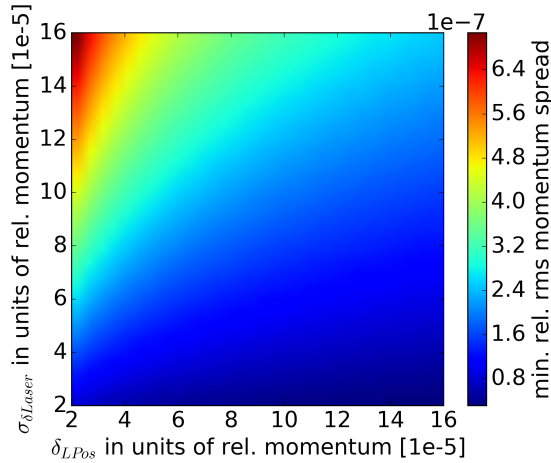


Figure 5.11: Equilibrium rms momentum spread for the cooling process with a pulsed laser system for titanium ions in the SIS100. The values are calculated by Eq. 5.11.

at the center of the bucket and is as strong as possible for all ions with $\delta > 0$. A single pulsed laser force does not fulfill the requirements but a combination of different laser pulses get closer to the ideal cooling force.

Figure 5.12 shows an example of the combination of two different pulsed laser systems and the force averaged over the synchrotron motion. The laser pulse with a high spectral width covers the ions with a high relative momentum deviation, while the interaction with ions close to the center of the bucket should be small. The second laser with a significantly lower spectral width creates a high derivative of the averaged laser force in the center of the bucket. The evolution of the rms momentum spread is compared to the cooling process with a single pulsed laser in fig. 5.13. The second pulsed laser system reduces the required cooling time and the final rms momentum spread by approximately a factor of two. The efficiency can be further increased by combining more than two different laser pulses and further converge towards the previously described ideal laser force. The drawback of the combination of different laser pulses is the creation of a non-linear cooling force and the generation of non-Gaussian beam profiles. The sharp edge in the bucket center quickly accumulates ions in the center while most of the ions are still in the outer region of the bucket. As a result, the distribution is a superposition of two Gaussian distributions during the cooling process.

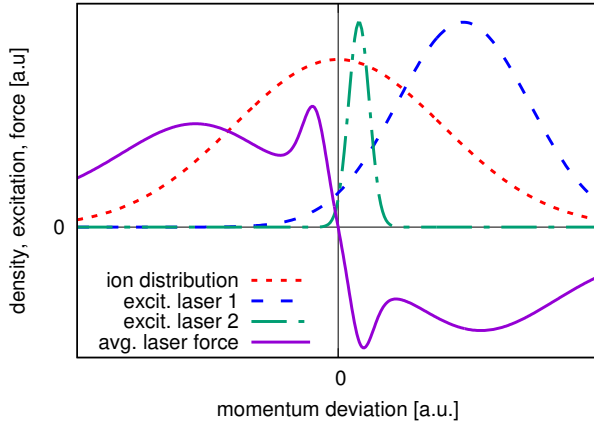


Figure 5.12: Illustration of the laser cooling force for combined pulsed laser systems. The laser force of the two laser systems averaged over the synchrotron motion offers a broad capture range and a high gradient at the center of the bucket.

5.4 Alternative Bucket Shapes

The shape of the bucket area in phase space is formed by the signal applied to the rf cavities. Beside a sinusoidal excitation which is described in Sect. 2.1, alternative configurations exist. The planned rf system in the SIS100 is able to generate barrier buckets and dual rf buckets in addition to the sinusoidal bucket shape. Both types create a section with a small rf voltage in the center of the bucket in order to get a constant ion density as illustrated in fig. 5.14. In the dual rf system, the second harmonic of the initial rf signal is applied to the particles with opposite phase. This leads to an reduction of the applied voltage in the center of the bucket as described in more detail in e.g. Ref. [56]. For the barrier bucket the positive and negative half of the sinusoidal wave are separated by a time delay Δt_{BB} that creates an acceleration free section in the bucket center with length $L_{BB} = \beta c_0 \Delta t_{BB}$ (see Ref. [57]). The applied voltage and the generated bucket shape is illustrated in fig. 5.14. The ions travel with constant momentum in the acceleration free area and experience a reflection at the barriers created by the two half waves. First experimental studies of laser cooling in a barrier bucket were conducted at TSR as described in Ref. [58].

For the Doppler laser cooling process the constant momentum in the acceleration free area in a barrier bucket seems to be beneficial. Following Eq. 5.2 the maximum scan speed of the laser resonance is equal to the average momentum change of the ion laser interaction. As illustrated in fig. 5.14, the ions are in resonance with the laser light for

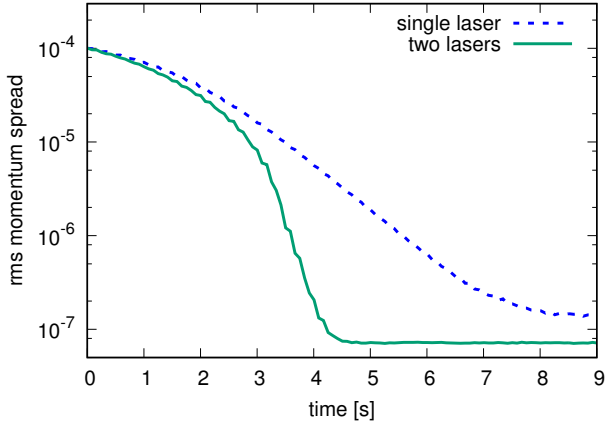


Figure 5.13: Evolution of the rms momentum spread over time for the single pulsed laser system and the combination of two laser systems. The second laser force creates a high gradient in the center of the bucket and reduces the required cooling time and equilibrium momentum spread by a factor of two.

a prolonged time. Assuming an instantaneous reflection at the two barriers (length of the barrier bucket L_{BB} is much larger compared to the distance the ions penetrate into the half wave of the rf signal), the ions are in resonance with the laser light for 50% of the time and the averaged momentum change (calculated equivalent to Eq. 5.3) is

$$\langle \Delta \delta_{turn}^{LF} \rangle_{syn} \approx \frac{1}{2} \Delta \delta_{turn}^{LF}. \quad (5.14)$$

This would lead to an extremely fast scan of the laser resonance and a very short cooling time. However, the condition of the maximum scan speed (see Eq. 5.2) assumes a small perturbation of the synchrotron motion in the bucket. Consequently, the change of the oscillation amplitude during one synchrotron motion has to be small compared to the width of the laser force. Following Eq. 5.2 the same limit holds for the shift of the laser resonance during one synchrotron period:

$$\frac{d_{scan}^{max}}{Q_s} \lesssim \Delta_{fwhm} \quad (5.15)$$

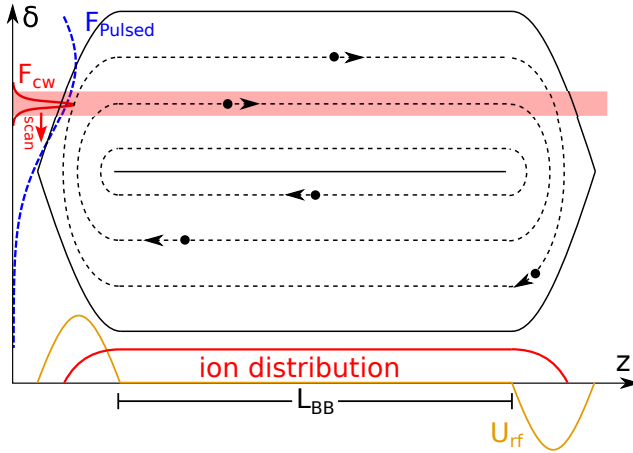


Figure 5.14: Sketch of the phase space area in a barrier bucket. The barrier bucket is created by two half waves of the rf voltage separated by a length L_{BB} . In the acceleration free area the ions have constant momentum and the initial ion distribution has a constant density.

If this condition is not fulfilled, the scan of the laser force is too fast to catch the ions after each synchrotron motion. The laser force forms a spiral in phase space and the rms momentum spread remains nearly constant.

In the barrier bucket the synchrotron tune differs from the conventional tune in the sinusoidal bucket. Assuming an instantaneous reflection at the two barriers, the synchrotron tune of the ions is equal to

$$Q_S^{BB} \approx \frac{v_z T_{rev}}{2L_{BB}} = \frac{-\eta L_{acc} \delta}{2L_{BB}}. \quad (5.16)$$

In contrast to a conventional sinusoidal bucket the synchrotron tune in a barrier bucket depends strongly on the momentum deviation of each ion. Ions with a high momentum deviation perform fast oscillations in the bucket whereas ions which are close to the reference ion, are very slow and the condition in Eq. 5.15 requires very slow scan speed of the laser resonance.

Figure 5.15 shows the evolution of the momentum distribution for the cooling process in a barrier bucket with a constant scan speed. At the beginning the ions perform fast oscillations in the barrier bucket and are successfully cooled down. When the synchrotron motion is too slow to fulfill the condition in Eq. 5.15, ions circulate behind the laser resonance. The ions do not interact with the laser light any more and the distribution stays unchanged for the rest of the laser resonance scan. A change of the

barrier bucket shape or a reduction of the scan speed is required in order to reach lower rms momentum spreads.

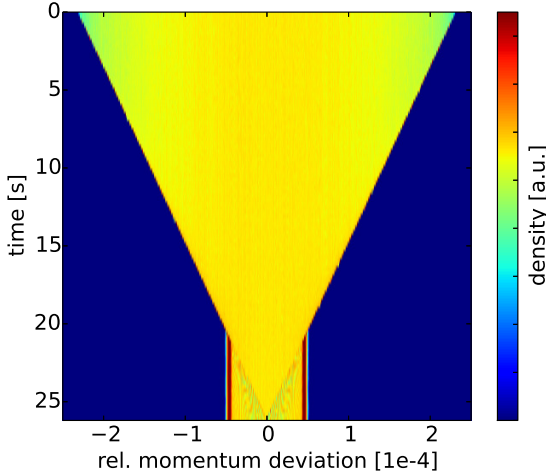


Figure 5.15: Evolution of the momentum distribution during the cooling process in a barrier bucket. The laser force cools the ion ensemble until the synchrotron motion is too slow to fulfill the condition Eq. 5.15. The ions get lost behind the cooling force.

The comparison of the final rms momentum spread for the conventional sinusoidal bucket and the barrier bucket with different length L_{BB} is shown in fig. 5.16. The cooling process is simulated for titanium ions in the SIS100. For short barrier buckets and high rms momentum spreads the laser scan interacts more efficiently with the ions compared to the cooling scheme in a sinusoidal bucket. But at lower rms momentum spreads the slow synchrotron motion in the barrier bucket require very slow scan speeds. The advantage of the prolonged interaction time is predominated by the disadvantage of the slow synchrotron motion for low rms momentum spreads. For a cooling process with a final rms momentum spread below $\sigma_\delta < 10^{-6}$ laser cooling in a sinusoidal bucket shows the best results.

A second major difference of the cooling process in a barrier bucket and a sinusoidal bucket exists. The spatial bunch length does not change during the cooling process in a barrier bucket while in a sinusoidal bucket the bunch length shrinks equally to the rms momentum spread (see fig. 5.3). However, the spatial ion distribution changes for low rms momentum spreads in a barrier bucket. The accumulation of the ions at low rms momentum spreads requires a stable point where the sum of the applied forces

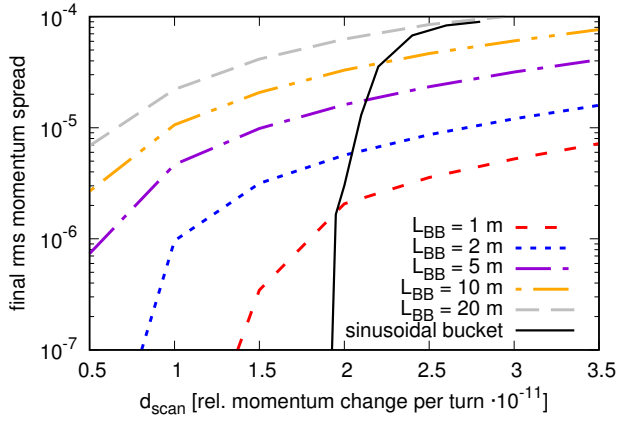


Figure 5.16: Rms momentum spread of the ion ensemble after the cw laser scan in the barrier bucket. The final rms momentum spread is given for different scan speeds d_{scan} and different length of the barrier bucket L_{BB} . For longer barrier buckets the scan speed has to be reduced. For a successful cooling process the scan speed reaches the highest value for the case of a conventional bucket (curve equal to fig. 5.2).

vanishes. The decelerating laser force is counteracted by the accelerating half wave of the barrier bucket. After reaching a low rms momentum spread ($\sigma_\delta \lesssim \Delta_{fwhm}$), the ions accumulate at the accelerating half wave. This leads to an abrupt rise of the ion density and a final bunch length similar to the final state in a sinusoidal bucket.



6 Intensity Effects

This chapter investigates the interplay of the cooling force of the ion-photon interaction and the ion intensity dependent heating effects. While many studies deal with the influence of intensity effects on the laser cooled ion bunch in the strongly coupled regime [59, 60, 61], the impact of intensity effects on relativistic ion beams during the scan of the laser force is nearly unknown. The study concentrates on effects which limit or prevent the successful cooling process of a relativistic ion beam. The simulation results are exemplary given for the cooling process of lithium-like titanium ions in the SIS100 as studied without intensity effects in Chapter 5.

6.1 Intra Beam Scattering

Intra beam scattering is a dominant intensity effect at low rms momentum spreads. IBS directly counteracts the cooling process and heats up the ion ensemble. The effect is described in Sect. 2.3 and the implementation in the simulation tool is explained in Sect. 4.1.

6.1.1 Pulsed Laser

The phase space distribution stays close to a Gaussian shape during the whole cooling process with a pulsed laser system as described in Sect. 5.2. The cooling and heating of a Gaussian distribution are described by rms rate equations, which express the change of the rms momentum spread in time. The final state of the cooling process is reached when the IBS heating rate (see Eq. 2.33) and the laser cooling rate (see Eq. 5.5) cancel each other. The equilibrium state is given by

$$\tau_{IBS}^{-1} + \tau_{pulse\ cool}^{-1} = 0. \quad (6.1)$$

The equilibrium rms momentum spread is assumed to be well above the Doppler limit (see Eq. 5.11). Consequently the laser heating is expected to be much smaller than the IBS heating ($\tau_{Lheat}^{-1} \ll \tau_{IBS}^{-1}$) and is neglected in the following calculations.

For a given configuration of the pulsed laser system the laser cooling rate is independent of beam parameters and constant in time. The IBS heating rate is calculated by Eq. 4.12 and changes during the cooling process. The heating rate is proportional to the longitudinal line density and inversely proportional to the rms momentum spread squared. Assuming a fast synchrotron motion ($\tau_{pulse\ cool}^{-1} \ll Q_s/T_{rev}$) and the bunch to be in the linear region of the sinusoidal bucket, the relative reduction of the bunch length

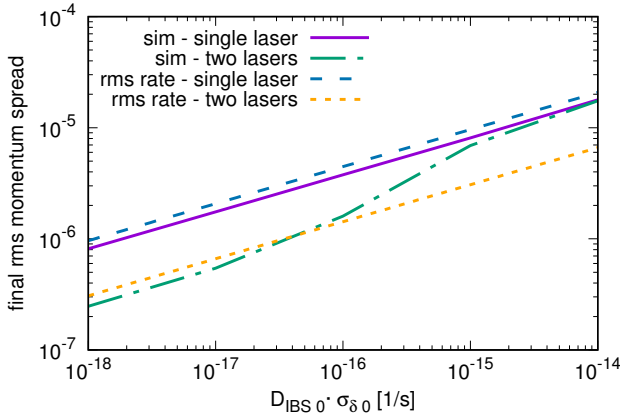


Figure 6.1: Equilibrium rms momentum spread for IBS heating and pulsed laser cooling. Simulation results are compared to analytic results (Eq. 6.3) and show good agreement. The rms momentum spread decreases by adding a second pulsed laser system.

and rms momentum spread are equal as illustrated in fig. 5.1. The proportionality is used to express the IBS growth rate by

$$\tau_{IBS}^{-1} = \frac{D_{IBS}}{\sigma_{\delta}^2} = \frac{D_{IBS0}}{\sigma_{\delta}^2} \cdot \frac{\sigma_{z0}}{\sigma_z} = \frac{D_{IBS0}}{\sigma_{\delta}^2} \cdot \frac{\sigma_{\delta0}}{\sigma_{\delta}}, \quad (6.2)$$

where D_{IBS} , σ_z and σ_{δ} are the IBS diffusion coefficient, spatial- and rms momentum spread and D_{IBS0} , σ_{z0} and $\sigma_{\delta0}$ the initial values. The equilibrium rms momentum spread is calculated by the combination of Eq. 5.6 and Eq. 6.2 and yields

$$\sigma_{\delta} = \sqrt[3]{\frac{2D_{IBS0}\sigma_{\delta0}T_{rev}\sigma_{\delta Laser}^2}{\langle\Delta\delta^{LF}\rangle\rho_{scat}(0)\delta_{Lpos}}}. \quad (6.3)$$

The simulation results are compared to the analytic estimation in fig. 6.1. The equilibrium rms momentum spread is shown for titanium ions in the SIS100 with the pulsed laser. The pulsed laser system follows the optimal configuration given in Eq. 5.12 and 5.13. The simulation results for a single pulsed laser system are well described by the rms rate equations. In addition the final rms momentum spread is determined for the combination of two pulsed laser systems. The width of the second laser system is set to $\sigma_{\delta Laser2} = 10^{-6}$ in order to achieve lower rms momentum spreads as discussed in Sect.

5.3. The final rms momentum spread is estimated by Eq. 6.3 using the values of the second laser system. For low ion intensities the rms momentum spread of the ion bunch reaches the width of the narrow band laser force $\sigma_\delta \lesssim \sigma_{\delta Laser2}$ and agrees with the analytic estimation. If the ion intensity is too high, only a small fraction of the ions interact with the second laser and the equilibrium rms momentum spread remains between the rms rate limits calculated for the two individual laser systems. In this case, the second laser does not improve the cooling process.

6.1.2 Continuous Wave Laser

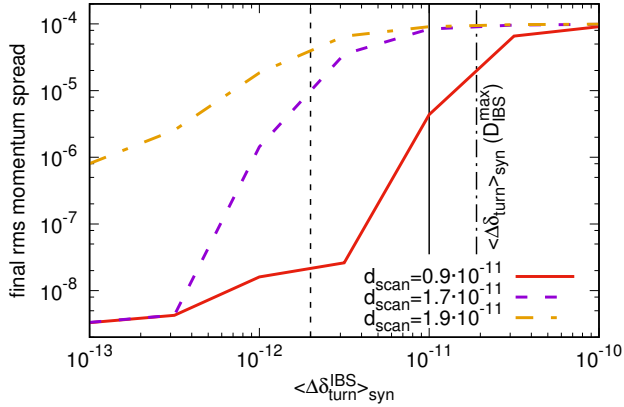


Figure 6.2: Final rms momentum spread after cw laser cooling for different strength of IBS heating. Simulation results are shown for titanium ions in the SIS100. The maximum IBS strength D_{IBS}^{max} is marked, which corresponds to the theoretical limit of $d_{scan} = 0$. The maximum IBS strength is marked for $d_{scan} = 1.7 \cdot 10^{-11}$ and $d_{scan} = 0.9 \cdot 10^{-11}$. The maximum IBS strength for $d_{scan} = 1.9 \cdot 10^{-11}$ is at $\langle \Delta \delta_{turn}^{IBS} \rangle_{syn} = 0$.

The cw laser force produces non-Gaussian beam profiles during the laser cooling process as described in more detail in Sect. 5.1. For these bunch shapes the conventional heating rate of diffusion, which is used for the calculation of the equilibrium state with a pulsed laser, is not valid. The crucial process for the success of the cooling process is the influence of IBS on the dense ring, which is created by the laser force at the bunch boundary in phase space (see fig. 5.3).

The condition for a successful cooling process without intensity effects is given by the balance of the laser scan speed in phase space and the cw laser force (see Eq. 5.2).

In presence of IBS the condition is extended by an additional IBS heating term, which counteracts the cooling process,

$$d_{scan}^{max} \approx \langle \Delta \delta_{turn}^{LF} \rangle_{syn} - \langle \Delta \delta_{turn}^{IBS} \rangle_{syn}, \quad (6.4)$$

where $\langle \Delta \delta_{turn}^{IBS} \rangle_{syn}$ describes the broadening of the dense ring in phase space by IBS in units of relative momentum per turn averaged over the synchrotron motion. Consequently the maximum scan speed d_{scan}^{max} depends on the difference of the cooling strength of the cw laser system and the IBS heating of the dense ring in phase space.

For the calculation of the IBS induced broadening of the dense ring, its cross section is assumed to be Gaussian. The width $\sigma_{\delta ring}$ of the cross section in units of relative momentum is defined at the longitudinal position $z = 0$ and is assumed to be equal to the width of the laser force

$$\sigma_{\delta ring} \approx \frac{\Delta_{fwhm}}{2\sqrt{2 \log 2}}. \quad (6.5)$$

The broadening of the cross section of the dense ring is described by the conventional IBS growth rate

$$\tau_{IBS}^{-1} = \frac{D_{IBS}}{\sigma_{\delta ring}^2}, \quad (6.6)$$

where the diffusion coefficient D_{IBS} is calculated with the line density of the whole bunch. The increase of the width of the dense ring in phase space is calculated by

$$\langle \Delta \delta_{turn}^{IBS} \rangle_{syn} = \sigma_{\delta ring} \left(e^{T_{rev} \cdot \tau_{IBS}^{-1}} - 1 \right) \cdot \frac{2}{\pi} \quad (6.7)$$

$$\approx \sigma_{\delta ring} T_{rev} \cdot \tau_{IBS}^{-1} \cdot \frac{2}{\pi}. \quad (6.8)$$

The factor $2/\pi$ arises by averaging the diffusive heating over the synchrotron motion.

Equation 6.4 defines the IBS limit for a defined scan speed of the laser resonance. The highest ion intensity, respectively the maximum diffusion coefficient of the initial bunch, is given for the limiting case $d_{scan} = 0$ by

$$D_{IBS0}^{max} \approx \frac{\langle \Delta \delta_{turn}^{cw} \rangle_{syn} \cdot \Delta_{fwhm} \cdot \pi}{4\sqrt{2 \log 2} \cdot T_{rev}}. \quad (6.9)$$

Figure 6.2 shows the success of the cooling process for different strengths of IBS and different scan speeds of the laser resonance for the cooling process of titanium ions in the SIS100. The analytically predicted maximum IBS strengths for different laser scan speeds are marked by vertical lines. Higher ion intensities can be cooled with a slower

scan of the laser resonance. But the reduction of the scan speed significantly below the maximum value without IBS (see Eq. 5.2) is not efficient, because the cooling process of a bunch with marginal higher ion intensity requires much more time.

Note that the analytic prediction assumes a fast synchrotron motion and a small perturbation of the synchrotron motion by the laser force. The analytic results become inaccurate for low synchrotron frequencies and strong perturbations by the laser force (see Sect. 5.1).

6.2 Space Charge

The second intensity effect that strongly affects the particle dynamics during the laser cooling process is space charge. Space charge does not necessarily heat up the particle ensemble but influences the trajectory of the ions. The effect is described in Sect. 2.2 and the implementation in the simulation tool is explained in Sect. 4.1. The relevant space charge effects during the laser cooling process are discussed in the following.

6.2.1 Bunch Length Limit

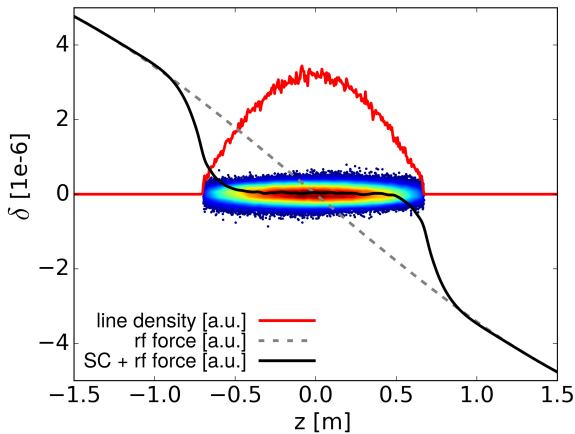


Figure 6.3: Equilibrium state of space charge (SC) and rf potential $U_{sc}(z) = -U_{rf}(z)$. Inside the ion distribution the sum of the rf and space charge force vanishes.

During the cooling process with a cw laser as well as a pulsed laser system the line density of the ion beam $\lambda(z)$ increases. Consequently the space charge potential be-

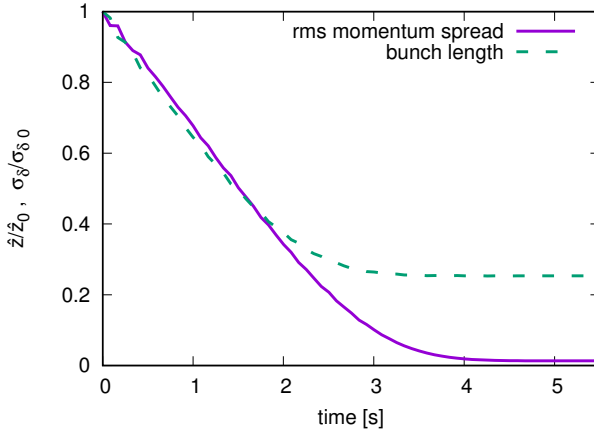


Figure 6.4: Relative reduction of the bunch length and rms momentum spread during pulsed laser cooling. The bunch length and rms momentum spread are normalized to the initial values and shown for titanium ions in the SIS100. Neglecting space charge and non-linearities in the rf bucket, the relative reduction is equal for both quantities. In presence of space charge the bunch length is limited to L_{equ} (see Eq. 6.11).

comes stronger as described by Eq. 2.23. The ion density limit is reached when the space charge potential fully cancels the externally applied rf potential. A higher repelling space charge force than the attractive rf force avoids a stable area in phase space and does not exist for stationary distributions. The shortest possible bunch length L_{equ} in the rf bucket is calculated by

$$U_{sc}(z) + U_{rf}(z) = 0 \quad \text{for } |z| \leq \hat{z}_{equ}, \quad (6.10)$$

where \hat{z}_{equ} denotes the position of the bunch boundary particle at equilibrium. Assuming a final state in the linear region of the bucket, the combination of Eq. 2.13, 2.21 and 2.23 results in the shortest bunch length

$$L_{equ} = 2 \cdot \hat{z}_{equ} = \sqrt[3]{\frac{3qL_{acc}^2 g_{sc} N_p}{2\pi^2 h \epsilon_0 \gamma^2 \dot{U}_{rf}}}. \quad (6.11)$$

The scaling of the bunch length with respect to the rf voltage and the particle number agrees with the results of laser cooling experiments presented in Ref. [55].

The phase space distribution and the sum of the external rf and space charge force are illustrated in fig. 6.3. Within the ion bunch the combined force is zero. The smooth transition at the boundaries of the bunch originates in the finite space charge cut off frequency (see Eq. 2.29). By varying the rf voltage the bunch length can be modified.

Despite space charge limits the shortest bunch length, the equilibrium state of the space charge and rf potential does not limit the rms momentum spread. The evolution of the rms momentum spread and bunch length is shown in fig. 6.4 exemplary for the cooling process of titanium ions in the SIS100 with a pulsed laser system. In absence of space charge and non-linearities of the rf bucket, the reduction of the bunch length and the rms momentum spread during the cooling process, normalized to the initial values, are equal (see fig. 5.3). After the cooling process both quantities are reduced by the same factor. In presence of space charge the bunch length stagnates at the equilibrium state whereas the reduction of the rms momentum spread continues. The rms momentum spread is limited by the previously described IBS heating or the Doppler limit.

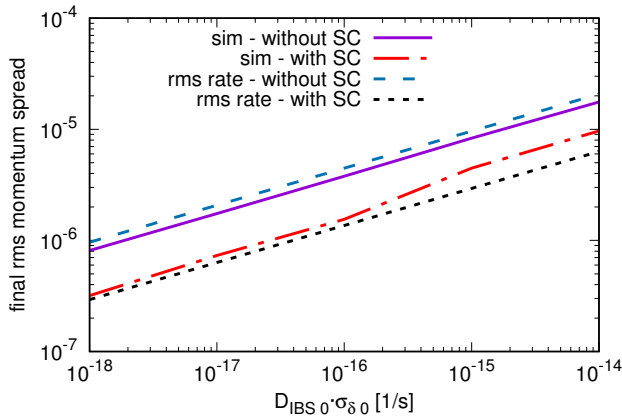


Figure 6.5: Equilibrium rms momentum spread for IBS heating, space charge and pulsed laser cooling. The results in fig. 6.1 are extended by space charge (SC). The limitation of the bunch length by space charge leads to a reduction of the equilibrium rms momentum spread.

The limitation of the shortest bunch length influences the effect of IBS and the general dynamics of the ions in the equilibrium state. The calculation of the IBS equilibrium for the cooling process with a pulsed laser system (see Sect. 6.1.1) assumes an equal reduction of the bunch length and the rms momentum spread. In presence of space

charge the reduction of the rms momentum spread and the bunch length are no longer correlated and Eq. 6.2 is modified to

$$\tau_{IBS}^{-1} = \frac{D_{IBS0}}{\sigma_\delta^2} \cdot \frac{2\hat{z}_0}{L_{equ}}, \quad (6.12)$$

where \hat{z}_0 is the half length of the initial bunch. The limitation of the shortest bunch length defines an upper boundary of the IBS heating rate and the rms momentum spread of the IBS equilibrium for a pulsed laser system is reduced to

$$\sigma_\delta = \sqrt{\frac{4D_{IBS0} T_{rev} \sigma_{\delta Laser}^2}{\langle \Delta \delta^{LF} \rangle \rho_{scat}(0) \delta_{Lpos} L_{equ}}} \frac{\hat{z}_0}{L_p} \propto N_p^{1/3}. \quad (6.13)$$

The analytic estimation is compared to simulation results for titanium ions in the SIS100 in fig. 6.5. Equation 6.13 describes the simulation results properly. The small deviation at high IBS diffusion coefficients originates in the strong noise of the space charge solver for these configurations. The reduction of the rms momentum spread by space charge depends on the beam parameters and bucket configuration and is in the simulated configuration ≈ 2.5 , independent of the ion intensity.

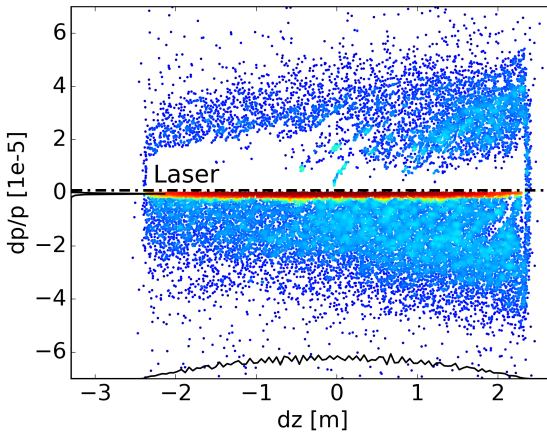


Figure 6.6: Beam blow up at the final state of the cooling process. Due to the compensation of the rf potential by space charge, the ions do not interact with the cooling force for a long period of time and intensity effects like IBS heat up the cold ion bunch.

In addition the space charge compensation of the rf potential leads to a very slow synchrotron motion of the ions at the final state. In the linear region of the sinusoidal bucket without space charge, the synchrotron period is independent of the momentum deviation of the ions and is constant during the laser cooling process. The reduction of the bucket forces by space charge slows down the synchrotron motion. At the final state of the cooling process the motion of the ions in the compensated rf bucket is similar to the motion in a barrier bucket as explained in Sect. 5.4. Within the bunch the sum of the forces vanishes and the ions travel with constant speed. The synchrotron period of an ion with a momentum deviation $\delta \ll \sigma_{\delta 0}$ is

$$T_{syn} = \frac{2L_{equ}}{v_z} = -\frac{2L_{equ}}{\eta\beta c_0} \cdot \frac{1}{\delta}. \quad (6.14)$$

For ions with a low relative momentum deviation, the motion in the bucket becomes very slow. The ions move in the compensated rf bucket and heat up by intensity effects like IBS. At phase space positions with $\delta > 0$ the ions interact with the laser light, while for $\delta < 0$ the ions experience no cooling force. For strong heating rates the ions are pushed far away from the resonant momentum of the laser light during the half of synchrotron period with $\delta < 0$. The ions do not interact with the cooling force after the half synchrotron motion and escape from the cold beam core. The blow up of the ions at the final state prevents very low momentum spreads of ion beams with strong space charge as exemplary shown in the phase space plot in fig. 6.6.

6.2.2 Continuous Wave Laser

The cooling process with a cw laser system creates non-Gaussian beam profiles and strongly increases the local ion density at the boundaries of the bunch as shown in the phase space plot in fig. 5.3. The arising longitudinal phase space distribution with a dense ring enclosing the bunch is a very exotic distribution. The stability of this distribution has not been studied yet. The peaks in the ion distribution at the boundaries of the bunch create strong space charge forces which trigger a microwave instability and a local rf compensation. Both effects lead to a broadening or entire clearance of the dense ring in phase space. Hence at most only one effect occurs during the cooling process which leads to a change of the distribution function and a prevention of the other effect. The two effects are discussed in the following.

6.2.2.1 Local rf-Compensation

The smooth transition of the initial distribution to the final distribution with a space charge limited bunch length, as shown in fig. 6.4, only exists for the cooling process with a pulsed laser. The pulsed laser force keeps the ion distribution similar to a Gaussian shape during the whole cooling process and the ratio of the space charge force to the

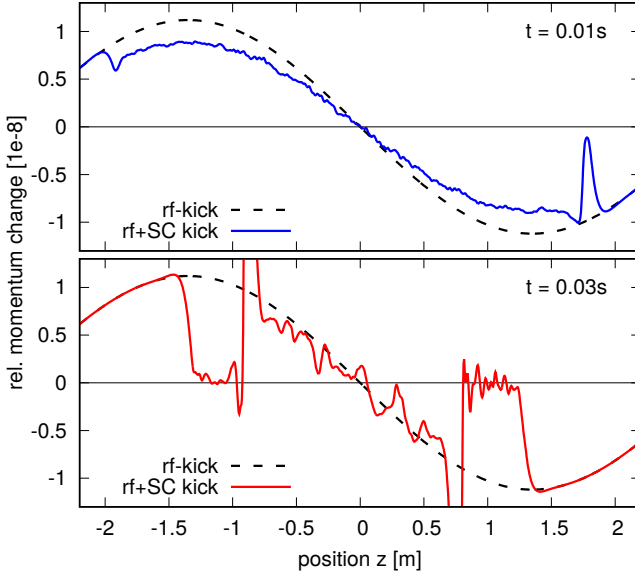


Figure 6.7: Space charge and rf forces during the local rf compensation. The forces are given for the cooling process of carbon ions in the ESR. The corresponding phase space distributions are shown in fig. 6.8.

rf force ($U_{sc}(z)/U_{rf}(z)$) is approximately equal for all positions within the ion bunch. During the cooling process with cw laser system the ion density increases locally and the distribution function $\lambda(z)$ is strongly non Gaussian. For the created bunch distributions the ratio of $U_{sc}(z)/U_{rf}(z)$ strongly differs at different positions within the ion bunch. The compensation of the rf force by the space charge force

$$U_{sc}(z)/U_{rf}(z) = -1 \quad (6.15)$$

occurs locally and not simultaneously at all positions within the ion bunch. The space charge forces during the cooling process with a cw laser system are shown in fig. 6.7 and the evolution of the phase space density in fig. 6.8. The cooling process of $N_p = 1.5 \cdot 10^6$ lithium-like carbon ions in the ESR (see detailed parameter list in Sect. 7.2) is simulated instead of titanium ions in the SIS100 because the cooling process of titanium ions show the microwave instability which is explained in the following section and prevents the local rf compensation. At $t = 0.01s$ the space charge force of the dense peak at the boundary of the bunch almost compensates the rf force at $z \approx 1.7m$ and the combined force is almost zero. As a result the ions stop performing the synchrotron motion and accumulate at this position. Ions accumulate until the space charge force

fully compensates the rf force and form an partly parabolic line density with $U_{sc}(z) + U_{rf}(z) = 0$ as shown in fig. 6.7 for $z > 0.8m$ and $z < 0.8m$ at $t = 0.03s$. Figure 6.8 shows the accumulation of ions at $\delta \approx 0$ during the local rf compensation. The fluctuations of the locally strong space charge force leads to a chaotic motion of the ions in phase space. However, this effect does not necessarily prevent the cooling process. The ions are successfully laser cooled except a small fraction that is lost behind the laser force due to the strong and chaotic space charge forces.

The threshold for the development of the local rf compensation and the chaotic motion is given by Eq. 6.15. However, the maximum ion intensity depends on the exact shape of the ion distribution and on the detailed space charge fields. Therefore no analytic formula for the threshold of the local rf compensation depending on beam parameters and ion intensity is given.

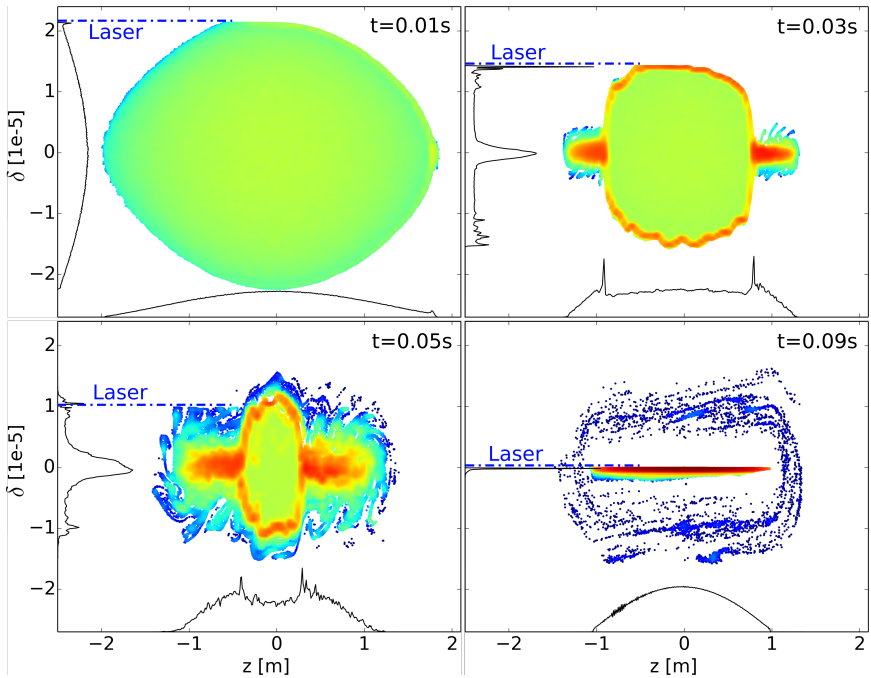


Figure 6.8: Evolution of the phase space density during the local rf compensation. The results are shown for cw laser cooling of carbon ions in the ESR. The rf compensation leads to chaotic motion of the ions which does not necessarily prevent the successful cooling process.

6.2.2.2 Microwave Instability

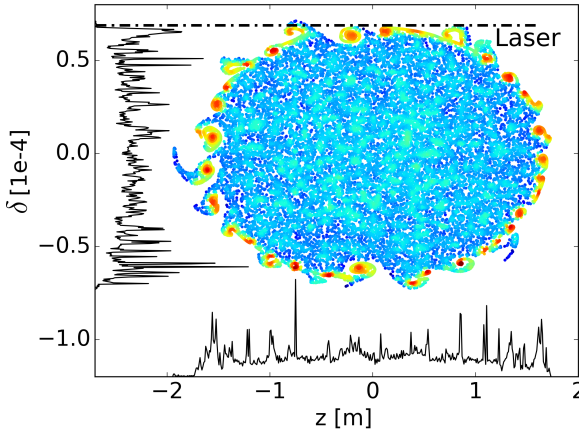


Figure 6.9: Phase space density during the microwave instability. The results are shown for cw laser cooling of titanium ions in the SIS100. Space charge creates micro bunches of the dense ring in phase space which counteract the cooling process.

Space charge triggers a collective instability during the cooling process with a cw laser excitation. A snapshot of the instability is shown in fig. 6.9. The dense ring in phase space which is created by the narrow band cw laser force (see fig. 5.3), becomes unstable and creates micro bunches. The micro bunches lead to a broadening of the dense ring and counteract the laser cooling process.

For the detailed investigation of the collective instability, the evolution of an isolated ring in phase space is simulated without the laser force. The macro particles are positioned on an ellipse in phase space with the amplitudes z_{ring} and δ_{ring} in longitudinal position and momentum. The amplitudes z_{ring} and δ_{ring} satisfy the condition for a matched distribution as discussed in Sect. 2.1. For simplicity the dense ring stays in the linear region of the rf bucket. The density of the ring is slightly modulated in a sinusoidal shape for an equally distributed initial perturbation. The evolution of the phase space distribution is shown in fig. 6.10. Due to space charge fields, the amplitude of the perturbation increases. At $t = 0.08$ s the dense ring starts to create small micro bunches which circulate in the rf bucket. The width of the ring increases significantly.

The instability shows similarities with the negative mass instability. The negative mass instability occurs in synchrotrons which operate above transition energy ($\gamma >$

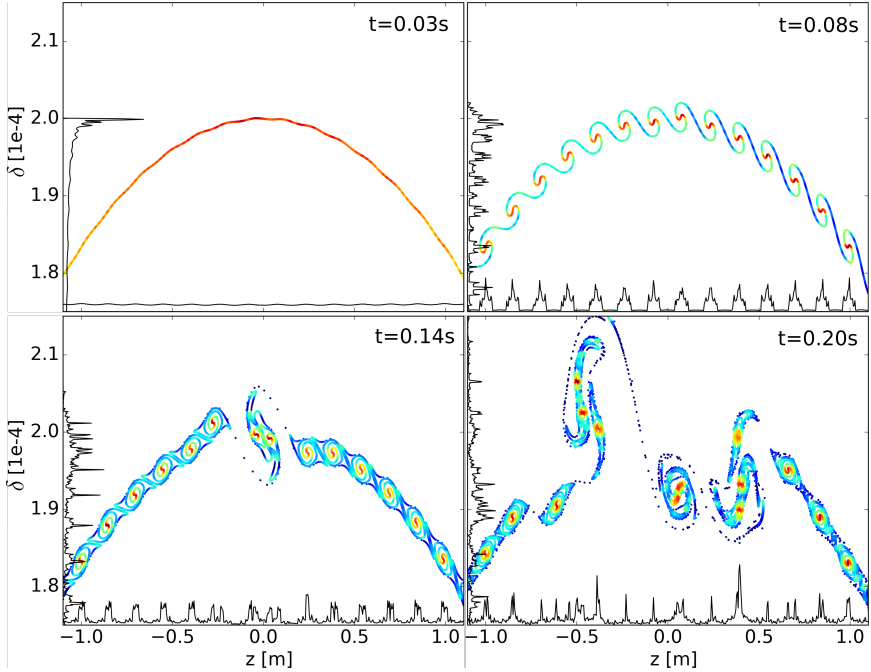


Figure 6.10: Evolution of the phase space density of isolated ring under influence of space charge. The results are shown for titanium ions in the SIS100 without a laser force. The initial perturbation grows and creates micro bunches.

γ_t). As a consequence the velocity v_z changes sign (see Eq. 2.9) and particles with higher momentum take more time for one revolution in the synchrotron compared to particles with a lower momentum. The space charge force accelerates particles which are located ahead and decelerate particles which are located behind the perturbation. Due to the opposite sign for the relation between the momentum and the velocity in the co-moving frame, the particles move towards the higher density and an initially small density perturbation grows. More information about the negative mass instability can be found e.g. in Ref. [28].

For the distribution of the ring in phase space, space charge causes the same effect as in the negative mass instability. For the detailed investigation of the instability the

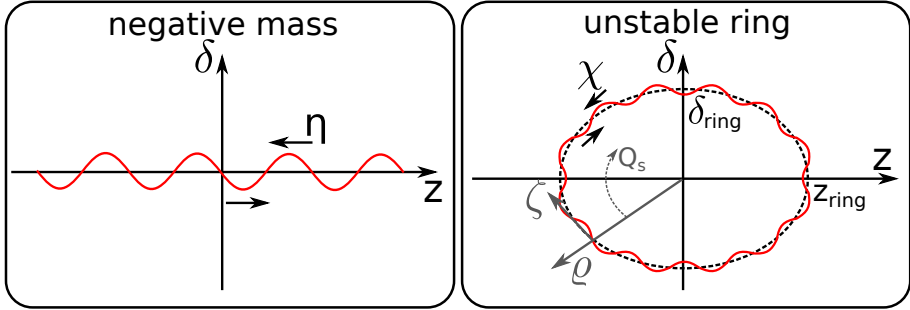


Figure 6.11: Comparison of the negative mass instability and the unstable ring. The space charge induced synchrotron tune shift χ acts like the slip factor η in the negative mass instability.

longitudinal phase space coordinates of the co-moving frame are transformed into a polar-like coordinate system. The new coordinates are given by

$$\varrho = \sqrt{\delta^2 + \left(\frac{\delta_{ring}}{z_{ring}} \cdot z \right)^2} \quad (6.16)$$

$$\zeta = z_{ring} \cdot \left(\arctan \left(\frac{z_{ring} \cdot \delta}{z \cdot \delta_{ring}} \right) - 2\pi \frac{t}{T_{rev}} \cdot Q_s \right). \quad (6.17)$$

The radial position in longitudinal phase space of the co-moving frame is denoted by ϱ . The coordinate ζ describes the angular position in phase space of the co-moving coordinate system. The origin of the coordinate system rotates with the speed of the synchrotron motion. In order to keep convenient units, ζ and ϱ are normalized to meters and relative momentum. The coordinate transformation is illustrated in fig. 6.11.

The unperturbed motion of a particle in the linear region of the rf bucket follows constant values of ϱ and ζ . For an initial higher density at $\zeta = 0$, space charge pushes ions with $\zeta > 0$ to higher radial positions ϱ , while ions with $\zeta < 0$ are pushed to lower radial position ϱ as shown in fig. 6.10 at $t = 0.03s$ and $t = 0.08s$.

On the other hand the dense peaks at $\pm z_{ring}$ create strong space charge fields as shown in fig. 6.12. These space charge peaks induce a synchrotron tune shift which depends on the radial position ϱ in phase space. As observed in fig. 6.10 ions with larger radial position ($\varrho > \delta_{ring}$) are going backwards in ζ and ions with a smaller radial position ($\varrho < \delta_{ring}$) moving forward in ζ . This implies a gradient of the synchrotron tune at $\varrho \approx \delta_{ring}$. The space charge induced synchrotron tune shift is depicted in fig. 6.13 for the numerical simulation of the dense ring in fig. 6.10.

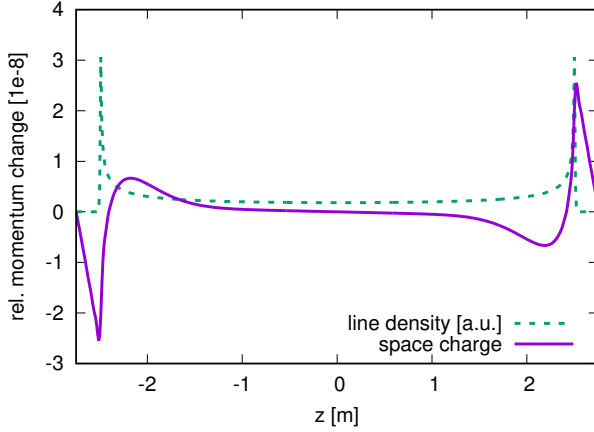


Figure 6.12: Ion line density and space charge kick for the isolated ring in phase space.

For further calculations the mean synchrotron tune shift can be described by a linear approximation for ions close to $\varrho \approx \delta_{ring}$ with the gradient

$$\chi = - \left. \frac{d\Delta Q_s}{d\varrho} \right|_{\varrho=\delta_{ring}} . \quad (6.18)$$

As shown in fig. 6.13 the straight line serves as a good approximation for small displacements. The effect of the synchrotron tune shift on a radial displacement and the similarities with the negative mass instability are sketched in fig. 6.11. For the presented instability the tune shift derivative χ acts equivalent to the slip factor η in the negative mass instability. The main difference is that η is constant in time and defined by the lattice function and χ depends on the ion distribution and is not necessarily constant in time.

The analytic description of the space charge instability of the dense ring in phase space is derived by solving the Vlasov equation in the polar-like coordinate system that is illustrated in fig. 6.11. The Vlasov equation is given by

$$\frac{df}{dt} = \frac{\partial f}{\partial t} + \frac{\partial \varrho}{\partial t} \cdot \frac{\partial f}{\partial \varrho} + \frac{\partial \zeta}{\partial t} \cdot \frac{\partial f}{\partial \zeta} = 0, \quad (6.19)$$

where ϱ and ζ describe the new coordinates that are defined in Eq. 6.16 and 6.17. The derivatives $\partial \varrho / \partial t$ and $\partial \zeta / \partial t$ depend strongly on the position in phase space. The space charge tune shift which is created by the space charge forces at the head and tail

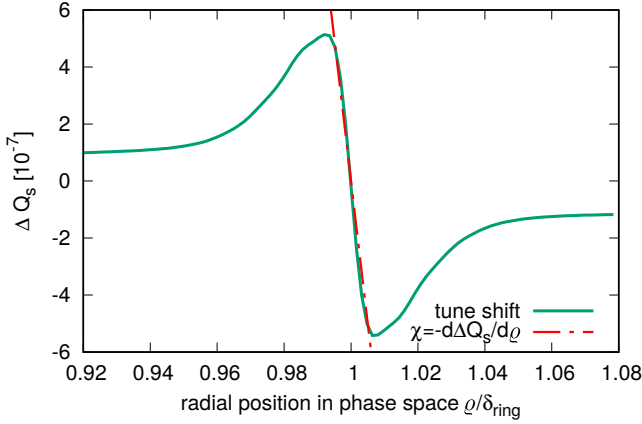


Figure 6.13: Space charge induced synchrotron tune shift. The tune shift triggers the microwave instability of the dense ring and is given for an initial synchrotron tune of $Q_s = 3.5 \cdot 10^{-4}$.

of the bunch, arises on a small fraction of the synchrotron motion. In order to solve Eq. 6.19 for the given case, the derivatives are averaged over the synchrotron motion and Eq. 6.19 evolves to

$$\frac{\partial f}{\partial t} + \left\langle \frac{\partial \rho}{\partial t} \right\rangle_{syn} \cdot \frac{\partial f}{\partial \rho} + \left\langle \frac{\partial \zeta}{\partial t} \right\rangle_{syn} \cdot \frac{\partial f}{\partial \zeta} = 0. \quad (6.20)$$

This simplification claims that the analyzed process is slow compared to the synchrotron motion.

For the Vlasov equation the phase space distribution function f is given by an ellipse in phase space as depicted in fig. 6.11. Following the nomenclature of the derivation for the negative mass instability (see e.g. Ref. [28]), the distribution function f consists of a small sinusoidal perturbation f_1 with wave vector k on top of a beam f_0 with constant density. For the presented instability the distribution function reads

$$f = f_0 + f_1 \quad (6.21)$$

$$f_0 = \frac{N_p}{2\pi z_{ring}} \cdot \delta(\rho - \delta_{ring}) \quad (6.22)$$

$$f_1 \propto e^{i(k\zeta - \omega t)}, \quad (6.23)$$

where $\delta(\cdot)$ denotes the Dirac delta function and assumes that all ions of the initial distribution have the same radial offset ϱ . As a consequence the relation

$$\left(\frac{\delta}{\delta_{ring}}\right)^2 + \left(\frac{z}{z_{ring}}\right)^2 = 1 \quad (6.24)$$

holds for the given initial distribution without perturbation, which is required for further calculations.

The time derivative of the radial position ϱ is given by

$$\frac{\partial \varrho}{\partial t} = \frac{\partial \varrho}{\partial \delta} \cdot \frac{\partial \delta}{\partial t} = \frac{\delta}{\delta_{ring}} \cdot \frac{\partial \delta}{\partial t}, \quad (6.25)$$

where the derivative of the radial position with respect to the relative momentum deviation is calculated using Eq. 6.16 under assumption of Eq. 6.24. The time derivative of the ion momentum is given by the space charge force (see Eq. 2.22). Equation 6.25 evolves to

$$\frac{\partial \varrho}{\partial t} = -\frac{\delta}{\delta_{ring}} \cdot \frac{q^2 g_{sc}}{4\pi\epsilon_0\gamma^2 p_0} \left(\frac{\partial \lambda_0}{\partial z} + \frac{\partial \lambda_1}{\partial z} \right), \quad (6.26)$$

where $\lambda_{0,1} = \int_{-\infty}^{\infty} f_{0,1} d\delta$ is the line density of the distribution function. As illustrated in fig. 6.12 the line density of the unperturbed distribution λ_0 is nearly constant in the center of the bunch and only shows a finite derivative at $z \approx \pm z_{ring}$. At these positions the fraction δ/δ_{ring} becomes very small (see Eq. 6.24). Consequently the space charge force of the initial distribution f_0 acting on the radial position is small $\partial \lambda_0/\partial z \approx 0$ and is neglected in the following. Only the space charge force of the perturbation f_1 is relevant for the change of the radial position ϱ . In order to solve the derivative of the perturbation f_1 the coordinates are transformed into the polar-like coordinate system

$$\frac{\partial \varrho}{\partial t} = -\frac{\delta}{\delta_{ring}} \cdot \frac{q^2 g_{sc}}{4\pi\epsilon_0\gamma^2 p_0} \cdot \frac{\partial \zeta}{\partial z} \frac{\partial \lambda_1}{\partial \zeta}. \quad (6.27)$$

The derivative of the angular position ζ is calculated under the constraint of Eq. 6.24 and the time derivative of radial position ϱ results in

$$\frac{\partial \varrho}{\partial t} = \frac{\delta^2}{\delta_{ring}^2} \cdot \frac{q^2 g_{sc}}{4\pi\epsilon_0\gamma^2 p_0} \cdot ik\lambda_1. \quad (6.28)$$

After averaging over the synchrotron motion the derivative is independent of δ and z

$$\left\langle \frac{\partial \varrho}{\partial t} \right\rangle_{syn} = \frac{1}{2} \cdot \frac{q^2 g_{sc}}{4\pi\epsilon_0\gamma^2 p_0} \cdot ik\lambda_1. \quad (6.29)$$

The derivative of the angular position ζ with time is given by the space charge induced synchrotron tune shift. Under the assumption of a linear synchrotron tune shift as described by Eq. 6.18 the change of the angular position in phase space is calculated by

$$\left\langle \frac{\partial \zeta}{\partial t} \right\rangle_{syn} = \frac{\partial}{\partial t} z_{ring} \frac{2\pi t}{T_{rev}} \Delta Q_s \quad (6.30)$$

$$= -\frac{2\pi z_{ring}}{T_{rev}} (\varrho - \delta_{ring}) \cdot \chi. \quad (6.31)$$

Finally the Vlasov equation for the evolution of the dense ring in phase space results in

$$\frac{\partial f}{\partial t} + \frac{1}{2} \cdot \frac{q^2 g_{sc}}{4\pi\epsilon_0\gamma^2 p_0} \cdot ik\lambda_1 \cdot \frac{\partial f}{\partial \varrho} - \frac{2\pi z_{ring}}{T_{rev}} (\varrho - \delta_{ring}) \cdot \chi \cdot \frac{\partial f}{\partial \zeta} = 0. \quad (6.32)$$

This partial differential equation determines the growth rate of the perturbation for the distribution function written in Eq. 6.21. The equation is solved equivalent to the negative mass instability in a coasting beam described in Ref. [28]. The exponential growth rate of the sinusoidal density modulation with wave vector k is

$$\tau_{mw}^{-1} = -i\omega_{mw} = k \sqrt{\frac{q^2 g_{sc} N_p \chi}{8\pi\epsilon_0 m \gamma^3 L_{acc}}}. \quad (6.33)$$

In comparison to the analytic description of the negative mass instability, the derivative χ of the synchrotron tune takes the part of the slip factor η . The main difference is that the derivative of the synchrotron tune spread is typically much smaller than the slip factor and the instability rises much slower. The width of the ring in radial position ϱ_{rms} over time is shown in fig. 6.14 during the rise of the microwave instability. The instability develops over several synchrotron periods, as required for the averaging of the Vlasov equation over the synchrotron motion (see Eq. 6.20). At $t \approx 6 \cdot T_s$ the growth of the instability is counteracted by the decoherence of the density modulation. The synchrotron tune spread causes a diffusion of the micro bunches with the decay rate

$$\tau_{decoher}^{-1} = k \frac{2\pi z_{ring} \chi}{T_{rev}} \varrho_{rms}. \quad (6.34)$$

For an equal growth and damping rate of the instability ($\tau_{mw}^{-1} + \tau_{decoher}^{-1} = 0$), the growth of the instability stagnates. Furthermore this equilibrium defines the threshold for the

instability, similar to the Keil-Schnell stability criterion (see Ref. [62]) for the conventional microwave instability. The dense ring in phase space is stable for

$$\varrho_{rms}^2 > N_p \cdot \frac{q^2 g_{sc} L_{acc}}{32\pi^3 z_{ring}^2 m\beta^2 c_0^2 \gamma^3 \chi}. \quad (6.35)$$

However, the particular equilibrium width of the dense ring is practically hard to define, because it depends on the space charge tune shift χ , which depends again on the distribution function. During the cooling process or growth of the instability the distribution function drastically changes and influences the equilibrium of the instability.

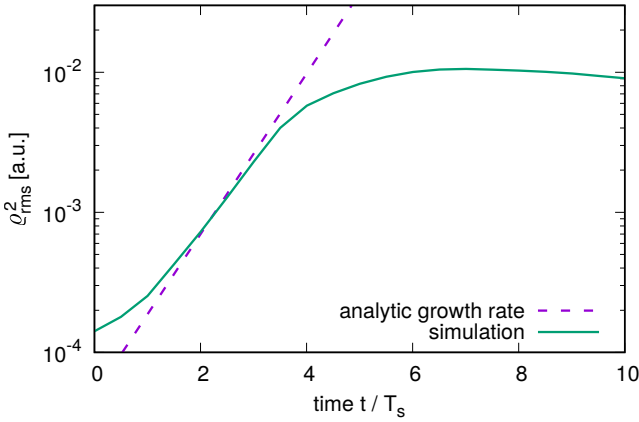


Figure 6.14: Growth of the microwave instability of the dense ring in phase space. The width of dense ring ϱ_{rms} is shown over time in units of the synchrotron period $T_s = T_{rev}/Q_s$. The wave vector of the initial perturbation is $k = 60 \frac{1}{m}$ and the synchrotron tune shift is shown in fig. 6.13.

Beside the decoherence the laser force influences the growth of the instability during the cooling process. The cw laser force acts on the dense ring in phase space and counteracts its broadening. However, the laser force only changes the radial position ϱ of the ions and does not affect the density modulation of the dense ring. The laser force slows down the instability but is not able to fully prevent the creation of micro bunches.

Nevertheless the instability does not necessarily lead to a failure of the laser cooling process. In numerical simulations, the instability usually leads to an additional broadening of the ring similar to the heating effect of IBS, described in Sect. 6.1.2. Above a certain ion intensity, the laser force is not strong enough to counteract the broadening of the ring and ions are lost for the cooling process. The exact threshold for the failure

of the cooling process depends on the detailed evolution of the phase space distribution during the cooling process and the high frequency space charge force. Therefore an analytic expression for the maximum ion intensity during the laser cooling process is not given and has to be evaluated by numerical simulations.

7 Prospects for Relativistic Ion Beams

This chapter deals with the ability and efficiency of laser cooling at relativistic beam energies. The previously discussed constraints for a successful laser cooling process and ion intensity limitations are evaluated for different ions at different relativistic factors γ . In order to combine the different aspects of laser cooling, the cooling process of titanium ions in the SIS100 is exemplary studied and compared to numerical simulations of carbon ions in the ESR.

7.1 Scaling Laws of Cooling Process

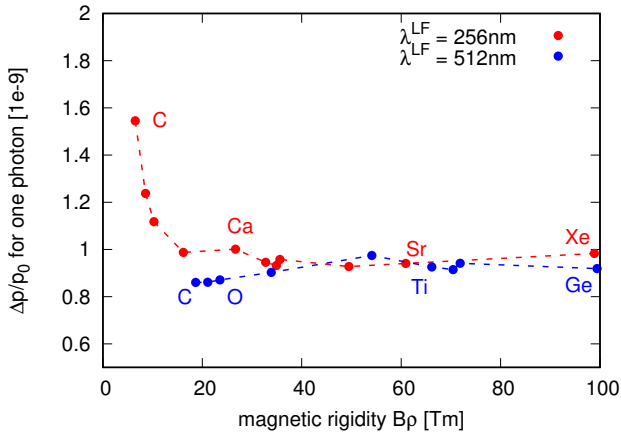


Figure 7.1: Mean momentum change of a resonant interaction in the LF. The momentum transfer normalized to the initial momentum is approximately constant. The results are shown for lithium-like ions using transition data from fig. 3.3. Different dots represent different ions that are partly marked by name.

For the scaling of the laser force and the laser cooling process with the relativistic factor γ , the resonant condition of the laser wavelength with the atomic transition of the relativistic ions has to be satisfied. The transformed laser wavelength in the PF has to match the energy gap of the atomic transition, as described by the condition

in Eq. 3.5. For a constant laser wavelength in LF the change of the relativistic factor requires a change of the energy gap of the atomic transition. Focusing on the $2s_{1/2} \rightarrow 2p_{1/2}$ transition in lithium-like ions and the two wavelengths ($\lambda^{LF} = 256 \text{ nm}; 512 \text{ nm}$), that will be available for experiments at the SIS100, the required magnetic rigidity for different ions is illustrated in fig. 3.4. The following scaling laws of different γ hold the resonant condition for the two fixed wavelengths in LF and different lithium-like ions and are plotted against the required magnetic rigidity.

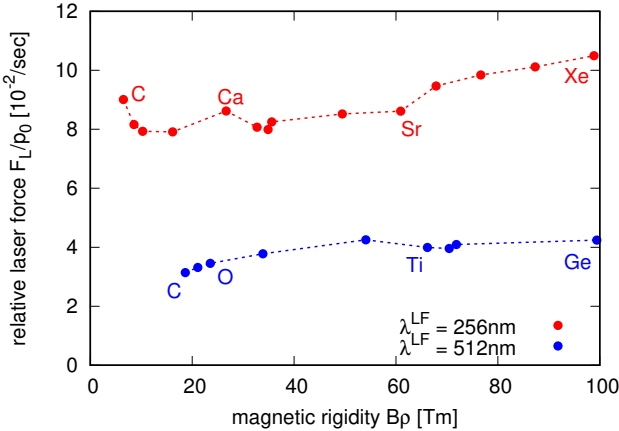


Figure 7.2: Relative laser force of a cw laser system in units of relative momentum for a saturated transition $S = 1$. The quantity corresponds to the relative momentum change per time for an ion which is permanently in resonance with the laser light. The results are shown for lithium-like ions using transition data from fig. 3.3. Different dots represent different ions that are partly marked by name.

The mean momentum transfer for one resonant interaction is calculated by Eq. 3.9 and evaluated for lithium-like ions in fig. 7.1. Despite the absolute value of the photon momentum strongly increases for higher relativistic factors ($\Delta p^{LF} \propto \gamma^2$), the relative momentum change of the ions is approximately constant for different lithium-like ions. The higher mass of ions which are cooled at higher relativistic factors, and the general scaling of the ion momentum with the relativistic factor lead to a similar scaling of the initial momentum p_0 as the resonant photon momentum. Hence the relative momentum change and the impact on beam dynamics for a single spontaneous emission is very similar for different lithium-like ions at relativistic beam energies (see fig. 7.1).

The excitation with a pulsed laser system is restricted to a maximum of one spontaneous emission per ion per laser pulse (see Sect. 3.2.2). If enough laser power is available in order to excite all resonant ions ($\rho_{excite} = 1$), the strength of the pulsed

laser is proportional to the results in fig. 7.1 and approximately constant for different relativistic factors.

The strength of the cw laser force depends on the photon momentum and the spontaneous emission rate (see Eq. 3.14). Figure 7.2 shows the cooling force of a cw laser system, normalized to the initial momentum of the ions. The relative cooling force corresponds to the relative momentum change of an ion per time which is permanently in resonance with the laser light. As depicted in fig. 7.2 the cw laser strength is approximately constant for $\lambda^{LF} = 256\text{ nm}$, but is reduced by approximately two for $\lambda^{LF} = 512\text{ nm}$. However the calculation of the laser force assumes the laser intensity to be equal to the saturation intensity $S = 1$. In case the laser system is not strong enough to reach the saturation intensity, the laser strength diminishes as described by Eq. 3.20. For higher relativistic factors the required laser intensity strongly increases (see fig. 3.7). Therefore the actual cw laser force for available laser sources might be much higher for $\lambda^{LF} = 512\text{ nm}$ instead of $\lambda^{LF} = 256\text{ nm}$ because the required laser intensities are lower and stronger laser systems with $\lambda^{LF} = 512\text{ nm}$ are available.

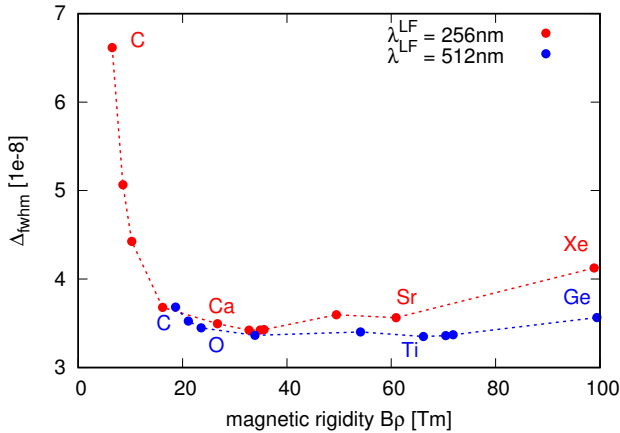


Figure 7.3: Width of the cw laser force in units of relative momentum. The results are shown for lithium-like ions using transition data from fig. 3.3. Different dots represent different ions that are partly marked by name.

Beside the scaling of the momentum change for resonant ions, the width of the cw laser force strongly affects the speed of the cooling process (see Eq. 5.3) and the maximum ion intensity (see eq. 6.9). The width Δ_{fwhm} of the cw laser force in units of relative momentum is calculated by Eq. 3.22 and depicted in fig. 7.3. For different lithium-like ions, the width of the cw laser force is approximately constant. Only for light ions with low values of β the width increases. The results of Δ_{fwhm} assume a saturated transition ($S = 1$) and can be slightly increased for higher saturation parameters,

as described by Eq. 3.22. However for all ions at relativistic energies the width of the laser force is significantly below the initial rms momentum spread of the ion ensemble and the ions have to be cooled by the cw cooling scheme described in Sect. 5.1.

7.1.1 Intensity Limitations

The ion intensity limit of the laser cooling process is reached when the heating effects overcome the strength of the laser cooling force. The heating of the ion ensemble in an accelerator is a combination of different effects, described in Chapter 6.

One effect is the diffusive heating by IBS. The cooling process with a cw laser system fails, if the IBS diffusion coefficient overcomes the threshold defined by Eq. 6.9. For the cooling process with a pulsed laser system the lowest attainable rms momentum spread scales with the IBS diffusion coefficient (see Eq. 6.3). For both cooling schemes the strength of the laser cooling force defines a maximum diffusion coefficient for a successful cooling process. Hence the correlation of the ion density and the diffusion coefficient is a proper indicator for the strength of the counteracting IBS heating for different ions. For equal beam parameters, the IBS diffusion coefficient for different lithium-like ions is depicted in fig. 7.4. For laser cooling at higher magnetic rigidities, the IBS strength decreases and enables the cooling process of higher ion densities, under assumption of equal beam parameters and equal cooling strength.

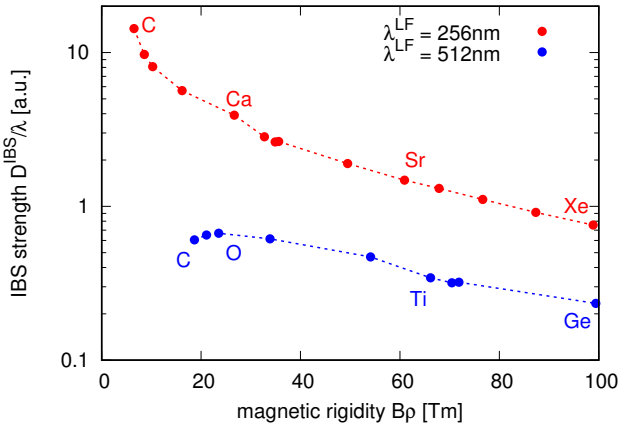


Figure 7.4: IBS strength for different ions during laser cooling in arbitrary units and for equal bunch properties. The results are shown for lithium-like ions using transition data from fig. 3.3. Different dots represent different ions that are partly marked by name.

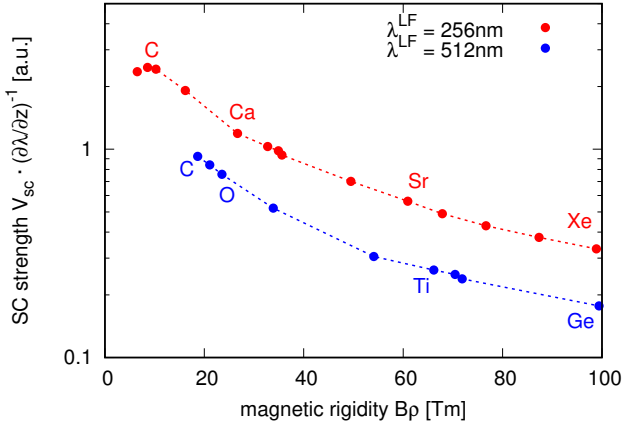


Figure 7.5: Space charge strength for different ions during laser cooling in arbitrary units and for equal bunch properties. The results are shown for lithium-like ions using transition data from fig. 3.3. Different dots represent different ions that are partly marked by name.

The second intensity effect which strongly influences the laser cooling process, is space charge. The different space charge effects which arise during the cooling process, are described in Sect. 6.2 and depend strongly on the rf bucket configuration which is not in general scalable with the relativistic factor. However all presented space charge effects scale with the space charge induced voltage for a given gradient in the longitudinal line density. The space charge voltage for different lithium-like ions for equal bunch properties is shown in fig. 7.5. The voltage is normalized to the gradient in the longitudinal line density. The decrease of the space charge impedance for higher relativistic factors (see Eq. 2.29) is partly compensated by the increasing charge state of ions cooled at higher relativistic factors. Overall the induced space charge voltage slightly decreases for ions cooled at higher magnetic rigidities.

For the cooling process with a pulsed laser system, the strength of space charge and IBS decreases for ions cooled at higher magnetic rigidities. In combination with a constant strength of the laser force, the ion intensity limit of pulsed laser cooling increases at higher magnetic rigidities.

For the cooling process with a narrow band cw laser system, space charge triggers two different instabilities. Both instabilities originate in the dense ring in phase space which is formed by the cw laser force. The projection of the dense ring on the spatial

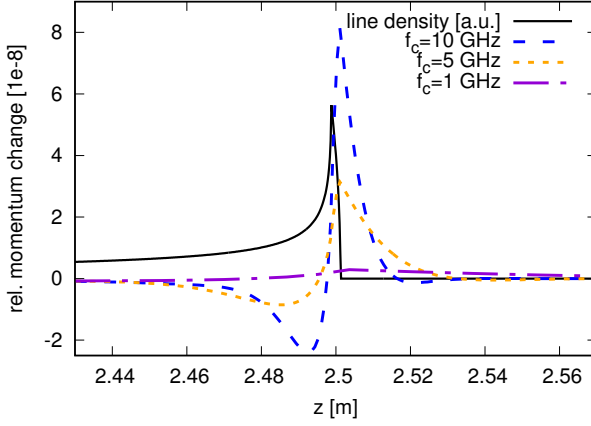


Figure 7.6: Influence of the space charge cut off frequency on the space charge field of the peaks in the longitudinal line density. The ion distribution and rf bucket configuration are equal to the investigation of the microwave instability in Sect. 6.2.2.

coordinate creates pronounced peaks at the head and tail of the bunch (see fig. 5.3). The length of the peaks is estimated by

$$z_{peak} \approx L_{Bunch} \cdot \frac{\Delta_{fwhm}}{\sigma_{\delta 0}} \quad (7.1)$$

and is typically in the range of a few millimeters to centimeters. In presence of strong heating effects the length increases, as described in Sect. 6.1.2. The arising space charge fields depend on the ion beam properties and the space charge cut off frequency. At higher beam energies the space charge strength decreases (see fig. 7.5), but the space charge cut off frequency increases. The corresponding space charge cut off wavelength is calculated by

$$\lambda_c = \frac{c_0}{f_c} = \frac{\pi a \sqrt{g_{sc}}}{\beta \gamma}, \quad (7.2)$$

where a and g denote the beam radius and the geometrical factor, defined in Sect. 2.2. In case the length of the peaks is short compared to the wavelength of the space charge cut off ($z_{peak} \ll \lambda_c$), the longitudinal space charge fields strongly depend on the cut off frequency, because fields above cut off are damped.

The relative momentum kick of the space charge field for the isolated dense ring (see fig. 6.10) for different space charge cut off frequencies is shown in fig. 7.6. For higher space charge cut off frequencies the space charge field becomes stronger and more narrow. For the local rf compensation during the cooling process the peak space charge field defines the threshold. Assuming the peak length to be short compared to the space charge cut off wavelength, the space charge peak scales with $\hat{\delta}_{SC} \propto f_c^{3/2}$ and consequently the maximum ion intensity with $\hat{N}_p \propto f_c^{-3/2}$ for equal properties of the rf bucket.

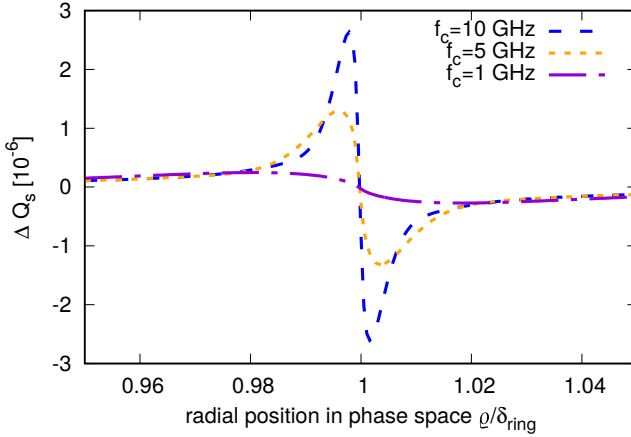


Figure 7.7: Influence of the space charge cut off frequency on the space charge induced synchrotron tune shift. The tune shift is calculated with the space charge force as shown in fig. 7.6.

The microwave instability depends on the derivative χ of the synchrotron tune shift with respect to the radial position in phase space (see Eq. 6.33). The space charge induced synchrotron tune shift of the ellipse in phase space is shown in fig. 7.7. For higher space charge cut off frequencies the synchrotron tune shift increases. The derivative scales with $\chi \propto f_c^{3/2}$ and accelerates the growth of the instability for higher cut off frequencies. Due to the damping of the space charge fields above cut off, the fastest growth rate is given for $k = 2\pi/\lambda_c$ and scales with $\hat{\tau}_{mw}^{-1} \propto f_c^{7/4}$.

Despite the space charge strength decreases for higher relativistic factors (see fig. 7.5), the space charge cut off frequency is proportional to the relativistic factor and enhances the local rf compensation and the microwave instability. Therefore the space charge effects during the cooling process with a cw laser system might be more crucial for higher beam energies. However the detailed threshold of the instabilities and intensity limitations strongly depend on the bucket configuration and have to be evaluated for the properties of the specific cooling process.

7.2 Relativistic Laser Cooling Example

The previously discussed scaling laws show the general trend of laser cooling for different relativistic factors. However the strength of the laser cooling force and the ion intensity limit of a particular cooling process strongly depend on the accelerator properties and the available laser power. For the evaluation of prospects of laser cooling at relativistic energies the cooling process of lithium-like titanium ions in the SIS100 is compared to the cooling process of lithium-like carbon ions in the ESR. Laser cooling of carbon ions was already studied experimentally in the ESR (see Ref. [63, 64, 65]).

The relevant properties of the two accelerators are shown in tab. 7.1. The circumference of the SIS100 is approximately ten times larger compared to the ESR while the laser ion interaction sections are approximately equal in length. Consequently the relative time of the laser ion interaction to the revolution time is much shorter in the SIS100. Due to the possibility of using an electron cooler in the ESR the initial rms momentum spread is assumed to be one order of magnitude below the expected initial rms momentum spread in the SIS100. The electron cooler also reduces the transverse diameter of the ion beam d_{beam} . For an efficient laser cooling process the laser beam is assumed to have the same diameter as the ion beam. For equal output power of the laser system the intensity, seen by the ions, is lower for the larger beam cross-section.

	ESR	SIS100
ion	$^{12}\text{C}^{3+}$	$^{48}\text{Ti}^{19+}$
L_{acc}	108 m	1083 m
T_{rev}	0.8 μs	3.6 μs
$L_{interact}$	25 m	26 m
$\sigma_{\delta 0}$	10^{-5}	10^{-4}
d_{beam}	3 mm	10 mm
γ	1.13	8.50
γ_t	2.4	15
h	20	8

Table 7.1: Properties of the ESR and the SIS100 for the comparison of two laser cooling examples of carbon and titanium ions.

The energy of the ions is adjusted to match the resonant condition for the applied laser wavelength. The properties of the laser systems are given in tab. 7.2. In order to reach the saturation intensity the cooling process of titanium ions is studied with a wavelength of 512 nm. As explained in Ref. [66] much higher laser intensities P_L are available for 512 nm than for 256 nm. For the excitation with a cw laser system the width of the laser force Δ_{fwhm} , the momentum change per spontaneous emission $\Delta\delta^{LF}$ and the mean value of a spontaneous emissions per turn n_{scat} are approximately equal for both examples. The mean momentum change of a resonant titanium ion per revolution

in the accelerator is slightly below of the mean momentum change of a resonant carbon ion.

	cw laser		pulsed laser	
	$^{12}\text{C}^{3+}$	$^{48}\text{Ti}^{19+}$	$^{12}\text{C}^{3+}$	$^{48}\text{Ti}^{19+}$
λ^{LF}	256 nm	512 nm	256 nm	512 nm
$\Delta\delta^{LF}$	$1.5 \cdot 10^{-9}$	$9.3 \cdot 10^{-10}$	$1.5 \cdot 10^{-9}$	$9.3 \cdot 10^{-10}$
E_p	20 mW	5 W	16 nJ	18 μJ
P_L	7.5	4.7	45.8 ps	4.3 ps
n_{scat}	$5.8 \cdot 10^{-8}$	$3.9 \cdot 10^{-8}$	$6.3 \cdot 10^{-6}$	$6.3 \cdot 10^{-5}$
Δf_{whm}			1.25 MHz	278 kHz
			ρ_{excit}	0.278
				$8 \cdot 10^{-5}$

Table 7.2: Properties and strength of the cw and pulsed laser system for the two laser cooling examples.

For the pulsed laser systems the width $\sigma_{\delta_{Laser}}$ and position δ_{LPos} of the excitation probability are set to the optimized values, evaluated by Eq. 5.12 and Eq. 5.13. The repetition rate f_{rep} is assumed to be synchronized to the revolution frequency of the ions in order to achieve a fast cooling process of the ions in one bucket. Assuming the same mean output power of the pulsed laser system and the cw laser system, the energy per laser pulse is given by E_p . The corresponding number of spontaneous emissions per laser pulse for resonant ions is given by ρ_{excit} . For the cooling of carbon ions the pulsed laser intensity is not sufficient to excite all resonant ions ($\rho_{excit} = 1$), but the broadband force is still strong enough to cool the ions in a reasonable time. For titanium ions in the SIS100 the pulsed laser excites only 0.008% of the resonant ions. Consequently the laser force of a single pulsed laser system is very weak. The cooling process of titanium ions from an initial rms momentum spread $\sigma_{\delta} = 10^{-4}$ to $\sigma_{\delta} = 10^{-6}$ would require $T_{cool} \approx 6$ hours, following Eq. 5.7. Hence the cooling process of titanium ions with a pulsed laser system is not included in the following investigation.

The simulation results of the rms momentum spread over time are shown in fig. 7.8. The applied scan speeds of the cw laser resonance for the simulations and the analytic predictions (see Eq. 5.2) are shown in tab. 7.3. For titanium ions the perturbation of the synchrotron motion by the laser force is strong and the applied scan speed in the simulation is adjusted to a much higher value compared to the analytic prediction. In the simulation of carbon ions the scan speed of the analytic prediction is used. The scan speed of the laser resonance can be increased or decreased in both cooling processes with the consequence of an decrease or increase of the ion intensity limit, as described in Sect. 6.1.2. The chosen values lead to a good compromise of a reasonable short cooling time and reasonable high intensity limit.

Despite similar values of the laser force and the laser scan speed for both examples, the required cooling time in the SIS100 is much higher compared to the cooling time in

	$^{12}\text{C}^{3+}$	$^{48}\text{Ti}^{19+}$
d_{scan}^{max} analytic	$2 \cdot 10^{-10}$	$2 \cdot 10^{-11}$
d_{scan}^{max} sim	$2 \cdot 10^{-10}$	$1 \cdot 10^{-10}$
N_p^{max} analytic	$6.7 \cdot 10^6$	$6.8 \cdot 10^7$
N_p^{max} sim	$1.5 \cdot 10^6$	10^7
L_{equ} sim	1.4 m	3.6 m

Table 7.3: Simulation results compared to analytic predictions of the scan speed and the maximum ion intensity per bunch for the two laser cooling examples.

the ESR (see fig. 7.8). The main reason for the difference in cooling time is given by the initial momentum spread that scales linearly with the time for the cooling process with a cw laser system. In addition the revolution time is about five times higher in the SIS100 compared to the ESR whereas the length of the cooling section has similar length. The initial momentum spread and the difference in revolution frequency cause a factor of ≈ 45 in cooling time between the ESR and the SIS100 (see Eq. 5.1).

The cooling process of carbon ions with the pulsed laser system gives a similar cooling time and final rms momentum spread as the cooling process with a cw laser system. Both simulations start with equal bunch properties and ion intensity. For the cooling process of carbon ions both cooling schemes are competitive while for titanium ions, the provided laser power of the pulsed laser system is not sufficient.

The required cooling time of carbon ions in the ESR is much shorter in simulation than in experiments. In this simulation the scan speed is optimized for the shortest possible cooling time, while for previous experiments at the ESR the laser scan speed was set to a fixed value. The focus of the experiments was set to the demonstration of laser cooling and the investigation of ultra cold ion beams.

The intensity limits of the simulations are compared to the analytically calculated limits in tab. 7.3. The analytic predictions of IBS heating are calculated for $d_{scan} \rightarrow 0$ (see Eq. 6.9). Due to the strong perturbation of the synchrotron motion by the cw laser force and the finite scan speed, the formula does not provide reliable results. For both ion types a further increase of the ion density leads to a failure of the cooling process. The heating effect of IBS overcomes the cooling force of the cw laser system for higher ion densities. Although the limiting process is IBS, the local rf compensation occurs in the cooling process of carbon ions and the microwave instability occurs in the cooling process of titanium ions. Both instabilities lead to a small fractional loss of ions but do not prevent a successful cooling process for the majority of the ions.

7.3 Effects on Transverse Dynamics

This study concentrates on longitudinal dynamics of the ion beam during the laser cooling process and assumes the transverse phase space to be unchanged. In order to justify

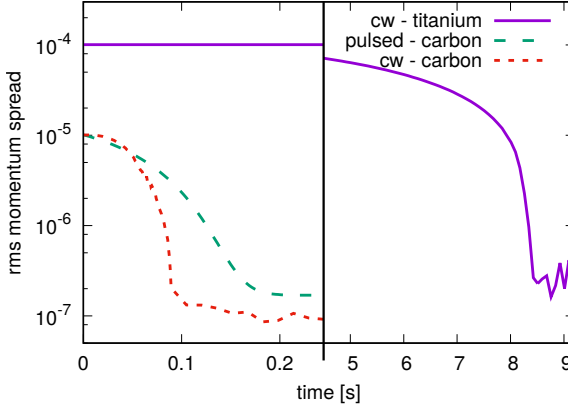


Figure 7.8: Rms momentum spread over time for the cooling process of carbon ions in the ESR and titanium ions in the SIS100. The cooling schemes of a cw and a pulsed laser system are compared for carbon ions. The required cooling time in the SIS100 is much longer compared to the cooling time in the ESR.

this assumption, the strength of the main processes for laser cooling affecting the transverse phase space are estimated. The intensity limits in the ESR and the SIS100 without laser cooling are orders of magnitudes above the intensity limitations of the cooling process that are presented in the previous section. Thus, this investigation focuses on laser cooling specific processes and does not investigate general intensity limits of an ion beam in the accelerator. On the other hand the feasibility of a reduction of the transverse emittance by laser cooling at relativistic beam energies is discussed.

7.3.1 Transverse Laser Heating

Beside the desired momentum transfer in longitudinal direction the spontaneous emission of a photon causes a transverse momentum change of the ions (see Eq. 3.8). The random transverse momentum changes result in a transverse diffusion which leads to a heating of the ion ensemble. The mean absolute value of the momentum change in transverse direction for a spontaneous emission (see Eq. 3.8) is given by

$$\langle |\Delta p_x^{LF}| \rangle = \langle |\Delta p_y^{LF}| \rangle = \frac{\pi \hbar}{\lambda^{LF}} \cdot \gamma \cdot (1 + \beta). \quad (7.3)$$

The transverse momentum transfer in relative coordinates result in

$$\langle |\Delta x'| \rangle = \frac{\langle |\Delta p_x^{LF}| \rangle}{p_0} = \frac{\langle \Delta \delta^{LF} \rangle}{2\gamma}. \quad (7.4)$$

The transverse diffusion D_x^{laser} caused by the ion-photon interaction is calculated by Langevin's equation (see Ref. [67]) which is described in more detail for the longitudinal component in Sect. 4.1, and yields

$$D_x^{laser} = \frac{\langle |\Delta x'| \rangle^2 \cdot n_{scat}(\delta)}{2T_{rev}}. \quad (7.5)$$

Assuming a Gaussian shaped transverse momentum distribution the diffusion causes a growth of the transverse emittance $\epsilon_{x,y}$ that is given by

$$\tau_{x,y}^{-1} = \frac{1}{\epsilon_{x,y}} \frac{d\epsilon_{x,y}}{dt} = \frac{\langle \beta_{x,y} \rangle \beta}{\epsilon_{x,y} \gamma} \cdot \frac{n_{scat}(\delta) \langle \Delta \delta^{LF} \rangle^2}{8T_{rev}}. \quad (7.6)$$

Note, that the value $n_{scat}(\delta)$ depends on the longitudinal momentum of the ions. The laser heating is only experienced by ions that are in resonance with the laser light.

The growth rates of transverse emittance are estimated for carbon ions in the ESR and titanium ions in the SIS100 which are described in Sect. 7.2. Assuming all ions are permanently in resonance with the laser light, the growth rates are $\tau_{x,y}^{-1} = 2.9 \cdot 10^{-9} \frac{1}{sec}$ for titanium ions and $\tau_{x,y}^{-1} = 8.3 \cdot 10^{-8} \frac{1}{sec}$ for carbon ions. Both values are very small compared to typical heating rates in accelerators. The required time for a noticeable growth of the transverse emittance by laser heating exceeds typical laser cooling times. Therefore the transverse laser heating is neglected in the study of laser cooling.

7.3.2 Sympathetic Cooling

Laser cooling directly reduces the longitudinal emittance of the ion beam, but does not affect the transverse phase space. The transverse and longitudinal motions have to be coupled in order to reduce the emittance in all dimensions. The simplest coupling mechanism is the coupling by IBS which is always present. As described in Sect. 2.3 the temperature difference in the longitudinal and transverse degree of freedom leads to a heat transfer from the transverse to the longitudinal phase space. The transverse cooling by IBS is called sympathetic cooling and was experimentally demonstrated e.g.

in Ref. [68]. The cooling rates are calculated by applying the simplified beam parameter functions (see Eq. 2.32) to the rate equations (see Eq. 2.31)

$$\tau_{x,y}^{-1} = -\frac{q^4 L_c}{64\pi^{3/2} m^2 \epsilon_0^2 \beta^3 \gamma^5 c_0^3 \sigma_{x',y'}^2 \epsilon_{x,y}^{3/2} \sqrt{\langle \beta_{x,y} \rangle}} \cdot n = -\tau_\delta^{-1} \cdot \frac{\sigma_\delta^2 \langle \beta_{x,y} \rangle}{\gamma^2 \epsilon_{x,y}}. \quad (7.7)$$

The horizontal and vertical components are assumed to have equal beam parameters and the horizontal dispersion is assumed to be negligible small ($d^2 \ll \frac{1}{2} a^2$). If horizontal dispersion is taken into account, heat is transferred back from the longitudinal to the transverse motion and the strength of sympathetic cooling shrinks (see Eq. 2.31).

The sympathetic cooling rate of the transverse coordinate scales linearly with the ion density. The maximum transverse cooling rate is limited by the highest particle density that is successfully laser cooled in longitudinal direction.

The highest cooling rate is reached after the scan of the laser resonance. The cw laser force is close to the center of the bucket and interacts with all ions simultaneously. The cooling rate is calculated equivalent to the cooling rate of a pulsed laser system (see Eq. 5.5), but with the mean momentum change caused by the cw laser system

$$\hat{\tau}_{cool}^{-1} = -\frac{1}{T_{rev}} \Delta \delta_0 \cdot n_{scat}(0) \cdot \frac{1}{\Delta_{fwhm}}. \quad (7.8)$$

Assuming a final bunch configuration where the longitudinal IBS heating fully compensates the longitudinal cooling, the maximum transverse cooling rate is calculated by

$$\hat{\tau}_{x,y}^{-1} = \hat{\tau}_{cool}^{-1} \cdot \frac{\sigma_\delta^2 \langle \beta_{x,y} \rangle}{\gamma^2 \epsilon_{x,y}} \quad (7.9)$$

$$= -\frac{1}{T_{rev}} \Delta \delta_0 \cdot n_{scat}(0) \cdot \frac{1}{\Delta_{fwhm}} \cdot \frac{\sigma_\delta^2 \langle \beta_{x,y} \rangle}{\gamma^2 \epsilon_{x,y}}, \quad (7.10)$$

where the rms momentum spread has to be $\sigma_\delta \approx \Delta_{fwhm}$ in order to keep all ions in resonance with the laser force. The transverse cooling rates of sympathetic cooling for the two examples described in Sect. 7.2 result in $\hat{\tau}_{x,y}^{-1} = 10^{-8} \frac{1}{sec}$ for titanium ions in the SIS100 and $\hat{\tau}_{x,y}^{-1} = 10^{-5} \frac{1}{sec}$ for carbon ions in the ESR. Due to the factor $\frac{1}{\gamma^2}$ sympathetic cooling becomes very inefficient at relativistic ion beams. The transverse cooling rates are too small for a practical three dimensional cooling by IBS. In addition, IBS rates are assumed to decrease at ultra low temperatures due to a phase transition to the strongly coupled regime (see Ref. [69]). Consequently the estimated IBS cooling rates might be much smaller in reality. In conclusion the change of the transverse emittance by IBS can be neglected during the laser cooling process for relativistic ion beams.

7.3.3 Induced Longitudinal-Transverse Coupling

The coupling of the longitudinal and transverse motion by IBS is not strong enough to efficiently cool all three dimensions of a relativistic ion beam. An induced coupling is necessary to transfer emittance from the transverse to the longitudinal phase space. Different coupling mechanisms exist and were studied during laser cooling experiments of non-relativistic ion beams.

One possible coupling method of the horizontal and longitudinal motion during laser cooling is to introduce a finite dispersion in the interaction section of the ions with the laser beam. The momentum change of the resonant interaction of the ion with a laser photon leads to a shift of the closed orbit by $\Delta x = D(s) \cdot \Delta\delta^{LF}$, where $D(s)$ is the dispersion function in the interaction section and x the horizontal position of the ion. A horizontal gradient of the laser force leads to a stronger change of the closed orbit for particles with a high transverse displacement and consequently a reduction of the horizontal emittance. A horizontal gradient of the laser force can be realized by a displacement of the laser beam with respect to the ion beam. This technique is called "dispersive cooling" and was demonstrated at the TSR in Heidelberg (see Ref. [22, 70]). Another technique is called "tapered cooling" and applies a horizontal gradient of the laser frequency to the ion beam (see Ref. [71]).

An induced coupling of the longitudinal and transverse phase space can also be realized independent of the ion laser interaction. A finite dispersion in the section of the accelerating cavities leads to a closed orbit change during acceleration or deceleration of the ions. If the sum of the longitudinal and the horizontal tune result in an integer, the synchro-betatron resonance couples the two coordinates and transfers emittance. This technique was successfully tested in laser cooling experiments as described in Ref. [72, 73, 74].

Both methods have proven the three dimensional reduction of the emittance during laser cooling experiments. However, the techniques were only applied to non-relativistic beams, where the cw laser force interacts with all ions simultaneously and no scan of the cw laser force is necessary. Furthermore the longitudinal motion slows down at relativistic beam energies and makes it difficult to create a synchro-betatron coupling. In order to evaluate the applicability and efficiency of three dimensional cooling at relativistic beam energies, detailed numerical simulations are necessary.

8 Conclusion and Outlook

Doppler laser cooling is a promising technique for the reduction of the longitudinal momentum spread of relativistic ion beams in circular accelerators. Previous studies of laser cooling focused on non-relativistic ion beams in low energy storage rings. In this work the efficiency of the laser cooling process and the underlying particle dynamics for relativistic beam energies are investigated. This study concentrates on analytic estimations and numerical simulations for the first laser cooling experiments of relativistic ion beams at the SIS100.

The resonant interaction of ions with laser photons is investigated. The probability of a spontaneous emission is calculated for a continuous wave and pulsed laser excitation with the optical Bloch equations. The excitation with a continuous wave laser results in a strong laser force with a spectral width which is typically three to four orders of magnitude below the initial momentum spread of a relativistic ion beam. Short laser pulses increase the spectral width of the laser force but reduce the amplitude of the force. For the investigation of the cooling process, models of the continuous wave and the pulsed laser excitation are implemented in a particle tracking code. The tracking code includes particle-in-cell routines for space charge and intra beam scattering.

The particle dynamics in the longitudinal phase space are analyzed. For the cooling process with a continuous wave laser system, the laser resonance is scanned from the ion with the highest oscillation amplitude to the center of the rf bucket. The laser force interacts with the ions at the bunch boundary and gathers them into a dense ring in longitudinal phase space. The radius of the dense ring shrinks in the same way as the laser resonance is scanned to the bucket center. A proper choice of the scan speed is crucial in order to successfully cool all ions within a short period of time. An analytic estimation of the optimal scan speed is given. For the cooling process with a pulsed laser excitation, the laser interacts with all ions simultaneously. The rms momentum spread decreases exponentially and the bunch profile stays nearly Gaussian during the whole cooling process. The particle dynamics are well described by rms rate equations. The cooling times for both cooling schemes are given. If sufficient laser intensities are available, both cooling schemes give comparable results.

Space charge and intra beam scattering counteract the laser force. During the cooling process, the ion density increases until space charge fully compensates the applied rf potential. The complete compensation defines the shortest bunch length that can be reached during laser cooling. However, the lowest rms momentum spread is not affected by the compensation of the rf potential but by the heating of intra beam scattering. For the cooling process with a pulsed laser, the diffusive heating of intra beam scattering generate a correlation of the final rms momentum spread and the ion intensity, which is calculated by rms rate equations. For the cooling process with a continuous wave laser,

intra beam scattering increases the width of the dense ring in phase space, which is formed by the narrow band laser force. The diffusive heating leads to an increase of the required cooling time until the heating overcomes the laser force and the cooling process fails. In addition, the dense ring in phase space becomes unstable in the presence of space charge. Depending on the bucket configuration and ion intensity, space charge triggers the microwave instability or the local rf compensation. Both effects lead to chaotic motion of the ions and a broadening of the dense ring in phase space. The underlying particle dynamics and ion intensity threshold for both effects are analyzed.

The scaling of the laser cooling process for different beam energies is analyzed. The laser force that is normalized to the momentum of the ions is approximately constant for the cooling process of lithium-like ions at different beam energies. However, the required laser intensity drastically increases for higher beam energies, which becomes a major challenge for laser cooling at relativistic beam energies. The laser cooling processes of non-relativistic carbon ions in the ESR and relativistic titanium ions in the SIS100 are compared. Although the laser force is very similar for both examples, the cooling time of titanium ions significantly exceeds the cooling time of carbon ions. The higher initial momentum spread and the lower revolution frequency are the main reasons for this. The ion intensity limits of both examples are very similar. For carbon ions the cooling process with a pulsed and a continuous wave laser are competitive in terms of cooling time and intensity limit. Pulsed laser cooling of titanium ions is not possible, because the required laser intensity exceeds the typical output power of available laser sources.

In the future, the presented theoretical results of laser cooling should be compared to experiments. The influence of different scan speeds of the continuous wave laser force on the success of the cooling process has not been measured yet. Experimental data would give a better insight of the ion-photon interaction and the counteracting intensity effects. In particular, the Schottky spectra of the stable bunch distributions after the microwave instability and the local rf compensation should be calculated from numerical simulations. The Schottky monitor is the most accurate measurement device of the particle dynamics during laser cooling experiments of carbon ions in the ESR. Similarities of simulated and measured Schottky spectra would prove the existence of the space charge instabilities presented in this work.

Further research could focus on the reduction of the transverse emittance by dispersive or tapered cooling. Detailed three-dimensional simulations would evaluate the possibility of three-dimensional laser cooling of relativistic ion beams within a reasonable time.

Finally, the numerical particle-in-cell simulations of laser cooling at relativistic beam energies can be extended by simulations with direct coulomb interactions between the ions. The simulations would lead to a better understanding of the transition to ultra-cold relativistic ion beams and would show if a crystallization of a relativistic ion beam is possible.

Acknowledgements

I would like to thank Prof. Oliver Boine-Frankenheim for offering me a PhD position at TEMF and giving constructive criticism on my work. He successfully guided me to improve scientific skills and supported the participation in conferences. I want to thank Prof. Joachim Enders for being the second referee in this thesis.

I thank Dr. Danyal Winters, because he introduced me to the collaboration of laser cooling at GSI and provided information about previous studies, experiments and future plans at FAIR. Many fruitful discussions with him improved this work. Besides he gave me the opportunity to participate in a laser cooling experiment at GSI in order to add practical experiences to the theoretical work.

I want to thank Dr. Michael Bussmann for valuable discussions on my work. He explained me interpretations of previous studies and experiments and gave me valuable hints on my work. Also I thank Prof. Thomas Walther and Daniel Kiefer for helpful feedback and information about the applied laser systems.

I am indebted to the colleagues from IMP in China, particular Prof. Xinwen Ma and Weiqiang Wen, who invited me for experiments twice. The experimental insights in laser cooling improved my understanding in the topic and the experimental challenges.

I thank all TEMF colleagues and former TEMF colleagues for a nice atmosphere. Especially I want to thank my office colleagues Dr. Fedor Petrov and Dimitry Bazyl for a nice environment and work related or unrelated discussions. Also I thank Oliver S. Haas for creative suggestions on numerics and help with computer problems. Special thanks goes to Dr. Uwe Niedermayer, Dr. William D. Stem and Sebastian Golisch for proofreading this thesis and improving it with helpful comments.



List of Figures

1.1	Site map of the planned FAIR facility	2
2.1	Sketch of the co-moving coordinate system	8
2.2	Sketch of the longitudinal dynamics in phase space	10
3.1	Single resonant ion-photon interaction	17
3.2	Illustration of the Doppler laser cooling process in a particle trap	18
3.3	Transition wavelength and lifetime for lithium-like ions	20
3.4	Required magnetic rigidity for the resonant condition	21
3.5	Sketch of the interaction section of the laser beam and the circulating ions	22
3.6	Excitation probability for the excitation with a cw laser	25
3.7	Saturation intensity for cw laser excitation	26
3.8	Excitation probability over time of the pulsed laser system	27
3.9	Required average intensity of pulsed laser system	29
4.1	Example of excitation probability of a single ion	35
4.2	Histogram of the probability of different numbers of spontaneous emissions during the interaction section	37
4.3	Final rms momentum spread for different scan speeds of the laser force	38
5.1	Sketch of the ion trajectory during the cooling process	41
5.2	Final rms momentum spread for different scan speeds of the laser force	42
5.3	Evolution of the phase space distribution for a successful cooling process	43
5.4	Evolution of the momentum distribution over time	44
5.5	Snapshot of the phase space distribution for an unsuccessful cooling process	45
5.6	Maximum scan speed for different strength of the perturbation of the synchrotron motion	46
5.7	Snapshot of the phase space density during an alternative cooling scheme	47
5.8	Illustration of the pulsed laser force	48
5.9	Cooling process with a single pulsed laser system	49
5.10	Required cooling time for the cooling process with a pulsed laser system	51
5.11	Equilibrium rms momentum spread for the cooling process with a pulsed laser system	52
5.12	Illustration of the laser cooling force for combined pulsed laser systems	53
5.13	Rms momentum spread over time for the combination of two laser systems	54
5.14	Sketch of the phase space area in a barrier bucket	55
5.15	Momentum distribution during the cooling process in a barrier bucket	56

5.16 Rms momentum spread after the cw laser scan in the barrier bucket . . .	57
6.1 Equilibrium rms momentum spread for IBS heating and pulsed laser cooling	60
6.2 Final rms momentum spread after cw laser cooling for different strength of IBS heating	61
6.3 Equilibrium state of space charge and rf potential	63
6.4 Relative reduction of the bunch length and rms momentum spread during pulsed laser cooling	64
6.5 Equilibrium rms momentum spread for IBS heating, space charge and pulsed laser cooling	65
6.6 Beam blow up at the final state of the cooling process	66
6.7 Space charge and rf forces during the local rf compensation	68
6.8 Evolution of the phase space density during the local rf compensation . .	69
6.9 Phase space density during the microwave instability	70
6.10 Evolution of the phase space density of isolated ring under influence of space charge	71
6.11 Comparison of the negative mass instability and the unstable ring	72
6.12 Ion line density and space charge kick for the isolated ring in phase space	73
6.13 Space charge induced synchrotron tune shift	74
6.14 Growth of the microwave instability	77
7.1 Mean momentum change of a resonant interaction in the LF	79
7.2 Relative laser force of a cw laser system	80
7.3 Width of the cw laser	81
7.4 IBS strength	82
7.5 Space charge strength	83
7.6 Influence of the space charge cut off frequency on the space charge field of the peaks	84
7.7 Influence of the space charge cut off frequency on synchrotron tune shift	85
7.8 Rms momentum spread of carbon and titanium ions during cooling process	89



List of Tables

- 7.1 Properties of the ESR and the SIS100 86
- 7.2 Properties and strength of the cw and pulsed laser system for the two laser cooling examples. 87
- 7.3 Simulation results compared to analytic predictions 88



List of Symbols

Units are given in SI (Système international d'unités). An arrow denotes a vectorized quantity, where applicable the same symbol without the arrow is used for the absolute value of the quantity. A mean value is indicated as $\langle \cdot \rangle$. The mean value calculated at the fixed position is denoted $\langle \cdot \rangle_{fp}$. The maximum value of a quantity is marked by a $\hat{\cdot}$. The indices $_x$ and $_y$ denote the horizontal and the vertical component of the quantity, respectively.

Term	Unit	Description
k_B	J/K	Boltzmann constant
T	K	Temperature
m	kg	Rest mass
v	m/s	Particle velocity
τ^{-1}	1/s	Cooling or heating rate
n_e	$1/m^3$	Electron density
β	1	Relativistic velocity ($\beta = v/c_0$)
γ	1	Relativistic factor
p_0	$kg \cdot m/s$	Particle momentum
Δp	$kg \cdot m/s$	Particle momentum deviation
δ	1	Relative particle momentum deviation ($\delta = \Delta p/p_0$)
δ_{rms}	1	Rms value of relative particle momentum deviation
q	C	Charge of particle
\vec{F}	N	Force
\vec{E}	V/m	Electric field
\vec{B}	T	Magnetic flux density
t	s	Time
Z	1	Atomic number
ρ	m	Bending radius in dipole magnets
x, y, z	m	Coordinates in the co-moving coordinate system
$\sigma_{x'}, \sigma_{y'}, \sigma_{\delta}$	1	rms values of horizontal, vertical and longitudinal beam divergence
$\beta(s)$	m	Beta function of accelerator lattice
ϵ	m	Particle emittance
L_{acc}	m	Length of circular accelerator
$D(s)$	m	Particle dispersion at position s

Term	Unit	Description
γ_t	1	Relativistic factor at transition energy
η	1	Slip factor ($\eta = 1/\gamma_t^2 - 1/\gamma$)
c_0	m/s	Speed of light
U_{rf}	V	rf voltage
U_0	V	Amplitude of rf voltage
h	1	Harmonic number ($h = \omega_{rf}/\omega_{rev}$)
T_{rev}	s	Time for revolution in accelerator
ω_{rev}	1/s	Angular revolution frequency ($\omega_{rev} = 2\pi/T_{rev}$)
Q_s	1	Synchrotron tune ($Q_s = \omega_s/\omega_{rev}$)
\mathcal{H}	J	Hamiltonian
$\hat{z}, \hat{\delta}$	m, 1	Bunch boundary in z and δ
$\lambda(z)$	1/m	Longitudinal line density
N_p	1	Number of particles
M_p	1	Number of macro particles
E_s	V/m	Space charge electric field
g_{sc}	1	Space charge geometrical factor
ϵ_0	F/m	The vacuum permittivity
Z_{\parallel}	Ω	Longitudinal impedance
f_c	1/s	Space charge cut off frequency
L_c	1	coulomb logarithm
λ	m	Wavelength
τ_{se}	s	Lifetime of the excited state
U	1	Random number
k_{se}	1/s	Spontaneous emission rate
ρ_{ee}	1	Probability of the excited state
n_{scat}	1	Number of scattering events
Ω_{rabi}	1/s	Rabi frequency
\hbar	Js	Planck constant
$L_{interact}$	m	Ion photon interaction length
I	W/m^2	Laser intensity
S	1	Saturation parameter
Δ_{fwhm}	1	FWHM of excitation probability in units of relative momentum
$\sigma_{\delta Laser}$	1	Standard deviation of pulsed laser excitation in units of relative momentum
σ_t^{LF}	s	Standard deviation of laser pulse in time in LF
ρ_{gg}	1	Porbability of ground state
f_{rep}	1/s	Repetition rate of pulsed laser system

Term	Unit	Description
ρ_{scat}	1	Probability of a spontaneous emission per turn for pulsed laser excitation
Λ	1	Plasma parameter
$f(\vec{r}, \vec{p})$	1/m	One dimensional distribution function
D_{IBS}	1/s	IBS diffusion coefficient
ξ	1/s	Constant describing the relation between momentum change and shift of laser frequency
δ_{LPoS}	1	Position of laser resonance in units of relative momentum
T_{cool}	s	Time of cooling process
d_{scan}	1	Scan speed of laser resonance in phase space in units of relative momentum per turn
$\Delta\delta_{turn}^{LF}(\delta)$	1	Momentum change of ion per turn originating in the ion cw laser interaction
D_L	1/s	Laser induced diffusion
L_{BB}	m	Length of barrier bucket
L_{equ}	m	Equilibrium bunch length of rf and space charge voltage
ϱ	1	Radial coordinate new defined coordinate system.
ζ	m	Angular coordinate new defined coordinate system.
χ	1	Derivation of synchrotron tune with respect to ϱ
δ_{ring}, z_{ring}	1,m	Size of ellipse in phase space in z and δ
k	1/m	Wavenumber
τ_{mw}^{-1}	1/s	Growth rate of microwave instability



List of Acronyms

- ASTRID Aarhus storage ring in Denmark.
- CERN Organisation européenne pour la recherche nucléaire.
- cw continuous wave.
- ESR Experimentierspeicherring (experimental storage ring).
- FAIR Facility for Antiproton and Ion Research in Europe GmbH.
- FFT fast Fourier transformation.
- FWHM Full Width Half Maximum.
- GSI GSI Helmholtzzentrum für Schwerionenforschung GmbH.
- IBS intra beam scattering.
- LF laboratory frame.
- PF particle rest frame.
- PIC Particle In Cell.
- rf radio frequency.
- rms root mean square.
- UNILAC Universal Linear Accelerator.
- SC Space charge.
- SIS100 Schwerionensynchrotron 100 (heavy ion synchrotron).
- SIS18 Schwerionensynchrotron 18 (heavy ion synchrotron).
- TSR test storage ring.



Bibliography

- [1] A. W. Chao and W. Chou, “Editorial preface,” *Reviews of Accelerator Science and Technology*, vol. 04, no. 01, pp. v–vi, 2011. 1
- [2] J. D. Cockcroft and E. T. S. Walton, “Experiments with high velocity positive ions,” *Proceedings of the Royal Society A: Mathematical, Physical and Engineering Sciences*, vol. 129, no. 811, pp. 477–489, 1930. 1
- [3] R. Wideröe, “Über ein neues Prinzip zur Herstellung hoher Spannungen,” *Archiv für Elektrotechnik*, vol. 21, no. 4, pp. 387–406, 1928. 1
- [4] G. Brianti and J. D. Lawson, “CAS - CERN Accelerator School: 50 years of synchrotrons,” 1997. 1
- [5] E. D. Courant and H. S. Snyder, “Theory of the alternating gradient synchrotron,” *Annals Phys.*, vol. 3, pp. 1–48, 1958. [Annals Phys.281,360(2000)]. 1
- [6] E. M. McMillan, “The synchrotron—a proposed high energy particle accelerator,” *Phys. Rev.*, vol. 68, pp. 143–144, 1945. 1
- [7] “www.fair-center.eu.” 2
- [8] M. Reiser, *Theory and Design of Charged Particle Beams*. Wiley-VCH, 2008. 3, 7, 13
- [9] G. I. Budker, “An effective method of damping particle oscillations in proton and antiproton storage rings,” *Soviet Atomic Energy*, vol. 22, no. 5, pp. 438–440, 1967. 3
- [10] G. I. Budker and et al., “Experimental study of electron cooling,” *Particle Accelerators*, vol. 7, pp. 197–211, 1978. 3
- [11] E. Rutherford, “The scattering of α and β particles by matter and the structure of the atom,” *Philosophical Magazine and Journal of Science*, vol. 21, no. 125, pp. 669–688, 1911. 4
- [12] M. Steck and et al., “Cooled heavy ion beams at the ESR,” *Nuclear Physics A*, vol. 626, no. 1, pp. 495 – 498, 1997. 4

-
- [13] M. Steck, P. Beller, K. Beckert, B. Franzke, and F. Nolden, “Electron cooling experiments at the ESR,” *Nuclear Instruments and Methods in Physics Research Section A*, vol. 532, no. 1, pp. 357 – 365, 2004. International Workshop on Beam Cooling and Related Topics. 4
- [14] H. Poth, “Electron cooling: theory, experiment, application,” *Physics reports*, vol. 196, no. 3-4, pp. 135–297, 1990. 4
- [15] T. Bergmark and et al., “Status of the HESR electron cooler design work,” *TUPLS067, Proceedings of EPAC*, 2006. 4
- [16] S. Van der Meer, “Stochastic damping of betatron oscillations in the ISR,” Tech. Rep. CERN-ISR-PO-72-31. ISR-PO-72-31, CERN, Geneva, 1972. 4
- [17] G. Carron and et al., “Experiments on stochastic cooling in ICE (initial cooling experiment),” *IEEE Transactions on Nuclear Science*, vol. 26, no. 3, pp. 3455–3461, 1979. 4
- [18] J. Marriner and D. McGinnis, “An introduction to stochastic cooling,” *AIP Conference Proceedings*, vol. 249, no. 1, pp. 693–761, 1992. 4
- [19] F. Nolden and et al., “Stochastic cooling at the ESR,” *Nuclear Instruments and Methods in Physics Research Section A*, vol. 441, no. 1, pp. 219 – 222, 2000. 4
- [20] W. D. Phillips, “Nobel lecture: Laser cooling and trapping of neutral atoms,” *Rev. Mod. Phys.*, vol. 70, pp. 721–741, 1998. 5, 17
- [21] S. Schröder and et al., “First laser cooling of relativistic ions in a storage ring,” *Phys. Rev. Lett.*, vol. 64, pp. 2901–2904, 1990. 5, 17
- [22] I. Lauer and et al., “Transverse laser cooling of a fast stored ion beam through dispersive coupling,” *Phys. Rev. Lett.*, vol. 81, pp. 2052–2055, 1998. 5, 92
- [23] J. S. Hangst, M. Kristensen, J. S. Nielsen, O. Poulsen, J. P. Schiffer, and P. Shi, “Laser cooling of a stored ion beam to 1 mK,” *Phys. Rev. Lett.*, vol. 67, pp. 1238–1241, 1991. 5
- [24] U. Schramm and et al., “Laser cooling of relativistic heavy ion beams,” in *Proceedings of the 2005 Particle Accelerator Conference*, pp. 401–403, 2005. 5
- [25] D. Winters and et al., “Laser cooling of relativistic heavy-ion beams for FAIR,” *Physica Scripta*, vol. 2015, no. T166, p. 014048, 2015. 5, 21, 22

-
- [26] G. Birkel, S. Kassner, and H. Walther, "Multiple-shell structures of laser-cooled ^{24}Mg ions in a quadrupole storage ring," *Nature*, vol. 357, no. 6376, pp. 310–313, 1992. 5
- [27] U. Schramm, M. Bussmann, and D. Habs, "From laser cooling of non-relativistic to relativistic ion beams," *Nuclear Instruments and Methods in Physics Research Section A*, vol. 532, no. 1, pp. 348 – 356, 2004. 5, 25
- [28] S. Y. Lee, *Accelerator Physics (Third Edition)*. World Scientific Publishing Company, 2012. 8, 9, 14, 71, 74, 76
- [29] K. Wille, *The physics of particle accelerators: an introduction*. Clarendon Press, 2000. 8
- [30] A. Hofmann and F. Pedersen, "Bunches with local elliptic energy distributions," *IEEE Transactions on Nuclear Science*, vol. 26, no. 3, pp. 3526–3528, 1979. 12
- [31] O. Boine-Frankenheim and T. Shukla, "Space charge effects in bunches for different rf wave forms," *Phys. Rev. ST Accel. Beams*, vol. 8, p. 034201, 2005. 12
- [32] J. L. Laclare, "Coasting beam longitudinal coherent instabilities," *Proc. CAS, General Accelerator Physics, Vol. 1. CERN 94-01*, 1994. 14
- [33] J. J. Bisognano, "Solitary waves in particle beams," *Proceedings of the Fifth European Particle Accelerator Conference*, p. 328, 1996. 14
- [34] O. Boine-Frankenheim and I. Hofmann, "Vlasov simulation of the microwave instability in space charge dominated coasting ion beams," *Phys. Rev. ST Accel. Beams*, vol. 3, p. 104202, 2000. 14
- [35] A. M. Al-khateeb, O. Boine-Frankenheim, I. Hofmann, and G. Rumolo, "Analytical calculation of the longitudinal space charge and resistive wall impedances in a smooth cylindrical pipe," *Phys. Rev. E*, vol. 63, p. 026503, 2001. 14
- [36] J. Wei, "Evolution of hadron beams under intrabeam scattering," in *Particle Accelerator Conference, 1993., Proceedings of the 1993*, pp. 3651–3653, IEEE, 1993. 15
- [37] H. J. Metcalf and P. Van der Straten, *Laser Cooling and Trapping*. Graduate texts in contemporary physics, Springer, 1999. 18, 23, 24, 25, 36, 50

-
- [38] W. R. Johnson, Z. W. Liu, and J. Sapirstein, “Transition rates for lithium-like ions, sodium-like ions, and neutral alkali-metal atoms,” *Atomic Data and Nuclear Data Tables*, vol. 64, no. 2, pp. 279–300, 1996. 20
- [39] U. Schramm and D. Habs, “Crystalline ion beams,” *Progress in particle and Nuclear Physics*, vol. 53, no. 2, pp. 583–677, 2004. 20, 21
- [40] M. Bussmann, *Laser Cooling of Ion Beams at Relativistic Energies*. ICFA Beam Dynamics Newsletter No. 65, 2014. 27
- [41] M. Siebold and et al., “High energy yb:yag active mirror laser system for transform limited pulses bridging the picosecond gap,” *Laser & Photonics Reviews*, vol. 10, no. 4, pp. 673–680, 2016. 27
- [42] J.-C. Diels and W. Rudolph, *Ultrashort Laser Pulse Phenomena, Second Edition (Optics and Photonics Series)*. Academic Press, 2006. 27
- [43] Y. Yuri and H. Okamoto, “Generating ultralow-emittance ion beams in a storage ring,” *Physical review letters*, vol. 93, no. 20, p. 204801, 2004. 31
- [44] H. Babovsky, *Die Boltzmann-Gleichung: Modellbildung - Numerik - Anwendungen (Leitfäden der angewandten Mathematik und Mechanik)*. Vieweg+Teubner Verlag, 1998. 32
- [45] R. W. Hockney and J. W. Eastwood, *Computer simulation using particles*. crc Press, 1988. 32
- [46] C. K. Birdsall and A. B. Langdon, “Plasma physics via computer simulation, Inst. of Phys,” *Publishing, Bristol/Philadelphia*, 1991. 32
- [47] R. Courant, K. Friedrichs, and H. Lewy, “Über die partiellen Differenzgleichungen der mathematischen Physik,” *Mathematische annalen*, vol. 100, no. 1, pp. 32–74, 1928. 32
- [48] G. Van Rossum and et al, “Python programming language.,” in *USENIX Annual Technical Conference*, vol. 41, p. 36, 2007. 33
- [49] S. Behnel, R. Bradshaw, D. S. Seljebotn, G. Ewing, and et al., “Cython: C-extensions for Python,” 2008. 33
- [50] K. Huang, *Introduction to Statistical Physics*. CRC Press, 2001. 34
- [51] I. N. Meshkov, A. O. Sidorin, A. V. Smirnov, and G. V. Trubnikov, “Betacool physics guide,” tech. rep., Joint Institute for Nuclear Research Joliot Curie, 2008. 34

-
- [52] “BETACOOOL, <http://betacool.jinr.ru/>.” 34
- [53] I. N. Meshkov, A. O. Sidorin, A. V. Smirnov, G. V. Trubnikov, and V. Malakhov, “Software development for beam cooling simulation including general collider physics,” tech. rep., Joint Institute for Nuclear Research, Dubna, Russia, 2007. 34
- [54] K. Mølmer, Y. Castin, and J. Dalibard, “Monte Carlo wave-function method in quantum optics,” *JOSA B*, vol. 10, no. 3, pp. 524–538, 1993. 36
- [55] J. S. Hangst, J. S. Nielsen, O. Poulsen, P. Shi, and J. P. Schiffer, “Laser cooling of a bunched beam in a synchrotron storage ring,” *Phys. Rev. Lett.*, vol. 74, pp. 4432–4435, 1995. 42, 64
- [56] K. P. Ningel, H. Klingbeil, U. Laier, B. Zipfel, C. Thielmann, and P. Hülsmann, “Dual harmonic operation at SIS18,” *Proceedings IPAC*, vol. 10, pp. 23–28, 2010. 53
- [57] J. E. Griffin, C. Ankenbrandt, J. A. MacLachlan, and A. Moretti, “Isolated bucket rf systems in the fermilab antiproton facility,” *IEEE Transactions on Nuclear Science*, vol. 30, no. 4, pp. 3502–3504, 1983. 53
- [58] U. Eisenbarth and et al., “Laser cooling of fast stored ions in barrier buckets,” *Nuclear Instruments and Methods in Physics Research Section A*, vol. 441, no. 1, pp. 209–218, 2000. 53
- [59] U. Eisenbarth and et al., “Anomalous behaviour of laser cooled fast ion beams,” *Hyperfine Interactions*, vol. 127, no. 1, pp. 223–235, 2000. 59
- [60] Y. Yuri, “Molecular dynamics simulation of the three-dimensional ordered state in laser-cooled heavy-ion beams,” in *Proceedings of the 12th Asia Pacific Physics Conference (APPC12)*, Journal of the Physical Society of Japan, 2014. 59
- [61] U. Schramm, T. Schätz, M. Bussmann, and D. Habs, “Cooling and heating of crystalline ion beams,” *Journal of Physics B: Atomic, Molecular and Optical Physics*, vol. 36, no. 3, p. 561, 2003. 59
- [62] E. Keil and W. Schnell, “Concerning longitudinal stability in the ISR,” Tech. Rep. CERN-ISR-TH-RF-69-48, CERN, Geneva, 1969. 77
- [63] M. Bussmann and et al., “The dynamics of bunched laser-cooled ion beams at relativistic energies,” *Journal of Physics: Conference Series*, vol. 88, no. 1, p. 012043, 2007. 86

-
- [64] W. Wen and et al., “Laser cooling of stored relativistic ion beams with large momentum spreads using a laser system with a wide scanning range,” *Journal of Physics: Conference Series*, vol. 488, no. 12, p. 122005, 2014. 86
- [65] T. Beck, *Lasersystem zur Kühlung relativistischer C^{3+} -Ionenstrahlen in Speicherringen*. PhD thesis, Technische Universität Darmstadt, 2015. 86
- [66] T. Beck, B. Rein, F. Sörensen, and T. Walther, “Solid-state-based laser system as a replacement for Ar^+ lasers,” *Opt. Lett.*, vol. 41, no. 18, pp. 4186–4189, 2016. 86
- [67] H. Risken, *The Fokker-Planck Equation*. Springer Berlin Heidelberg, 1984. 90
- [68] H.-J. Miesner, R. Grimm, M. Grieser, D. Habs, D. Schwalm, B. Wanner, and A. Wolf, “Efficient, indirect transverse laser cooling of a fast stored ion beam,” *Physical review letters*, vol. 77, no. 4, p. 623, 1996. 91
- [69] Q. Spreiter, M. Seurer, and C. Toepffer, “Relaxation in a strongly coupled particle beam,” *Nuclear Instruments and Methods in Physics Research Section A*, vol. 364, no. 2, pp. 239 – 242, 1995. 91
- [70] U. Eisenbarth, *Laser cooling of fast stored ion beams to extreme phase-space densities*. PhD thesis, Heidelberg University, 2001. 92
- [71] H. Okamoto and J. Wei, “Theory of tapered cooling,” *Phys. Rev. E*, vol. 58, pp. 3817–3825, 1998. 92
- [72] A. Noda and et al., “Ultralow emittance beam production based on doppler laser cooling and coupling resonance,” *Proceeding of IPAC14*, 2014. 92
- [73] H. Souda and et al., “Transverse laser cooling by synchro-betatron coupling,” *Proceeding of IPAC10*, pp. 861–863, 2010. 92
- [74] H. Okamoto, “Transverse laser cooling induced through dispersion at an rf cavity,” *Phys. Rev. E*, vol. 50, pp. 4982–4996, 1994. 92

Curriculum Vitae

Lewin Eidam

Born on 24.03.1989 in Fritzlar, Germany

Education and Work Experience

- 06/2014 to Present **PhD student and research staff at the Institut “Theorie Elektromagnetischer Felder” at Technical University Darmstadt, Germany**
- 10/2011 to 01/2014 **Study of Physical Science at the Technical University Darmstadt**
Field: Nuclear Physics; Degree: Master of Science
- 05/2012 to 02/2014 **Student trainee at GSI Helmholtzzentrum für Schwerionenforschung**
- 06/2011 to 12/2013 **Student Assistant at the Institute of Nuclear Research**
Operator of the electron Accelerator S-DALINAC
- 10/2008 to 10/2011 **Study of Physical Science at the Technical University Darmstadt**
Field: Nuclear Physics; Degree: Bachelor of Science
- 10/2010 to 02/2012 **Student Assistant for Experimental Physics I-III at Technical University Darmstadt**
mentoring exercise courses for students (Prof. D.H.H. Hoffmann)
- 04/2010 to 07/2010 **Student Assistant for Physics for Civil Engineers at Technical University Darmstadt**
mentoring exercise courses for students (Prof. R. Feile)
- 09/1999 to 07/2008 **Gustav-Stresemann-Gynasium Bad Wildungen**
higher education entrance qualification

Computer and Foreign Language Skills

Good knowledge in Linux and Windows
Programming skills in C, Python, Cython, Mathematica, LATEX, CAD modeling
Good knowledge in German (mother tongue)
Good knowledge in English (9 years at school)
Basic knowledge in Latin (5 years at school)

Publications

L. Eidam, O.Boine-Frankenheim, D. Winters. "Cooling rates and intensity limitations for laser-cooled ions at relativistic energies" Nuclear Instruments and Methods in Physics Research Section A, submitted for publication, available on arXiv: <http://arxiv.org/abs/1709.03338>

H. B. Wang,...,L. Eidam, et al. "Measurement of the lifetime and the proportion of $^{12}\text{C}^{3+}$ ions in stored relativistic ion beams as a preparation for laser cooling experiments at the CSRe." Nuclear Instruments and Methods in Physics Research Section B, 2017

L. Eidam, O. Boine-Frankenheim, D. Winters. "Simulation Studies on Intensity Limitations of Laser Cooling at High Energy." Proceeding of International Workshop on Beam Cooling and Related Topics (COOL'15), Newport News, VA, USA, 2015

U. Niedermayer, L. Eidam, and O. Boine-Frankenheim. "Analytic modeling, simulation and interpretation of broadband beam coupling impedance bench measurements." Nuclear Instruments and Methods in Physics Research Section A, p. 129-143, 2015

L. Eidam, O. Boine-Frankenheim, D. Winters. "Simulation of Laser Cooling of Heavy Ion Beams at High Intensities", Proceeding of International Particle Accelerator Conference (IPAC15), MOPWA025, p. 150-152, Richmond, VA, USA, 2015.

Oral presentations

"Laser Cooling of Heavy Ion Beams at High Energies and Intensities", atomphysikalisches Seminar GSI, Darmstadt, May 2017

"Cooling Rates and Intensity Limitations of Laser Cooling at Ultra Relativistic Beam Energies", FWK-Seminar HZDR Dresden, Dresden-Rossendorf, Februar 2017

"Particle-In-Cell Simulations of Intense Laser Cooled Ion Beams", Workshop on the Frontiers of Intense Beam Physics Modeling, Boulder, USA, October 2016

"Laser Cooling of Intense Ultra-Relativistic Ion Beams", DPG Spring meeting, Darmstadt, 15. March 2016

"Laser Cooling of Relativistic Heavy Ion Beams in SIS100", HIC for FAIR PAC meeting, Darmstadt, October 2015

"Simulation der Laserkühlung von intensiven Schwerionenstrahlen", DPG Spring meeting, Wuppertal, March 2015
